TECHNISCHE UNIVERSITÄT MÜNCHEN
Lehrstuhl für Radiochemie
Fakultät für Chemie

A new focal plane detector for the gas-filled separator TASCA

Alexander Gorshkov

Vollständiger Abdruck der von der Fakultät für Chemie
der Technischen Universität München zur Erlangung des akademischen Grades eines

Doktors der Naturwissenschaften (Dr. rer. nat.)

genehmigten Dissertation.

Vorsitzender: Univ.-Prof. Dr. K. Köhler

Prüfer der Dissertation:

1. Univ.-Prof. Dr. A. Türler
2. Univ.-Prof. Dr. R. Krücken
3. Priv.-Doz. Dr. A. Yakushev

Die Dissertation wurde am 14.06.2010 bei der Technischen Universität München eingereicht und durch die Fakultät für Chemie am 02.07.2010 angenommen.

Abstract

The goal of present work conducted in the framework of thesis was to develop a focal plane detection setup for the gas filled separator TASCA (**T**rans**A**ctinide **S**eparator and **C**hemistry **A**pparatus), which was recently installed at the GSI Helmholtzzentrum für Schwerionenforschung GmbH in Darmstadt, Germany. TASCA is one of a few recoil separators for the superheavy element (SHE) research; it has unsuppressed transmission efficiency and a capability to perform chemical investigations and highly efficient nuclear decay spectroscopy with SHE.

SHE exists solely because of enhanced nuclear stability, due to shell effects. Experimental studies have shown that cross sections for the synthesis of SHE decrease continuously, with exception of warm fusion reactions of doubly magic ^{48}Ca with actinide targets. Exploration of SHE nuclei is close to the border of present technical limitations and more efforts are needed to increase the efficiency and sensitivity in future experiments on SHE.

In the final commissioning experiment the nuclear fusion-evaporation reaction ^{244}Pu(^{22}Ne, 4-6*n*)$^{260\text{-}262}$Rf was studied at TASCA. Two types of a focal plane detector were tested in the measurements of the isotopes ^{260,262}Rf; the advantage of the DSSSD-type compared to the PSSSD-type was demonstrated. ^{262}Rf has been measured for the first time as an evaporation residue in a recoil separator, and a new value for the half-life of 190^{+100}_{-50} ms was obtained. Both isomeric states of ^{261}Rf have been produced with the ratio ^{261a}Rf:^{261b}Rf of 2.5:1 and measured after pre-separation in TASCA The TASCA transmission efficiency to the focal plane for the very asymmetric nuclear reaction ^{22}Ne+^{244}Pu was estimated to be 10.5%.

The goal of this thesis was accomplished that, based on results from numerous test experiments during the commissioning phase, the new focal plane detection system for TASCA was designed, built and tested. The implantation detector of the focal plane detector array consists of 2 DSSSD structures with a pitch of 1 mm on both sides and covers the focal plane area of 144 x 48 mm^2. This provides high collection efficiency of separated with TASCA reaction products, even from asymmetric reactions. The detection efficiency for a single alpha particle emitted from an implanted in the new focal plane detector evaporation residue is 72%. The good energy and spatial resolution

ensure the search for time- and position-correlated decay chains, which is extremely important for experiments on the synthesis of new SHE.

The new electronics consisting of 640 spectrometric channels was developed for the new TASCA focal plane detector. The combination of specially designed analogue electronic modules with a conventional digital electronics allowed to reduce the costs significantly.

The new detection system has been used in the experiment on the synthesis of element 114, produced in the nuclear fusion-evaporation reaction ^{244}Pu(^{48}Ca, 3-4n)$^{288-289}$114. Fifteen decay chains were observed from ^{288}114 and ^{289}114 at two beam energies. Decay modes, α-particle energies, and half-lives agree with those reported from the original experiments at Dubna Gas Filled Recoil Separator, and even higher cross sections were measured for 3n and 4n evaporation channels. A previously unobserved α-decay branch in ^{281}Ds has been observed leading to the discovery of the isotope ^{277}Hs. The observation of two of the ^{288}114 decay chains in the SIM demonstrates that TASCA is ideal apparatus for nuclear spectroscopy and for future chemistry experiments after preseparation.

Zusammenfassung

Das Ziel der Arbeit, durchgeführt im Rahmen dieser Dissertation, war die Entwicklung eines Fokalebenendetektionssystem für den gasgefüllten Separator TASCA (**T**rans**A**ctinide **S**eparator and **C**hemistry **A**pparatus), welcher vor Kurzem am GSI Helmholtzzentrum für Schwerionenforschung GmbH in Darmstadt installiert wurde. TASCA ist einer der wenigen Rückstoßseparatoren weltweit für die Erforschung superschwerer Elemente, hat eine sehr hohe Transmissionseffizienz und bietet die Möglichkeit chemischer Untersuchungen und hocheffizienter Kernzerfallsspektroskopie an SHE.

SHE existieren nur aufgrund erhöhter Kernstabilität, verursacht durch Schaleneffekte. Experimentelle Studien haben gezeigt, dass der Wirkungsquerschnitt für die Synthese von SHE kontinuierlich abfällt, mit der Ausnahme von warmen Fusionsreaktionen von doppelt magischem ^{48}Ca mit Aktinidentargets. Die Erforschung von SHE befindet sich nah am Rand der heutigen technischen Grenzen, deshalb sind größere Anstrengungen notwendig um die Effizienz und die Sensitivität bei zukünftigen SHE-Experimenten zu erhöhen.

Im letzten Inbetriebnahmeexperiment wurde die nukleare Fusionsreaktion ^{244}Pu(^{22}Ne,4-6*n*)$^{260\text{-}262}$Rf an TASCA untersucht. Zwei Typen von Fokalebenendetektoren wurden bei den Messungen der Isotope ^{260,262}Rf getestet. Es wurden die Vorteile des DSSSD-Typs im Vergleich zum PSSSD-Typ demonstriert. ^{262}Rf wurde das erste Mal als Abdampfungsrestkern in einem Rückstoßseparator gemessen und ein neuer Wert für die Halbwertszeit von 190^{+100}_{-50} ms wurde ermittelt. Beide isomere Zustände von ^{261}Rf wurden produziert und nach der Vorseparation durch TASCA mit einem Verhältnis von ^{261a}Rf:^{261b}Rf of 2.5:1 gemessen. Die Transmissionseffizienz von TASCA zur Fokalebene für die sehr asymmetrische Reaktion ^{22}Ne + ^{244}Pu betrug 10.5%.

Das Ziel dieser Dissertation, basierend auf vielen Testexperimenten während der Inbetriebnahme von TASCA ein neues Fokalebenendetektionssystem zu entwickeln, bauen und testet, wurde erfüllt. Der Implantationsdetektor der Fokalebenendetektoranordnung besteht aus 2 DSSSD Strukturen mit einer Streifenbreite von 1 mm beiderseits und bedeckt eine Fläche in der Fokalebene von

144 x 48 mm^2. Dies gewährt eine hohe Sammeleffizienz für Reaktionsprodukte, separiert durch TASCA, auch für sehr asymmetrische Reaktionen. Die Detektionseffizienz für ein einzelnes Alphateilchen, emittiert von einem implantierten Kern in der Fokalebene, beträgt 72%. Die gute Energie- und Ortsauflösung gewährleistet die Suche nach zeit- und positionskorrelierten Zerfallsketten, was extrem wichtig für Syntheseexperiment von neuen SHE ist.

Die neue Elektronik, bestehend aus 640 Spektroskopiekanälen, wurde für den neuen TASCA Fokalebenendetektor entwickelt. Die Kombination von speziell entwickelten Analogelektronikmodulen mit konventioneller Digitalelektronik führte zu einer deutlichen Kostenreduzierung.

Das neue Detektionssystem wurde erstmalig verwendet im Syntheseexperiment von Element 114, hergestellt in der Kernfusionsreaktion $^{244}Pu(^{48}Ca,3\text{-}4n)^{288\text{-}289}114$. 15 Zerfallsketten von $^{288}114$ und $^{289}114$ wurden beobachtet bei zwei Strahlenergien. Zerfallsarten, α-Teilchenenergien und Halbwertszeiten stimmten mit denen des Originalexperiments am Dubna Gas Filled Recoil Separator (DGFRS) überein, wobei höhere Wirkungsquerschnitte für den 3n und 4n Kanal gemessen wurden, als am DGFRS. Ein zuvor noch nie beobachteter α–Zerfall von ^{281}Ds wurde gemessen, welcher zur Entdeckung des Isotops ^{277}Hs führte. Die Beobachtung von zwei $^{288}114$ Ketten im SIM demonstrierte, dass TASCA ein ideales Instrument für die Kernspektroskopie und für zukünftige Chemieexperimente mit vorheriger Vorseparation ist.

Acknowledgements

This thesis arose from the research on superheavy elements conducted by the Institut für Radiochemie under the guidance of Prof. Dr. A. Türler and Dr. A. Yakushev, together with the Nuclear Chemistry Group at GSI Helmholtzzentrum für Schwerionenforschung GmbH.

I am grateful to many people for help, both direct and indirect, in accomplishing the goal and in writing this thesis. I owe a great deal to colleagues, who through their own research, advices and questions have enlightened and encouraged me; to my all friends and members of my family, who have supported and helped me during my stay in Germany.

First and foremost I would like to express gratitude to my mentor, Dr. A. Yakushev, who did a lot of efforts to prepare all chemistry experiments at GSI, and all TASCA experiments during last 7 years, especially studies on E114 at TASCA, and to bring them to success. He has made incredible contributions to the work of every PhD student in our group, and never asks for any recognition for it. Without him this thesis would never come into existence. He made me an offer to come to Munich and took the full responsibility for me. During the years of my stay in Germany I became a member of his family, and he was always ready to help, supporting me in every possible way. He taught me his many know-how's about superheavy element production, separation and detection. I want to use the possibility to thank him for everything that he did for me.

I gratefully acknowledge Prof. A. Türler for his confidence to allow an inexperienced in the field young man to develop the new TASCA detection device in the framework of such an important and exciting research project. He always supported my work and gave me a lot of freedom in accomplishing my research goals. A very important help from him to me was a bettering of my English in spoken and written, especially I am very thankful for the correction work by writing this thesis and articles. I am really happy that even after his move to Switzerland he always took care about me at the last step of my work.

Many thanks go to the Nuclear Chemistry group at GSI, where we spend so much time on our experiments. All members of the group were very helpful and working very professionally, and I have learned a lot from them. In particular, I would like to acknowledge Dr. M. Schädel, who always granted me his time for answering my

questions and was always ready to share with me his huge experience in the field; Prof. Dr. Ch. Düllmann, who organized many TASCA experiments, spent his time to improve my articles and made huge amount of TASCA calculations;, Dr. W. Brüchle, who sacrificed his time to explain me everything about ROMA, even being retired; Dipl.-Ing. E. Jäger, who helped with any problems concerning TASCA equipments; E. Schimpf and J. Krier, who performed a lot of work during design and construction them; Dr. A. Semchenkov, who made a very important contribution to the success of TASCA and was at any time ready to help. Special thanks go to the Software Department at GSI, personally to Dr. N. Kurz and Dr. H.-G. Essel for a very effective help with implementation of MBS and GO4 codes for the new detection system; and to Dr. J.M. Gates who as member of both RCM and GSI NC groups helped a lot with the analysis of the experimental results and writing.

I am positively impressed from an extraordinary team of coworkers, which I had an opportunity to meet every day at the Institut für Radiochemie and deeply appreciate the conditions, which they prepared for my research. I would like to thank for extensive support from our workshop, because without their fast and yet precise work no experiments would be possible.

Many thanks go to members of our small group, in particular to R. Schuber, who helped me to make things clear during my first steps; to J. Dvorak, who explained me a lot in science and programming; to R. Graeger, with whom we spend a lot of time during necessary preparations for the experiments, during long night shifts at GSI and during nice discussions, who became my good friend.

I acknowledge Prof. Dr. Petry and I. Kaul for their help with administrative tasks, which I myself didn’t master and for the care they took about me, especially during last month of my stay in Germany.

I would like to thank many collaborators, who participated in our experiments, directly or indirectly. My thanks go to the ACCULINNA group at Flerov Laboratory of Joint Institute for Nuclear Research in Dubna, who helped a lot in test experiments with new DSSSD and SSSSD detectors; and especially to my father, Dipl.-Ing. V. Gorshkov, who suggested a lot of brilliant ideas and is also the father of the new data acquisition system. To Dr. K. Eberhardt, Dipl.-Ing. D. Thörle and Dipl.-Ing. D. Liebe from Mainz University, who really mastered target preparation.

I want to thank M. Sc. M. Wegrzecki and his group from ITE Warsaw for careful work during the design and manufacturing of the new detectors. They start from scratch in the production of DSSSD and SSSD structures and fulfilled an excellent work. I have never saw him, but I am very grateful to him for the incredible help in my work

I would like to thank the staff and crew of the GSI UNILAC for providing stable intense beams and for providing their help. This work was supported by BMBF projects No. 06MT248, 06MZ223I and F&E Project between GSI and TU Munich.

And of course, where would I be without my family? My parents deserve special mention for guiding me to wisdom and curiosity and always gave me their full support in my ambitions. Many thanks go to my sister Elena. And special thanks to my girl-friend Natalia, who has always shown me her loving. I owe her for invaluable support, which she offered to me despite of her own hard work. I know she didn't like my work, because I was far, far away for so long time. Also I want to thank the family of Dr. A. Yakushev. During the years of my stay in Munich Sasha, Vera and Anton became like my second family - always glad to see me and ready to help. I want to thank all of them for helping to keep my spirit up.

Alexander Gorshkov

Contents

Chapter I

Introduction

Physical aspects in SHE research

1.1 Motivation

The fundamental goals of nuclear physics and nuclear chemistry are the characterization of elements and study of their physical and chemical properties. Because uranium (Z = 92) is the last naturally, in macroscopic quantities occurring element, all elements beyond uranium must be artificially created before being characterized. Elements up to Z = 100 can be synthesized in nuclear reactors, and those with Z > 100 are highly unstable and must be produced in nuclear reactions at particle accelerators. This thesis concerns the production and study of Super Heavy Elements (SHE) which have Z ≥ 104. The 5f electronic shell ends with lawrencium (Z = 103) and the SHEs begin in the seventh row of the periodic table, starting with filling the 6d shell. After the discovery of the first transuranium elements, neptunium and plutonium, in the following 65 years scientists synthesized and identified 25 new elements (Z = 93 − 118). The production of the heaviest elements becomes more and more difficult due to extremely low production rates and very short lifetimes. This challenging research field requires utilizing very effective recoil separators with detection systems of very high sensitivity.

For a long time it was believed, that the limit of the periodic table would be reached at element 108. Extremely short half-lives for spontaneous fission (SF) expected for nuclei with Z ≥ 108 would prohibit their identification. This number results from the balance of two fundamental nuclear parameters described by the liquid-drop model (LDM), the strength of the attractive nuclear force, which binds neutrons and protons together and creates a surface tension, and the repulsive electric force. However, like the electrons in an atom, also the nucleons in a nucleus form closed shells with “magic” numbers of nucleons. At the magic proton or neutron numbers 2, 8, 20, 28, 50, and 82, the nuclei have an increased binding energy relative to the average trend. Various theoretical models which took into account shell corrections [1-3] proposed that the next double closure shell beyond ^{208}Pb should be at proton numbers Z = 114 or 126,

and at neutron number N=184. Recent models based on the Nilsson-Strutinsky approach predicted strong shell correction energies and spherical shapes for nuclei with Z = 114 and N = 184 [4], whereas Hartree-Fock calculations predict highest stability at proton number Z = 126 and at the same neutron number [5]. This stabilization to the complete filling of proton and neutron shells results in lifetime enhancement against spontaneous fission. The prediction of magic numbers, although not unambiguous, was less problematic than the calculation of the stability of those doubly closed shell nuclei against fission. As a consequence, the predicted half-lives based on various calculations differed by many orders of magnitude [6-11].

Such an indication was also true for the other modes of radioactive decay such as α– and electron capture (EC) decays. Some of the half-lives approached the age of the universe, and attempts have been made to discover naturally occurring SHEs. Although discoveries were announced from time to time, none could be substantiated after more detailed inspection.

Shortly after the first shell model calculations were published, a hypothesis that the "superheavy" elements (SHE) located around this closed shell form an "Island of Stability" separated from the land of known nuclei by the "Sea of Instability" was formulated. Therefore, the physicists put an enormous effort to find these elements in nature but their endeavor was not successful. To find out the truth about the "Island of Stability" the consecutive synthesis of heavy elements was started in laboratories. The quest to find the limits of stability for nuclei has been one of the major driving forces in nuclear physics for about forty years up to now.

1.2. Nuclear models

The man-made SHEs have to be produced artificially in nuclear fusion reactions at appropriate particle accelerators. The transactinide elements have very low nuclear stability against α- and SF-decay due to their high nuclear charge and should not exist according to the phenomenological *"liquid drop model"*. The existence of transactinide elements with relatively long half-lives (on the order of milliseconds to minutes) can be explained by enhanced nuclear stability due to *"shell effects"*, where the potential energy (mass) of the ground state nucleus is reduced due to quantum mechanical effects. Both theoretical approaches are described in the following Sections.

1.2.1 Liquid drop model

To predict any physical properties of nuclei one of the major problems is to construct a simplified rule, which represents the general interactions of nucleons inside of a nucleus with solvable mathematical equations. If this rule can successfully describe at least a few previously measured nuclear properties and predict new properties that can be tested in new experiments, then it can be called a nuclear model [12].

The oldest nuclear model which approximates the nucleus as a drop of charged liquid with very low compressibility and attractive short-range force, holding the nucleons (molecules) together, is called the Liquid Drop Model (LDM) [13]. The LDM successfully predicts the binding energies in nuclei, and also explains the spherical shape of most nuclei. Based on the LDM, a semi-empirical mass formula (SEMF), also known as the *"Bethe-Weizsäcker formula"*, has been developed.

$$M = NM_m + ZM_p - \frac{B}{c^2} \tag{1.1}$$

The mass of nuclei is equal to the sum of the masses of all neutrons N and protons Z along with a term to take into account the extra stability caused by the binding force of the nucleons. B is the binding energy and it is given by Bethe-Weizsäcker as:

$$B = a_v A - a_s A^{2/3} - a_c Z(Z-1)A^{-1/3} - a_{sym}\frac{(A-2Z)^2}{A} + \delta \tag{1.2}$$

The first term is the volume term, and comes from the fact that density and binding energy per nucleon are approximately constant for all stable nuclei and that nucleons are assumed to interact only with the nearest neighbors. Because the nuclear radius is $r_{nucl} = r_0 A^{1/3}$, where $r_0 \approx 1.2$ fm, the volume is proportional to A, and a_v is determined to be 15.5 MeV by fitting to experimental binding energy data.

The second term takes into account that the nucleons on the surface of the nucleus do not have as many nearest neighbors as the nucleons inside of the nucleus, which causes the surface tension. The proportionality constant a_s is 16.8 MeV.

The third term takes into account the Coulomb repulsion of protons in the nucleus. Assuming a uniformly charged sphere, this term is then proportional to r_{nucl}^{-1} i.e. $A^{-1/3}$, and $a_c = 0.72$ MeV.

To account for the neutron-proton asymmetry, the fourth term is introduced, and the proportionality constant a_{sym} = 23 MeV.

The last term is included due to the tendency of likeliness of nucleons to pair up to form a more stable configuration. The pairing term can be represented as:

$$\begin{cases} \delta_0 = a_p A^{-3/4}, & \text{for even Z, N nuclei} \\ 0, & \text{for odd A nuclei} \\ -a_p A^{-3/4}, & \text{for odd Z, N nuclei,} \end{cases} \tag{1.3}$$

where a_p constant is determined to be 34 MeV.

1.2.2 Nuclear shell model

Over the years, as new knowledge was gained through experimental research, nuclear theoreticians have been able to modify, expand, and improve the Bethe-Weizsäcker equation to produce extremely accurate models. Each new discovery in the laboratory is used as a test for these models and provides motivation for further improvement of our understanding of the nucleus.

One of the very important nuclear properties that the LDM is not able to predict is the existence of *magic numbers*, i.e. neutron or proton numbers where the binding energies are much higher than for the surrounding numbers of protons or neutrons.

Certain protons and neutron numbers form shells, similar to electron shells in chemistry, that grant enhanced stability to nuclei, just as the closed-shell noble gases are known to be chemically very stable. While chemical closed-shells occur at electron numbers 2, 10, 18, 36, 54, and 86, the “magic” numbers of 2, 8, 20, 28, 50, 82, and 126 protons and/or neutrons have long been known to be particularly stable.

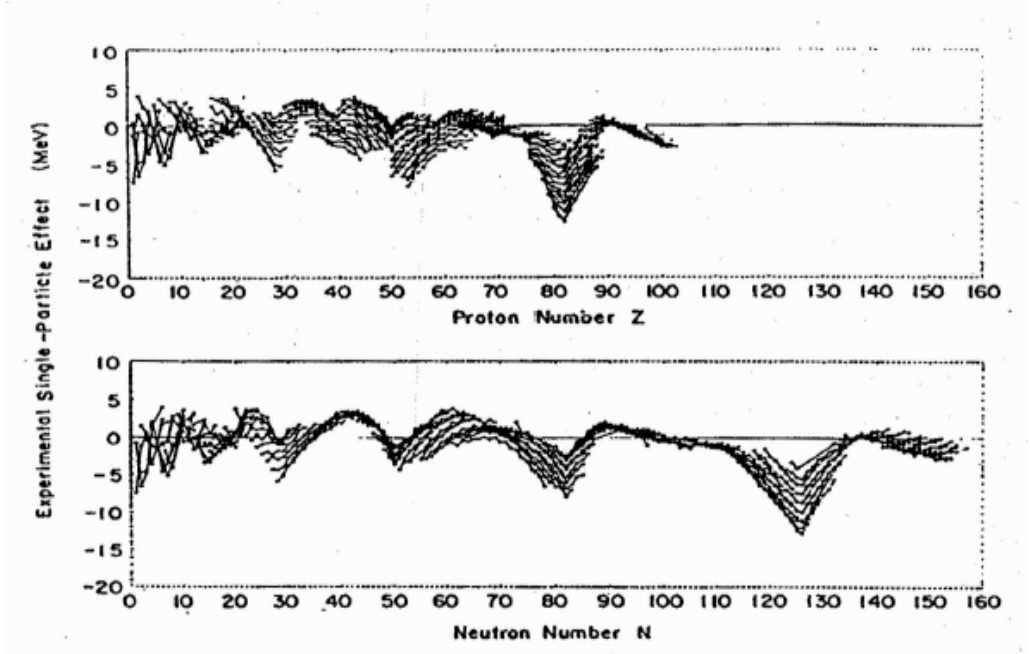

Figure 1.1: Difference in MeV between the experimental ground state mass and the mass given by a liquid drop semiempirical mass equation, uncorrected for shells. Note the extra stabilization energy at nucleon numbers 28, 50, 82, 126, mostly because of nuclear shell effects. Adopted from [14].

The magic numbers for neutrons can be clearly seen in Fig. 1.1 as local minima in the masses of nuclei. Clearly, there is a close association between improved stability and less mass (higher binding energy). The reference point in the figure is the liquid-drop mass, that is, the mass that is calculated for a nucleus by treating it as if it had properties similar to drops of a liquid. The difference between the experimental mass and the liquid-drop mass is the *shell correction or shell effect*.

As stated above, it was well known from the beginning of the study of nuclei that certain numbers of protons and neutrons gave unusual stability to nuclei. The nuclear shell model was developed in the late 1940s [15,16] as a reaction to unsuccessful attempts of previous models to explain a number of nuclear phenomena, most importantly the existence of magic numbers among others. The LDM explains the nuclear structure and properties on the basis of statistical contributions of all nucleons in the nucleus. The main idea of the nuclear shell model is in the independent motion of each nucleon in the central potential of all other nucleons.

Initially, the harmonic oscillator– and the square well potential were used to approximate the nuclear potential, but they were not able to reproduce magic numbers above 20 [17]. Later a more realistic potential, called Woods-Saxon potential, was used, but it still failed to predict all of the observed magic numbers.

Later Maria Goeppert-Mayer [18,19] improved the existing model starting with an almost square well and calculating the energies of the "single-particle levels". In these single-particle levels, the nucleons moved independently because any scattering interaction would require the particle to jump to a state with an energy higher than the interaction energy. Mayer took these levels and applied spin-orbit coupling between a spin of the nucleon and its motion, which resulted in the split of previously degenerate levels and accurately reproduced all of the magic numbers. The calculations with the harmonic-oscillator potential and with spin-orbit term are presented in Fig. 1.2.

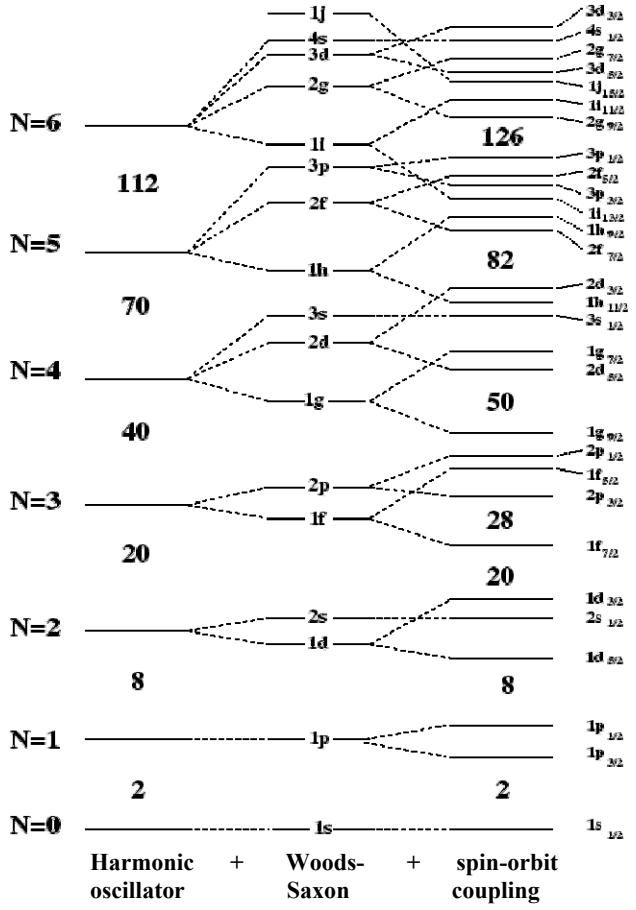

Fig. 1.2: Energy level pattern for nucleons calculated using three potentials. On the left side are the energy levels calculated with the harmonic oscillator potential. In the middle are the energy levels calculated by Woods-Saxon, and finally on the right side are the levels obtained by inclusion of the spin-orbit coupling term.

The shell model works well for spherical nuclei, because the calculated levels are based on a spherical nuclear potential. However, nuclei with $150 \leq A \leq 190$ and $A > 230$ are found to be deformed and it is not possible to use a spherical nuclear potential for calculation of their nuclear levels.

One of the theoretical tools to understand deformed nuclear structures is the *deformed shell model* or *Nilsson model* [20,21]. The Nilsson model describes the single-particle motion of a proton or a neutron in an axially symmetric nuclear potential.

Originally Nilsson used a modified harmonic oscillator potential to take into account deformation of the nuclei [21], but later on more realistic nuclear potentials, such as the deformed Woods-Saxon potential, have been applied. The Nilsson diagram displaying the energy levels of the more realistic folded-Yukawa single-particle potential shows enhanced stability of deformed nuclei at and close to $Z = 108$ and $N = 162$ (see Figure 1.3).

However, the Nilsson model failed to predict reasonable deformation energies at large deformations or the existence of the second minimum in fission barriers of actinides.

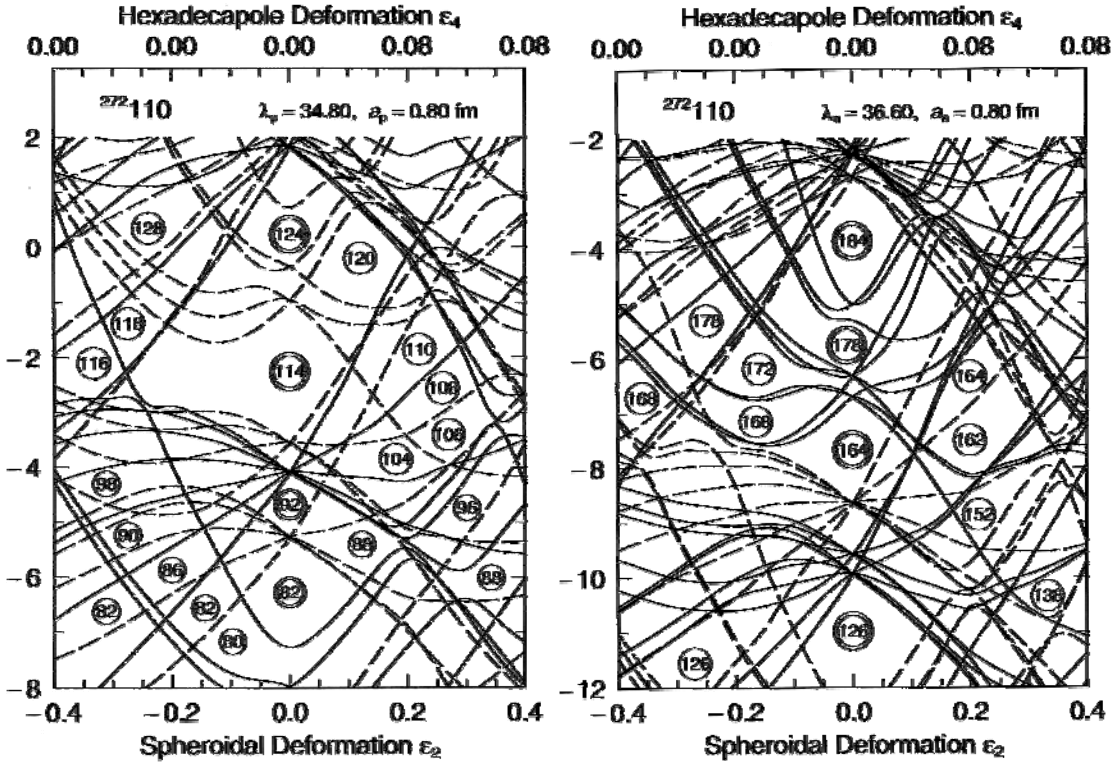

Fig. 1.3: Proton and neutron folded-Yukawa single-particle level diagram for the nucleus ^{272}Ds plotted versus spheroidal and hexadecapole deformation. Adapted from [22].

1.2.3 Strutinsky Macroscopic-Microscopic Model

The LDM model describes the properties of most nuclei well, but does not explain the existence of SHEs and their stabilities. Hence, corrections are needed to get an agreement with experimental observations and to make extrapolations of macroscopic nuclear properties, like masses and binding energies, to the region of SHE.

To solve the problems associated with the LDM model and to quantitatively describe shell closures; Strutinsky used the density of single-particle states, from the Nilsson model for deformed nuclei [21]. The Strutinsky model can reproduce the experimental nuclear ground state energies if the proton and neutron shells and the paring energy corrections to the LDM energies are included taking into account the deformation of nuclei [1,23].

Unfortunately, when one attempts to calculate the mass of a nuclide using shell-model states, the results are not satisfactory. The best method to calculate the total energy E of a nucleus is to use the so-called "macroscopic-microscopic" approach. The LDM is used to establish "baseline" macroscopic masses, which give the general trend. Then, the method developed by Strutinsky may be used to calculate the microscopic shell correction. Summing these two quantities gives a much more accurate depiction of nuclear masses:

$$E = \underbrace{E_{LDM}}_{Macroscopic} + \underbrace{\sum_{p,n}(\delta S + \delta P)}_{Microscopic} \tag{1.4}$$

Here E_{LDM} is the liquid drop model energy (macroscopic part), and (δS) the shell and (δP) the pairing corrections to this energy (microscopic part). The difference between the LDM and macroscopic-microscopic approach easily can be seen on Fig. 1.4.

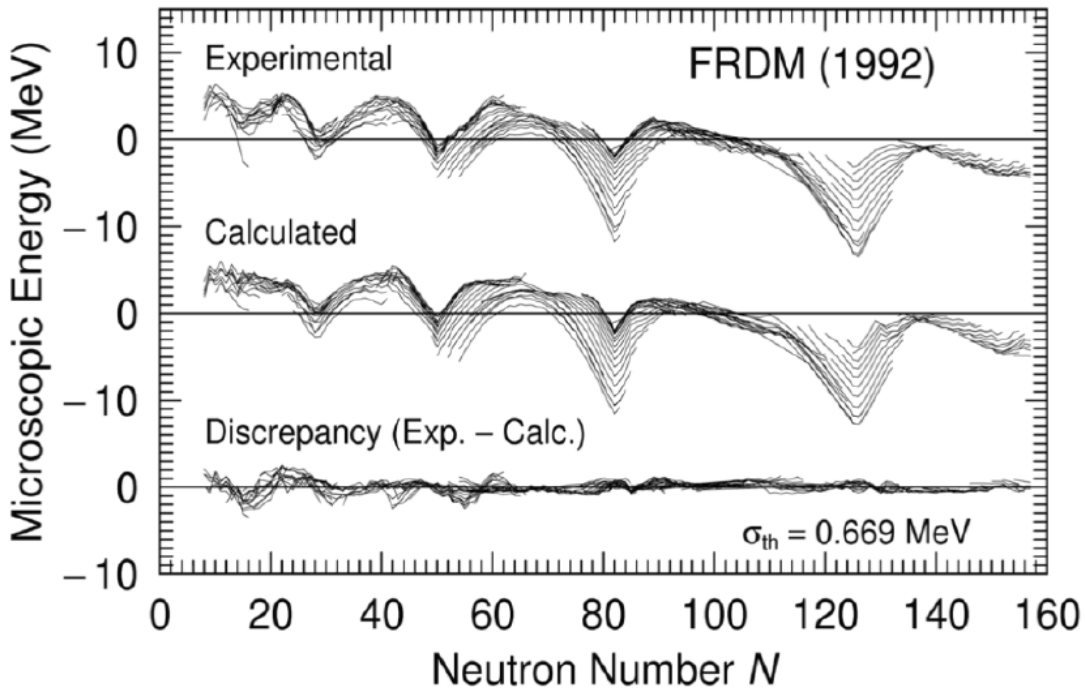

Fig. 1.4: The shell correction energy as a function of neutron number is shown. The top part represents the experimental shell effects which are defined as the difference in MeV between the experimental ground state mass and the mass given by a liquid drop semiempirical mass equation, uncorrected for shells. The middle section represents the theoretical shell effects calculated as described in [24]. The bottom section is the difference between the measured and the calculated values. Adapted from [24].

The stabilization of SHEs due to shell effects can be demonstrated by investigation of their fission barriers. The results of a LDM and a macroscopic-microscopic calculation of the fission barrier for elements up to 116 are shown in Fig. 1.5. A strong disagreement is found in the region of the heaviest nuclei between the height of fission barrier B_f (Fig. 1.5a)) and the probability of spontaneous fission (Fig. 1.5b)) which, as it is well known, is determined not only by the height, but also by the shape of the fission barrier. The smooth decreasing of the liquid drop fission barrier height with increasing fissility parameter $x \sim Z^2/A$ cannot explain the variations of the fission barriers of heavy nuclei, namely the two times higher barrier in ^{208}Pb ($B_f \approx 28$ MeV) and the practically unchanged fission barrier heights in the isotopes of the actinides from U to Fm ($B_f \approx 6$MeV). As a result, the partial spontaneous-fission half-lives T_{SF}(th) strongly differ from T_{SF}(exp), see Fig. 1.5b). Similar effects were found for other important properties of heaviest nuclei, such as the α-decay energy Q_α and the partial half-life T_α [25]. Shell structure effects are important for all nuclei; however, for the SHE their role is more essential as these nuclei would not exist without enhanced nuclear stability.

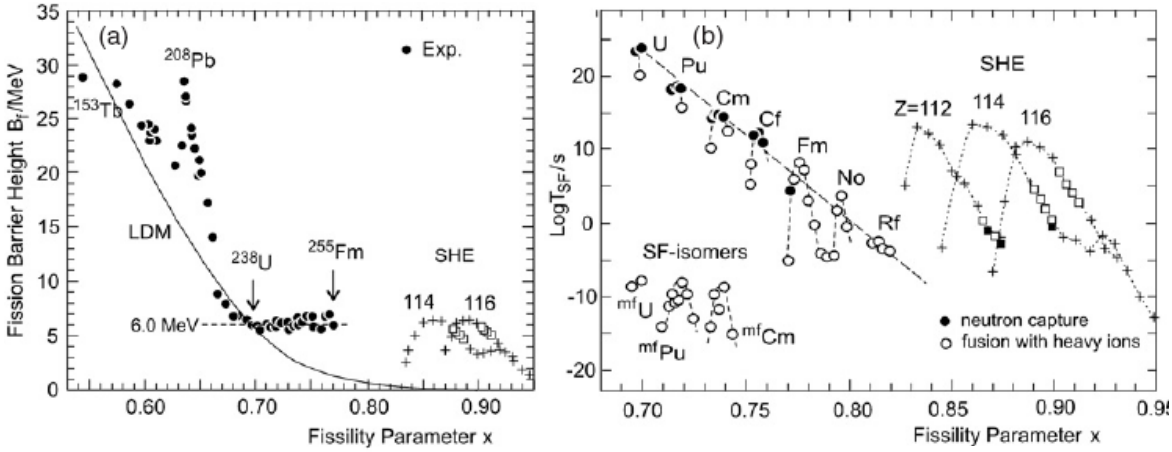

Fig. 1.5: a) Fission barrier heights as a function of the fissility parameter $x = (Z^2/A)/(Z^2/A)_{crit}$ at $(Z^2/A)_{crit} = 50.883$. The black points are experimental data, the solid line is a calculations with the liquid-drop model, crosses are calculated fission barrier heights in the macroscopic-microscopic model for the isotopes of elements 114 and 116 [26], the open squares are nuclei, produced in the ^{242,244}Pu, ^{245,248}Cm + ^{48}Ca reactions. b) Half-lives with respect to spontaneous fission as a function of the fissility parameter x. The black points and the open circles denote experimental values T_{SF}(exp) for spontaneous fission of even–even nuclei from the ground and isomeric states. The dashed line is an extrapolation into the transactinide region before the synthesis of heavy nuclei in heavy-ion-induced reactions (macroscopic concept). Crosses are calculated values T_{SF}(th) in the macro-microscopic model for even–even isotopes of elements 114 and 116 [26], open squares are nuclei, produced in the reactions ^{242,244}Pu, ^{245,248}Cm + ^{48}Ca, black squares are isotopes for which the SF-half-lives have been measured. Adapted from [27].

1.3 Stability in the SHE region

Depending on the used model [6,28,29,30], the theoretically predicted center of stability is located at $Z = 114$, 120, 126 and at $N = 184$. SHEs were predicted to form an "Island of Stability" surrounded by nuclei with very short half-lives.

Including higher orders of deformation, Sobiczewski improved previously performed calculations [31,32,33]. Figure 1.6 shows a contour map of shell correction energies E_{sh} for elements between Pb and element 120 plotted as a function of Z and N [26,34]. E_{sh} is defined as the difference between the total potential energy for the equilibrium shape taking into account the deformation and the macroscopic part of the potential energy for the spherical shape. The values indicated on the contour lines represent this shell correction energy (in MeV) for differing values of Z and N. One can see that E_{sh} has three minima in this region. The first and the deepest one is at the doubly magic spherical ^{208}Pb (E_{sh} = -14.3 MeV); the second one lies near the doubly magic deformed ^{270}108 (E_{sh} = -7.2 MeV), which is predicted in [32,35]; the third one at

the ^{298}114 (E_{sh} = -7.2 MeV) has been predicted to be again a doubly magic spherical nucleus, the next one to the last experimentally known double-magic ^{208}Pb [2,3,36]. The plotted points indicate nuclei known at that time. Besides these three minima, there appears a rather wide plateau around the nucleus ^{252}Fm, which, although having a smaller shell correction (E_{sh} = −5.2 MeV) may be considered as a nucleus with closed deformed sub-shells [32,35].

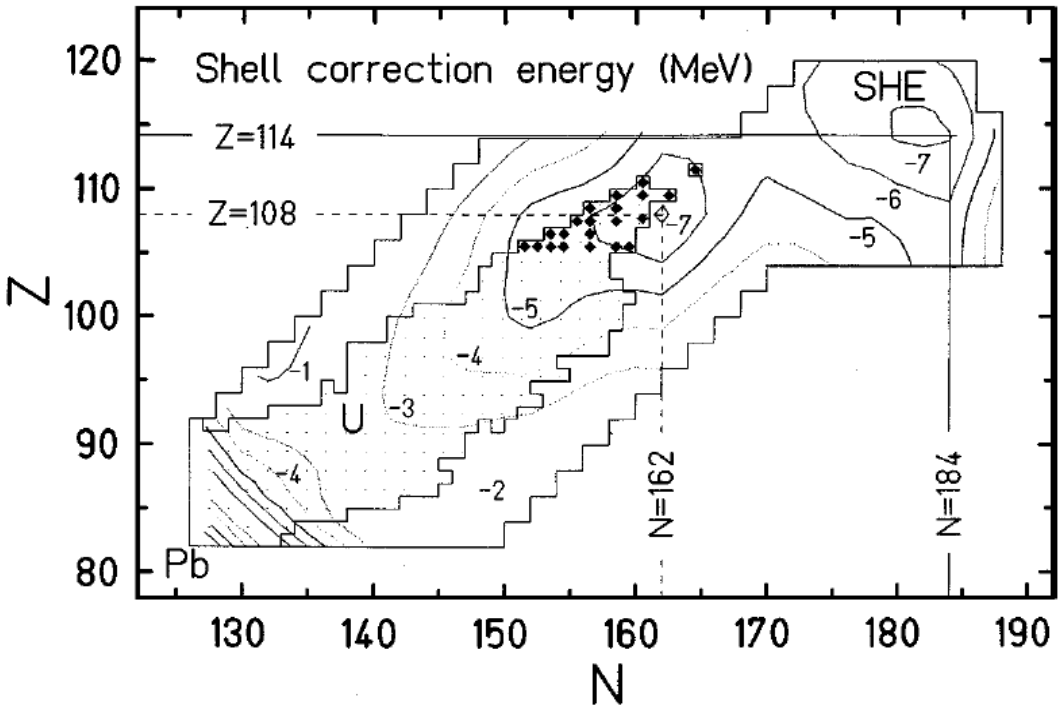

Fig. 1.6: Contour map of the ground-state shell correction energy E_{sh} [26,34].

The appearance of the region of deformed superheavy nuclei around the second minimum with values of the shell correction energy as large as in the case of ^{298}114 reveals, that there is a "Peninsula of Stability", which stretches further than previously thought and includes also the spherical superheavy nuclei [37].

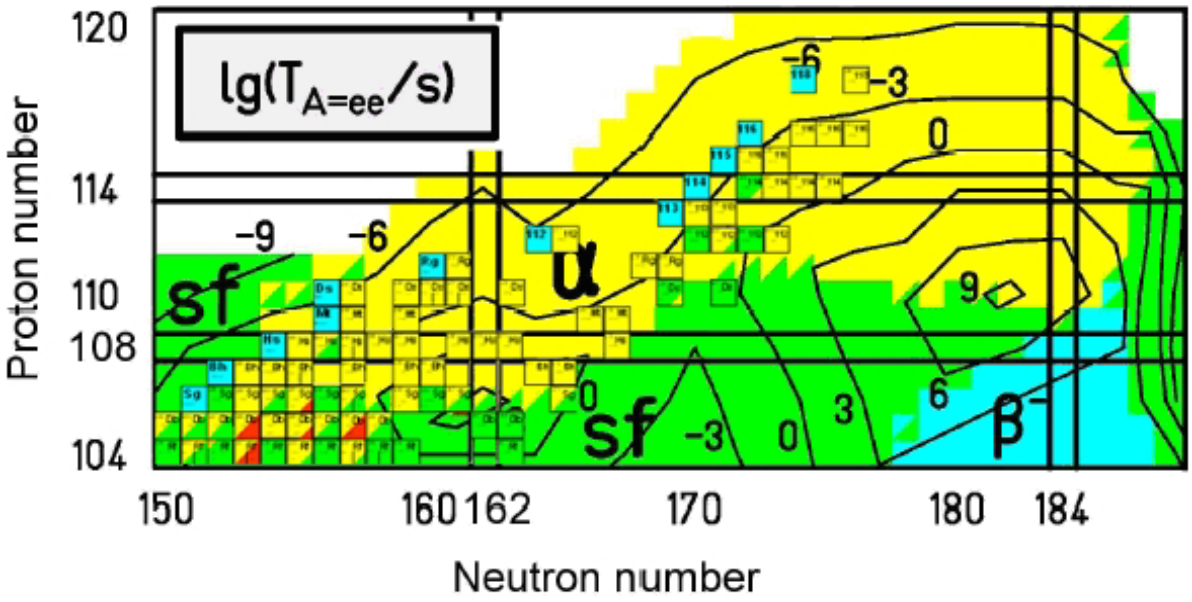

Fig. 1.7: Decay scenario in the region of SHE for even-even nuclei. Adapted from [38]. The synthesized nuclei from Rf to E118 are also shown for comparison.

In order to be able to estimate the real feasibility of experiments aimed at the synthesis of new elements, it is necessary to understand at what distance from the regions of known nuclei are the nuclides to be looked for and what are the possible decay scenarios, the decay modes, and the half-lives. Based on the calculations of shell correction energies presented in Fig. 1.6 one can calculate the partial half-lives for different decay modes resulting in a landscape of the most probable decay modes for each nucleus in the SHE region. Fig. 1.7 presents the comparison between the calculated landscape and the upper end of the chart of nuclides from Rf to element 118. From the decay scenario can be derived, that most likely the decay chains originating from SHE isotopes should usually consist of a few consecutive alpha particle decays, while the last member of all SHE decay chains are expected to undergo SF. As one can see in Fig.1.8, the experimental results are in a very good agreement with the calculations.

1.4 Experimental evidence for Z = 108, 114 and N = 162, 184 shells

The first attempt to confirm the existence of the N = 162 neutron shell as indication of increased stability in the region of deformed SHE around ^{270}Hs was performed by Lazarev *et al.* [39]. In the reaction ^{248}Cm + ^{22}Ne four α-α-(α) and six α-SF decay chains were detected and attributed to ^{265}Sg and ^{266}Sg, respectively. This assignment was based on the decay properties of ^{261}Rf and ^{262}Rf known at that time [40,41,42]. A half-life of 2 – 30 s for ^{266}Sg was derived by Lazarev *et al.* [39], which was interpreted as an indication of increased stability. A short-lived isomeric state of ^{261}Rf with a SF branch was discovered in the experiment devoted to discovery of element 112 [43,44]. Seven decay chains were detected during the first experiment on the Hs chemistry performed by Düllmann *et al*. and assigned to ^{269}Hs or tentatively to ^{270}Hs [45,46]. Again, the assignment was made according to the decay properties of ^{261,262}Rf and ^{265,266}Sg known at that time. In 2004-2008 a number of chemistry experiments in the region Z = 108 were performed by the Munich group in order to study more precisely the decay properties of ^{270}Hs. [47-49]. 25 decay chains from three Hs isotopes were detected. The tentative assignment made in [45,46] has been not confirmed, new decay properties for ^{270}Hs, ^{266}Sg, and ^{263}Rf, as well as the new isotopes ^{271}Hs, and ^{267}Sg have been observed [47,48] (see Fig. 1.8).

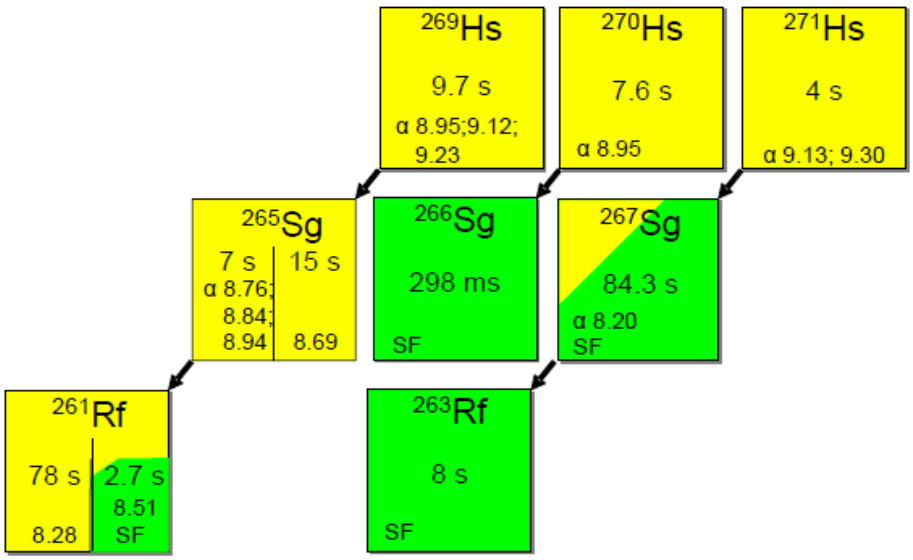

Fig. 1.8: Decay properties of nuclei, determined from TUM chemistry experiments of Hs chemistry. Five new nuclides were measured, including the doubly magic nuclide ^{270}Hs [48,50].

It was the first unambiguous observation of the doubly magic nucleus ^{270}Hs, while the existence of the closed deformed shells at Z=108 and N=162 has been confirmed. The comparison of calculated Q_{α}-values of even-even nuclei [51,52] with experimentally observed values [53,54,55] for nuclei with Z from 102 till 118 is shown in Fig. 1.9. The measured α-decay energies for ^{269,271}Hsare higher than in the case of ^{270}Hs, and a big difference in α-decay energies of ^{271}Hs (N = 163) and its daughter ^{267}Sg (N = 161) strongly support the attribution of the shell closure to N = 162 due to the existence of a local minimum in Q_{α} values at N = 162 and a large gap between Ds and Hs isotones. ^{270}Hs is the first experimentally observed even-even nucleus on the predicted N = 162 neutron shell. This experimental data provided an important reference point for theoretical models and clearly showed the enhanced nuclear stability at Z = 108 and N = 162.

A recent experiment at the DGFRS in Dubna was aimed at the synthesis of Hs isotopes via the reaction ^{226}Ra(^{48}Ca,xn)$^{274-x}$Hs and resulted in observation of 6 ^{270}Hs decay chains. The decay properties of the even-even nuclei ^{270}Hs and ^{266}Sg have been confirmed and the half-life of doubly magic ^{270}Hs has been measured for the first time [56]. The decay properties of Hs isotopes and their daughters are summarized in Fig. 1.8.

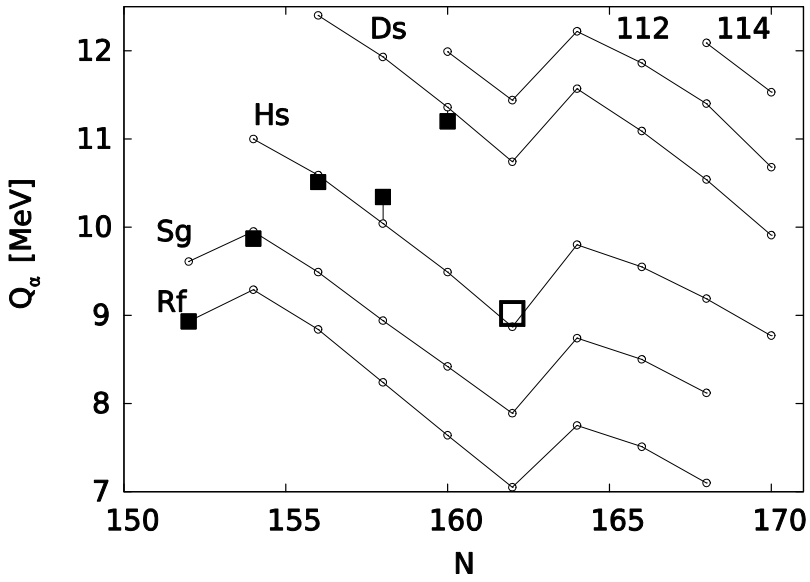

Fig. 1.9: The comparison of Q_{α} values from theoretical calculations [51,52] and experimental data [53,54,55] for even-even nuclei. The Q_{α} value obtained in [47] for ^{270}Hs is depicted with an open square. Adapted from [47].

In light of the new knowledge about the SF decay branch of ^{261}Rf and the decay properties of ^{265,266}Sg, the attribution of the decay chains to Sg isotopes from all previous experiments was reexamined [57]. New experiments to study the decay properties of Rf isotopes are needed. In the framework of this work, we have performed experiments on Rf isotopes, where both isomeric states of ^{261}Rf have been produced and measured as evaporation residues, and a new value for the half-life of ^{262}Rf has been measured at TASCA. These experiments are described in Chapter 4.3.

Elements with Z = 113 − 118 and heaviest isotopes of element 112 were synthesized at FLNR Dubna using doubly magic ^{48}Ca projectile and various actinide targets. These reactions allowed studying more neutron-rich isotopes, which are closer to the region of spherical SHE and for which also longer half-lives are expected. An excellent overview can be found in [27]. The last unknown element in the 7th row of the periodic table of the elements, element 117, has been synthesized very recently at the DGFRS [58]. Some of the discovered isotopes were observed in cross-bombardment experiments. However, as the chains end by spontaneous fission genetic relations to known nuclei cannot be used, making a direct assignment difficult. An independent confirmation is necessary. The decay properties of ^{283}112 were confirmed in experiments on the chemistry of ^{283}112 produced in the reaction ^{48}Ca + ^{242}Pu after α-decay of ^{287}114 conducted in Dubna by the PSI/FLNR group [59] and in an experiment conducted at SHIP (GSI Darmstadt), in which the reaction ^{48}Ca+^{238}U was investigated [60]. Recently, the synthesis and decay properties of four E114 isotopes produced with ^{48}Ca beam and ^{242}Pu and ^{244}Pu targets were confirmed at the Berkeley Gas filled Separator (BGS) in Berkeley and at TASCA, GSI in Darmstadt. The TASCA experiment for studies on E114 will be described in more details in Chapter 6.3.

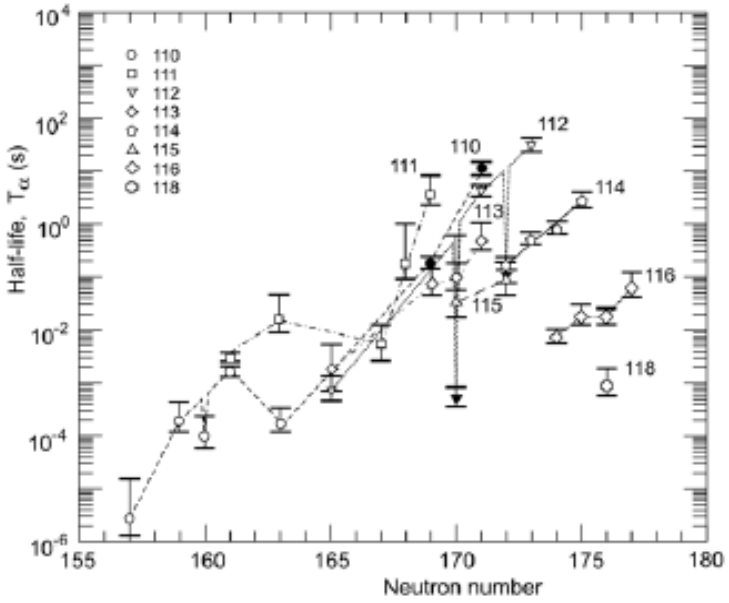

Fig. 1.10. The α-decay half-life of the heaviest nuclei depending on the neutron number. Adapted from [27].

The measured increasing relative stability of SHE with Z ≥ 112 with increasing neutron number has been interpreted as the existence of the Island of Stability close to the closed shell at N = 184. However, the position of the closed proton shell at Z=114, Z=120, or at Z = 126 could not yet be located definitely. The heaviest nuclei which have been synthesized are still too neutron-poor. To reach an area close N = 184, the fusion reactions of ^{244}Pu and ^{248}Cm nuclei with heavier projectiles, such as ^{58}Fe or ^{64}Ni, or future intensive beams of radioactive neutron-rich nuclei have to be used.

1.5 Synthesis of SHE

As SHEs have not been found in nature, the only method known today to synthesize superheavy nuclei is via nuclear fusion of two lighter nuclei at suitable particle accelerators. The understanding of the path from the event of fusion to the final product of the superheavy element is not complete and thorough yet, however, new approaches and experimental results steadily bring more insight into the process.

1.5.1 Fusion reactions

The bombardment of thin targets by a beam of projectiles is a common method to produce transactinides and has several possible outcomes. The creation of SHE as a compound nucleus (CN) is the result of a complete fusion reaction. In the fusion reaction the projectile has to have an energy higher than the fusion barrier, due to the

effective Coulomb force between the target and the projectile nuclei. The fusion probability is determined by the ratio of surface tension versus Coulomb repulsion. The last one is strongly depend on the asymmetry of the reaction partners (the product $Z_1 \times Z_2$ at fixed $Z_{CN} = Z_1 + Z_2$). In fusion reactions towards SHE the product $Z_1 \times Z_2$ reaches extremely large values ($Z_1 \times Z_2 > 1000$) and the fission barrier height decreases rapidly. For these reasons the formation of SHE is hindered by a high probability for re-separation in the entrance channel and by a high probability for fission in the exit channel.

For the classification of the types of reactions the impact parameter is important, which describes the centrality of the collision. If the products are the same as the reactants, then this is classified as a scattering reaction, and depending on the final states of the products two types of scattering reactions can take place [61]. If the projectile nucleus interacts with the target nucleus at large impact parameters, the incident projectile is reflected, corresponding to elastic scattering (products are in their ground states). With increasing the impact factor (corresponding to non-central collisions), the angular momentum increases and the nuclei are re-separated by centrifugal forces (the products are in excited states). Another reaction type are transfer reactions, a reaction where a few nucleons are transferred between the projectile and the target. Both scattering reactions and transfer reactions are direct reactions, reactions in which only few nucleons interact during the reaction and participate in the momentum and energy transfer.

In case of central or nearly central collisions the opposite to direct reactions and the most important for the formation of SHE complete fusion reactions takes place, reactions where the incident particle reacts with the whole target nucleus and the energy and momentum are equally shared between all nucleons in the resulting nucleus [61]. Because the CN is produced in a highly excited state and the fission barrier is lower than the excitation energy, the newly created CN undergoes fission within 10^{-20} s or it has to de-excite via particle emission. The emitted particles carry away a portion of the excitation energy, and more than one particle may be emitted in this process. Neutron emission in de-excitation is energetically more favorable than charged particle emission due to the fact that neutrons do not need to overcome the Coulomb barrier. The probability of survival of the CN is determined by the ratio of the probability of neutron evaporation and γ-emission versus fission of the compound nucleus. In SHE formation,

fission of the CN occurs much more often than particle emission, resulting in low production rates. The fusion reaction mechanism is described in more detail in Section 1.4.3.

1.5.2 Cold and Hot Fusion

Depending on the excitation energy of the compound nucleus (E*), two types of fusion reactions leading to the synthesis of SHE are distinguished: (i) "cold" fusion reactions with $E^* \sim 10 - 20$ MeV (1*n* or 2*n* evaporation channel), (ii) "hot" fusion reactions at $E^* \sim 30 - 50$ MeV (evaporation of 3 – 5 neutrons).

Cold fusion reactions are typically reactions of relatively heavy projectiles with ^{208}Pb or ^{209}Bi as targets. Due to the closed proton and neutron shells in ^{208}Pb and the neutron shell in ^{209}Bi, these reactions have large negative *Q*-values, which are responsible for the formation of rather low excited compound nuclei. Because of the symmetry of masses of target and projectile, cold fusion reactions are often called "symmetric", or "more symmetric" reactions.

The other type of fusion reactions with rather high excitation energies has the name hot fusion reactions. These are asymmetric reactions, where actinides are used as targets, and light projectiles have typical masses between A=12 and 40. This type of reaction has larger fusion cross sections, but the survival probabilities are lower due to the higher E^* of the CN.

Cold fusion reactions lead to more neutron deficient isotopes than those from hot fusion reactions.

In reactions of the doubly magic ^{48}Ca projectile with actinide targets, lower excitation energy of the CN can be reached again due to larger negative *Q*-values. This improves the survival probability. Such reactions sometimes are referred to as "warm" fusion. The production cross sections in warm fusion reactions are significantly higher compared to other combinations of projectile and target in cold and hot fusion reactions. The advantages of both production ways are combined in warm fusion reactions: lower fusion barrier, higher fusion probability and a "colder", less excited CN. Using reactions with ^{48}Ca as projectile, the elements with $Z = 113 - 118$ have been discovered. A compilation of experimental cross sections for both types of reactions is presented in Fig. 1.12.

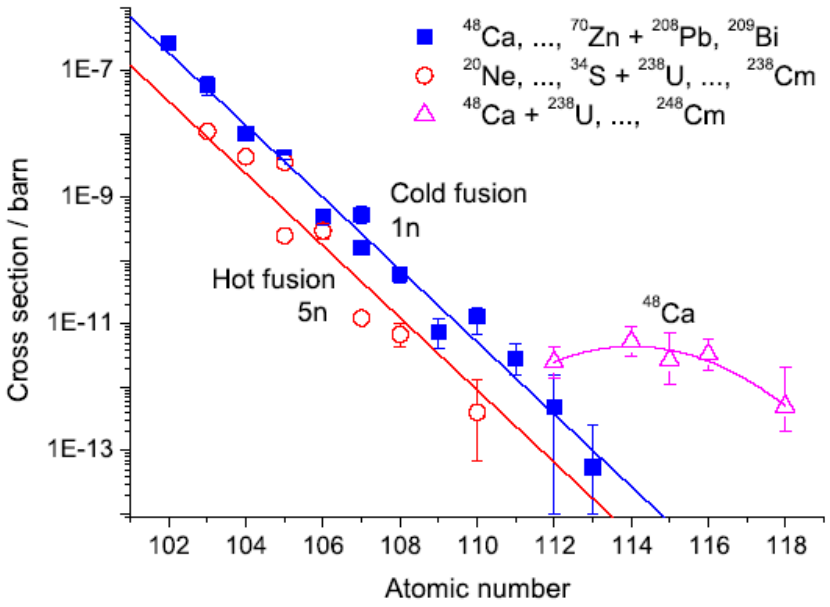

Fig. 1.12: Experimental cross sections for the formation of nuclei with Z ≥ 102 in (■)the 1n evaporation channel of cold fusion reactions, (○) the 5n channel of hot fusion reactions, and (Δ) the fusion reaction with the ^{48}Ca + actinide targets. The curves are drawn to guide the eye. Adapted from [50].

Producing elements beyond fermium, the increasing Coulomb repulsion starts to severely affect the fusion cross sections. A continuous decrease of the cross sections from microbarns (for nobelium synthesis) down to picobarns (for the synthesis of element 112) was observed. As can be seen, for both cold and hot fusion reactions the decrease of the cross sections has the same slope. Surprisingly, the cross sections of reactions with ^{48}Ca projectiles remain almost unchanged at a few picobarns to fractions of picobarn for all reactions with actinide targets.

1.5.3 Fusion reaction mechanism

Theoretical models that attempt to reproduce reaction cross sections are generally in a form of a product of three factors:

$$\sigma_{tot} = \sigma_{cap} \cdot P_{CN} \cdot P_{surv} \qquad (1.5)$$

The first term, σ_{cap}, is the capture cross section which corresponds to the probability for two nuclei to overcome the Coulomb barrier. The probability to form a compound nucleus is P_{CN}, and the probability that the nucleus will de-excite by neutron and γ-ray emission and form the residual nucleus rather than fission is P_{surv}.

There are many variables with a strong influence on cross section that determine if a nuclear reaction will proceed to CN formation and many different processes can

take place instead. When two nuclei, touch they may separate into a projectile-like fragment (PLF) and a target-like fragment (TLF), into fragments resulting from deep inelastic collision (DIC), or proceed directly to the quasi-fission (QF) channel, i.e., a fission-like process that occurs before CN formation. A three-dimensional plot of potential energy as a function of elongation (the distance between the centers of two nuclei) and mass asymmetry $(A_1 - A_2)/(A_1 + A_2)$ is given in Fig. 1.13 to demonstrate possible paths of nuclear reactions after the contact point. Two points of contact corresponding to two different reactions, one hot fusion (^{48}Ca + ^{248}Cm) and one cold fusion (^{88}Se + ^{208}Pb) producing the same CN ^{296}116 are also shown in Fig. 1.13.

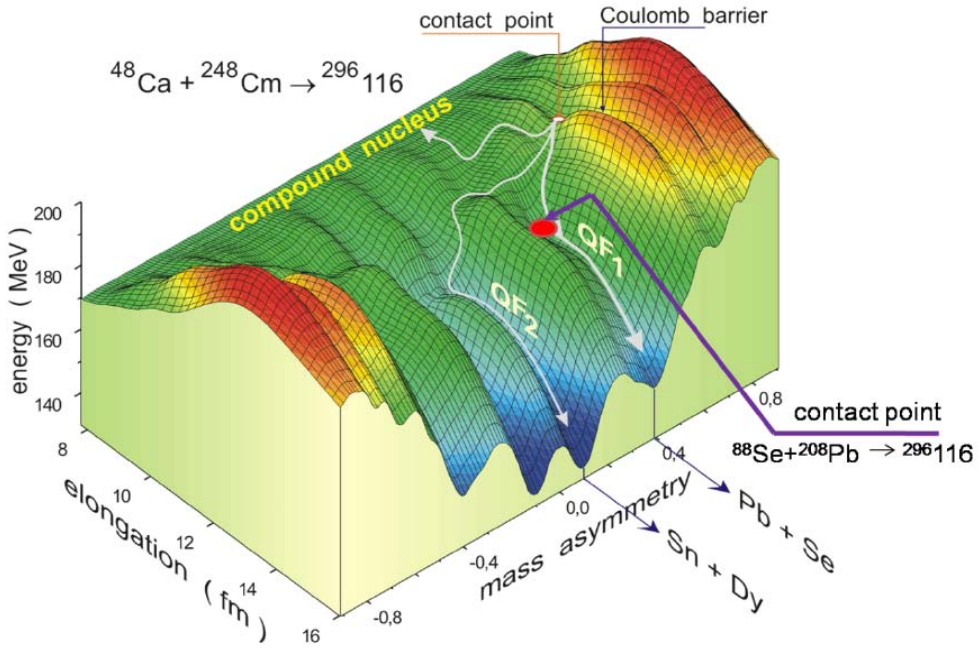

Fig. 1.13: An example of potential energy as a function of elongation (the distance between the centers of two nuclei) and mass asymmetry in the ^{48}Ca + ^{248}Cm reaction is shown as a topographical landscape. QF_1 and QF_2 are two possible quasi-fission paths. Adapted from [62].

In the case of the ^{88}Se + ^{208}Pb reaction, at the point of contact the potential energy is lower than the ground state potential energy of the CN. Therefore it is an uphill process to reach the CN configuration and it requires a high excitation energy which makes the system unstable with respect to quasi-fission and deep-inelastic processes. However, for the hot fusion reaction ^{48}Ca + ^{248}Cm, the potential energy at the point of contact is above the ground state CN energy, and it is more probable to reach the CN configuration in this case. However, a significant number of trajectories go through the quasi-fission valley, and thus the probability of CN formation in the hot fusion reaction

is by no means large, just significantly larger than it is for the cold fusion reaction. This is the reason why cold fusion reactions are not favorable for production of super-heavy elements with $Z \geq 112$.

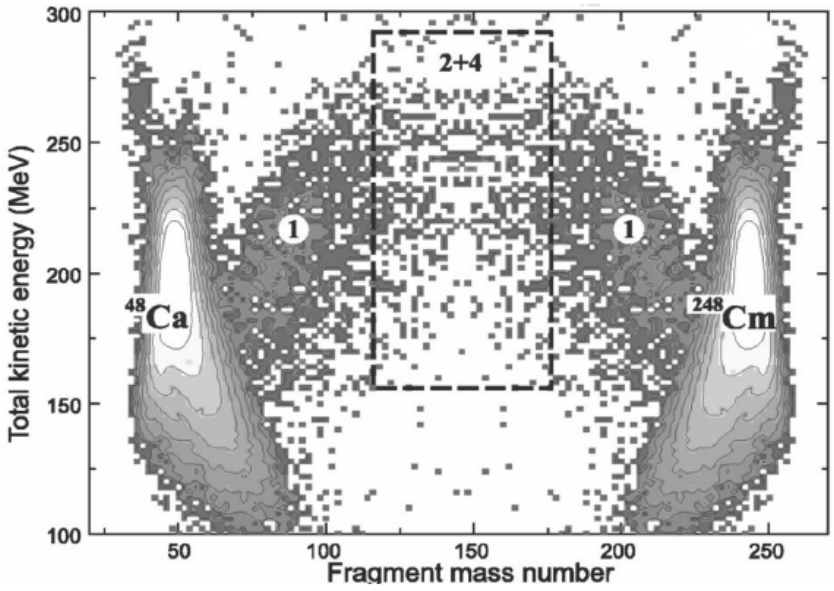

Fig. 1.14: Total kinetic energy (TKE) of fragment masses in the reaction $^{248}Cm(^{48}Ca,xn)^{296-x}116$. The numbers 2+4 refer to the region of fission of CN, 1 denotes the area of quasi fission. Both the projectile and target masses are seen, originating from quasi elastic scattering. Adapted from [63].

The difference of quasi fission and fission of a CN can be seen when observing the mass distribution of fission fragments experimentally. However, these two mechanisms have a smooth transition as can be seen in Fig. 1.14. It shows that nucleon transfer products around the target and projectile are produced in vast amounts. The next probable way is the quasi fission process leading to fragments with masses around A = 100 and A = 200. Events originating from the fission of the formed compound nucleus have a more symmetric distribution around a mass A = 150 (area marked within square). Further details can be found e.g. in [63,64].

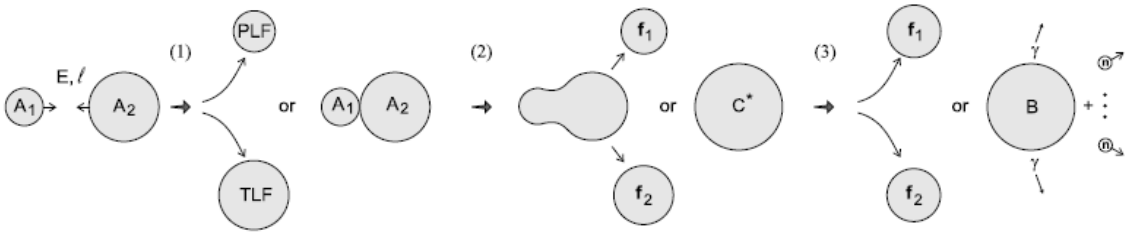

Fig 1.15: Fusion reaction dynamics.

The production cross section of a cold residual nucleus *B*, which is the product of neutron evaporation and γ-emission from an excited compound nucleus *C*, formed in the fusion process of two heavy nuclei $A_1 + A_2 \rightarrow C \rightarrow B + xn + N\text{g}$ at c.m. energy *E* close to the Coulomb barrier in the entrance channel, can be decomposed over partial waves and written as follows (Fig. 1.15).

$$\sigma_{ER}^{xn}(E) \approx \frac{\pi\hbar^2}{2\mu E}\sum_{l=0}^{\infty} f(B)P^{HW}(B,l,E)P_{CN}(B,l,E^*)dB \cdot P_{xn}(l,E^*) \tag{1.6}$$

The *CN* excitation energy at the Coulomb barrier depends on the barrier height and reaction *Q*-value, thus on the (*B*-*Q*) value. On the other hand, the CN formation probability P_{CN} strongly depends on the reaction asymmetry.

$$P_{CN}^0 = \frac{1}{1+\exp\left[\dfrac{Z_1Z_2-\zeta}{\tau}\right]} \tag{1.7}$$

Because of the extremely low production cross sections in this region it is very important to chose the most promising nuclear reactions for the production of new nuclides. The evaporation residue cross sections depend on entrance channel parameters (asymmetry, binding energy in the target and projectile nuclei, excitation energy at the fusion barrier and *Q*-value) and on the survival probability of the compound nucleus (*CN*) (fission barrier, excitation energy of the *CN*). However, the survival of heavy nuclei depends not only on the fissility, but also on the excitation energy or in other words on the competition between the neutron evaporation process and fission. The excitation energy at the fusion barrier (*B)* is equal to the *(B - Q)* parameter and can be used as an additional parameter for empirical cross section systematics. A contour plot (Fig. 1.16) presents experimental cross section values in dependence of both, the fissility and the *(B - Q)* parameter for heavy nuclides (Z > 100) produced in complete fusion reactions. The calculated values of the *(B - Q)* parameter and fissility for some reactions leading to SHE are also shown as red symbols. It appears as if the "warm fusion" of heavy actinide targets with neutron-rich heavy ions is the most promising way towards heaviest elements.

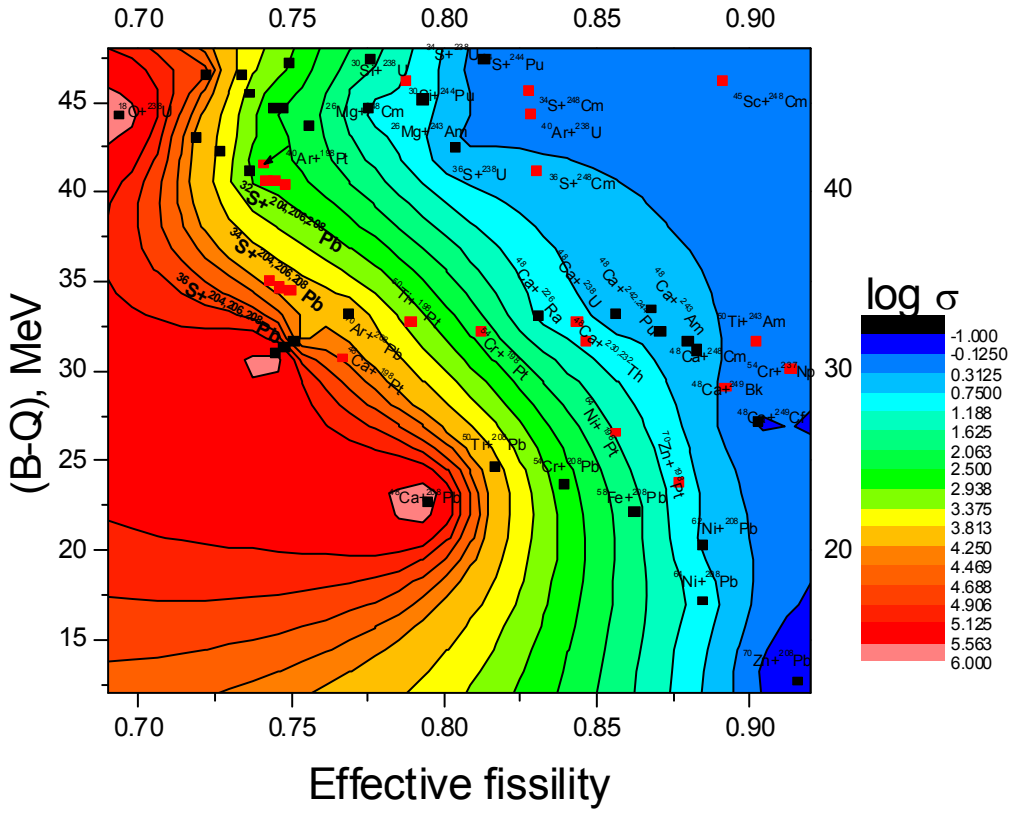

Fig. 1.16: Contour plot showing the correlation of the evaporation residue cross section from the fissility and the *(B - Q)* parameter. Adopted from [50].

1.6 Summary

SHEs exist solely because of enhanced nuclear stability, due to shell effects. Experimental studies have shown that cross sections for the synthesis of SHE decrease continuously, with exception of warm fusion reactions of doubly magic ^{48}Ca with actinide targets. Recent data from FLNR Dubna prove the importance of the choice of the nuclear reaction. More systematic studies are needed for a better understanding of the reaction mechanism of fusion reactions in the SHE region. The small cross sections, the short half-lives of the synthesized nuclides, the significant decrease of the luminosity of the experiments and the considerable increase of the background from byproducts called for a radical change of the approaches to the synthesis of new elements. Yet, the exploration of the "Island of Stability" will be a difficult task, since many technical developments have to be done first. Exploration of SHE nuclei is close to the border of present technical limitations.

It is certain that in order to unfold the mystery about the superheavy elements several conditions have to be fulfilled. Most of all there is a need for new principle experimental approaches which allow to reach directly the spherical shell at N = 184.

This is given by the impossibility of today's experimental set-ups to produce intense beams of neutron-rich projectiles, since there is no possible combination of available actinide targets and stable beams leading to a doubly magic SHE nucleus in the center of the closed shells. Such a task can nowadays be achieved mostly only by utilizing radioactive beams that already start to be used in nuclear physics experiments. However, for successful engagement into heavy element research their intensity needs to be increased by few orders of magnitude. Another task that lies in front of heavy element research is to improve the separation methods and detection systems, which can give an opportunity to get more closely to the "Island of Stability". The separation and detection techniques used in SHE research field are described in two following Sections.

Chapter II

Separation of superheavy elements

Short overview of methods for SHE separation

2.1 Introduction

The identification of the first transuranium elements has been performed by chemical means. In the early 1960s the first physical techniques were developed which allowed detecting nuclei with lifetimes of less than one second with high sensitivity. A further improvement of physical methods was achieved with the development of recoil separators and large area position sensitive detectors.

In order to study the properties of SHEs, they have to be produced in a nuclear fusion reaction and separated (1) from the primary beam and (2) from unwanted byproducts of the interaction of a beam with a target, such as transfer products, as well as from scattered beam and target material. This separation can be done in different ways using physical and/or chemical properties of the products. Physical methods are based on the capability of magnetic and electric fields to separate particles having different mass to charge ratios or velocities into different spatial trajectories. Chemical properties like the volatility in the gaseous phase and generally the distribution between two phases are utilized to make chemical separations (e.g. [59]). Depending on the reaction and on the reaction products, the available technique which offers the best separation and efficiency is chosen.

The following section gives a short explanation of gas phase chemistry where the separation of Hs isotopes presents an illustrative example. An extensive description of SHE chemistry can be found in [65]. In other parts of this chapter the principles and techniques of physical separation are described.

2.2 Chemical separation

Relativistic effects in the electron orbitals of SHEs have a pronounced influence on their chemical properties, thus the chemical investigation of SHEs is an important method to enlarge the knowledge about SHEs. In addition, chemical properties of SHEs may also serve as a basis for effective separation techniques, for the search for new

isotopes and new elements aiming at the investigation of both, chemical and physical properties of SHEs. This was for instance realized in the fast gas phase chemistry of Rf, Sg, Hs, element 112, and 114.

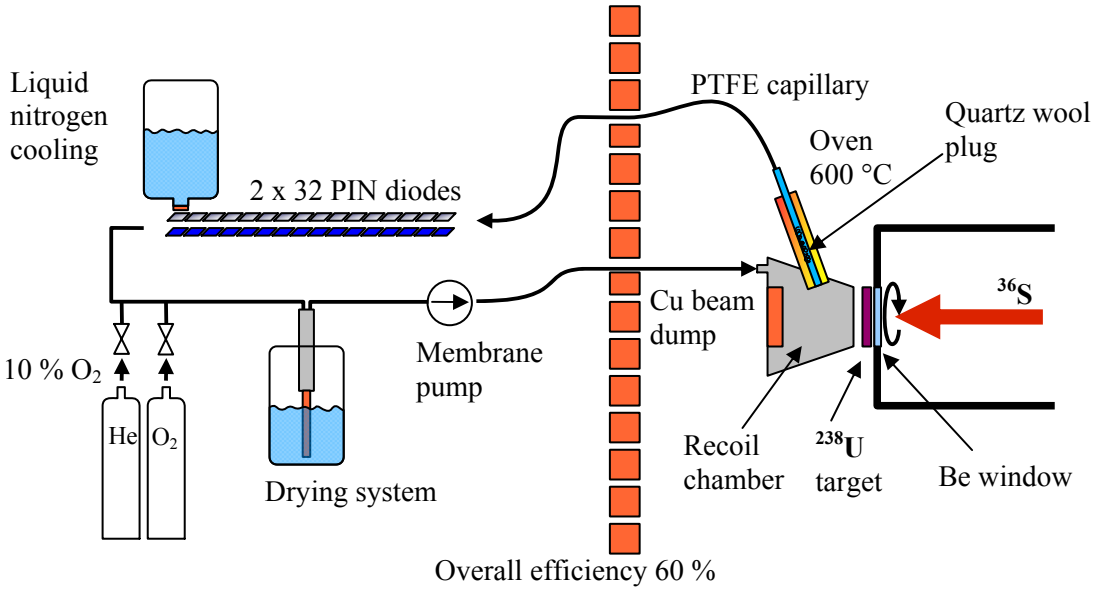

Fig. 2.1: Schematic view of the low-temperature thermochromatography experiment used to investigate HsO_4.

A setup (see Fig. 2.1), developed by the Munich group [47,48,50] used for example in experiments investigating properties of Hs isotopes is as follows: a target is placed at the end of the beam line of an accelerator. Behind this target, a so-called recoil chamber (RC) is mounted, which is flushed out with gas. The recoiled products are thermalized in the gas, and a chemical reaction takes place if the gas is reactive; or they attach to aerosols, carried by the gas flow. Volatile species are then transported to a detector setup by the gas flow. A window separates the volume of the RC at a pressure of 1 - 2 bars from the beam line, where high vacuum is required for beam transport. In gas phase experiments, a chemical separation of the SHE from unwanted byproducts is based on the different volatilities of the created molecules. Non-volatile products are trapped by the quartz wool plug filter and only very volatile species are transported to a detector through a Teflon capillary at room temperature.

The detector COMPACT (Cryo On-line Multidetector for Physics And Chemistry of Transactinides), used in Hs experiments, is a linear arrangement of 2 × 32 silicon PIN diodes, positioned in a way that a narrow (0.5 mm) channel is formed, in which the gas flows. A method known as thermochromatography is applied: by cooling

the downstream side of the detector with liquid nitrogen and keeping the other end at room temperature a temperature gradient is established. Depending on the volatility of the species carried in the gas stream they are adsorbed at different positions in the detector.

Since a coverage of the detectors by thin metal layers or SiO_2 layers is possible and does not influence the detector resolution, one can use different detector surface coverages for adsorption investigations. For very volatile metals like E112 and E114, it is important to distinguish adsorption due to chemical bonding and adsorption due to a weak interaction. The use of two types of detectors – noble metal coverage or with an inert surface (SiO_2 or Al_2O_3) – allows the measurement of both adsorption mechanism due to Van-der-Waals forces only and due to chemical bonding between E112/E114 atoms and the noble metal surface. The knowledge of both can improve extrapolations of properties like volatility and reactivity with transition metals over the group of the Periodic System of Elements.

From the chemical point of view investigations of E112 and E114 should concentrate on the elemental state, since the valence electrons, which are sensitive to the influence of relativistic effects, are not engaged in chemical bonds. From extrapolations, one could expect that E112 and E114 are fairly volatile in the elemental state.

However, a major problem in the chemical separation of elements is that elements, which behave chemically similar, can also be transported to the detector. Hence, a complete avoidance of background by chemical separations is impossible. During production of E112 and E114, comparably large activities of Rn isotopes were produced in transfer reactions and transported to the cryodetector by the gas flow, where alpha decays from Rn isotopes and their daughters negatively affect the search for SHE decay chains. The reduction of the background in such experiments is essential for the unambiguous identification of certain elements produced in nuclear fusion reactions with actinide based targets. The use of a gas-filled separator as a preseparator for chemistry can be important for chemical identification of volatile SHE in the elemental state. The preseparator will suppress unwanted byproducts utilizing the different magnetic rigidities of recoiling ions before a chemical separation is applied.

Further, without preseparation, it is difficult to perform chemistry experiments using aerosols as carriers of the activity. The main reason for this is that the beam

passing through the gas in a recoil chamber creates plasma, which destroys the aerosols and reduces the yield of transported products.

In section 4.3 one example of a chemical experiment with ^{261}Rf produced in the reaction ^{22}Ne + ^{244}Pu using a gas-filled preseparator will be presented in more detail.

2.3 Physical separation

An ion moving in an electric or magnetic field is forced onto a trajectory depending on their different masses *m*, charges *q,* and velocities *v*. The mass and velocity of projectiles is different compared to other reaction products, hence byproducts move on different trajectories and can be very effectively deflected by electric and magnetic fields. Usual suppression factors of the primary beam from reaction products are on the order of 10^{10} - 10^{12}. The separation time is determined by the recoil velocities and the length of the separator. They are typically in the range of 1 - 2 microseconds. Nowadays two types of recoil separator are used:

(1) Gas-filled separators use the different magnetic rigidities of recoils and projectiles traveling through a gas-filled volume at a low gas pressure (about 1 mbar) in a magnetic field of a dipole magnet [66]. As a gas filling, helium is commonly used in order to obtain a significant difference in the rigidities of slow reaction products and fast projectiles. An average charge state of the ions is achieved by frequent collisions of the ions with the gas atoms. Such type of separation devices are used in SHE studies, for example Berkeley Gas-filled Separator (BGS) in Berkeley, USA [67-70]; Dubna Gas-filled Recoil Separator (DGFRS) in Dubna, Russia [39]; Gas-filled Recoil Ion Separator (GARIS) in Tokyo, Japan [71] and the TransActinide Separator and Chemistry Apparatus (TASCA) in Darmstadt, Germany [72]. The last gas-filled separator, which has been recently installed at GSI will be described in more detail in section 2.4.

(2) Wien-filter or energy separators use the specific kinematic properties of the fusion products. The latter are created with velocities and energies different from the beam projectiles and other reaction products. Their ionic charge state is adjusted when they escape from a thin solid-state target into vacuum. Hence, only several charge states are guided through the velocity filter, the ionic-charge achromaticity is essential for high transmission. An example of such a separator used in experiments for the investigation of heavy elements is the Separator for Heavy Ion reaction Products (SHIP) at the GSI in Darmstadt [73] described in part 2.3.1.

Both types of separators have their advantages and disadvantages; in general, gas-filled separators are used for more asymmetric reactions, while vacuum separators are more suitable for symmetric reactions. The reason for this lies in the higher acceptance of gas-filled separators for EVRs with wide angular, charge, and velocity distributions. However, vacuum separators show better capabilities of background reduction.

2.3.1 Physical aspects of kinematic separators

An example of a kinematic separator, which uses a combination of electric and magnetic fields to separate particles with different velocities, is the velocity filter SHIP [73], at which the discoveries of elements 107 to 112 have been performed. It is constructed as a two stage velocity filter with spatially separated electric and magnetic fields. At the tail an additional 7.5° deflection magnet is placed behind the second quadrupole triplet providing supplementary reduction of high energy background by a factor of 10 – 50. A schematic drawing of SHIP can be seen in Fig. 2.2.

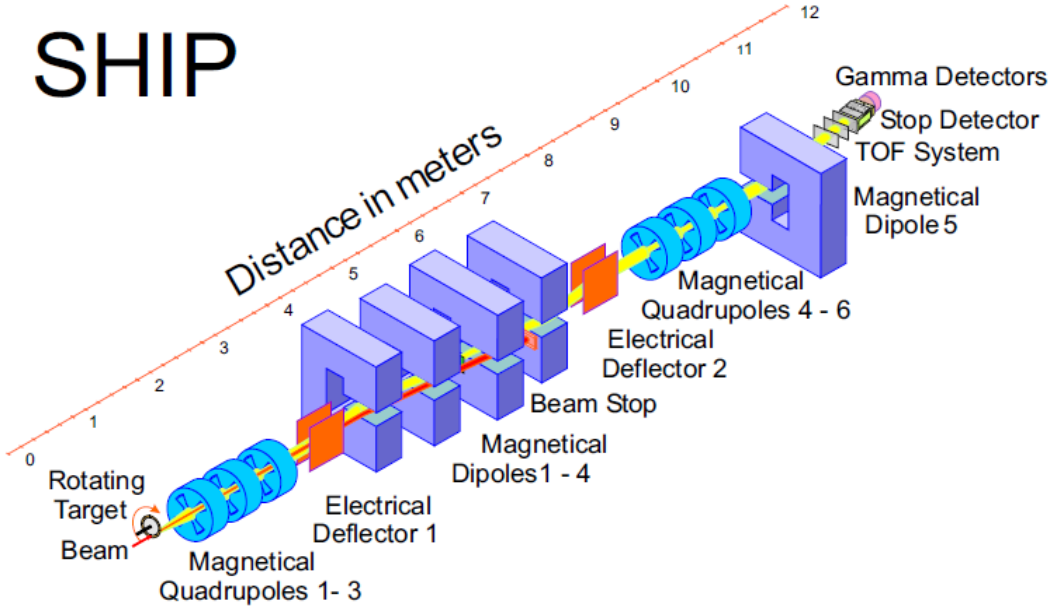

Fig. 2.2: Schematic drawing of SHIP separator with the couplet at the end of it detection system.

The combination of two electric and four magnetic dipole fields, together with two quadrupole triplets, is used for focusing all ionic charges within an ionic charge window of 20%. Maximum velocity dispersion is necessary to separate projectiles and EVRs in the medium plane of the system. Here, the beam is stopped in a Faraday cup.

The velocity dispersion is then compensated in the second half of the filter, which is ion-optically antisymmetric to the first half.

The whole separator has a length about 12 m. Depending on the type of reaction the efficiency of the separator can reach up to 60% for more symmetric reactions, but decreases dramatically for asymmetric reactions. In a recent experiment aiming at the identification of element 112 in the reaction $^{238}U(^{48}Ca, xn)^{286-x}112$ the maximum efficiency of SHIP was calculated to be 34% [60].

In the region of hot fusion reactions between actinide targets and lighter projectiles, gas-filled separators are more efficient (TASCA efficiency is ~ 60% for Ca induced reactions for SHE formation). Gas-filled separators will be described more closely in the following sections. Already several such separators exist around the world, each having its own special properties and design.

2.3.2 Physical aspects of gas-filled separators

The basic physical principles of gas-filled separators were already formed in the 1950's (e.g. [74,75]). Investigations of the charge state of fission fragments traversing through a gas-filled media showed that an average charge state of the products is reached at relatively high gas pressures. When an EVR is produced in a compound nucleus reaction, it recoils out of the target in different charge states. Because an average charge state can be obtained relatively fast in collisions with the filling gas, all original charge states can be guided through the separator. This property increases significantly the efficiency of the recoil separator. The main interaction processes of particles in the gas are: charge exchange collisions and multiple scattering. When an EVR recoils out of the target and encounters gas atoms, after a large enough number of collisions, the fluctuation of the charge state reaches equilibrium between the capture and loss of electrons and an average charge value $q_0 \pm \Delta q$ for a given velocity of the ions is maintained. A simplified illustration of the dependence of ion deflection in a dipole magnet with gas filling and in vacuum is shown in Fig. 2.3.

Gas-filled separators are especially suitable for studying reaction products resulting from asymmetric hot fusion reactions. The reason for this is in their ability to efficiently accept, separate, transfer, and focus in the focal plane even very slow ions emitted from a target in front of the recoil separator. Slow recoils have a particularly wide charge, velocity, and angular distribution when leaving the target.

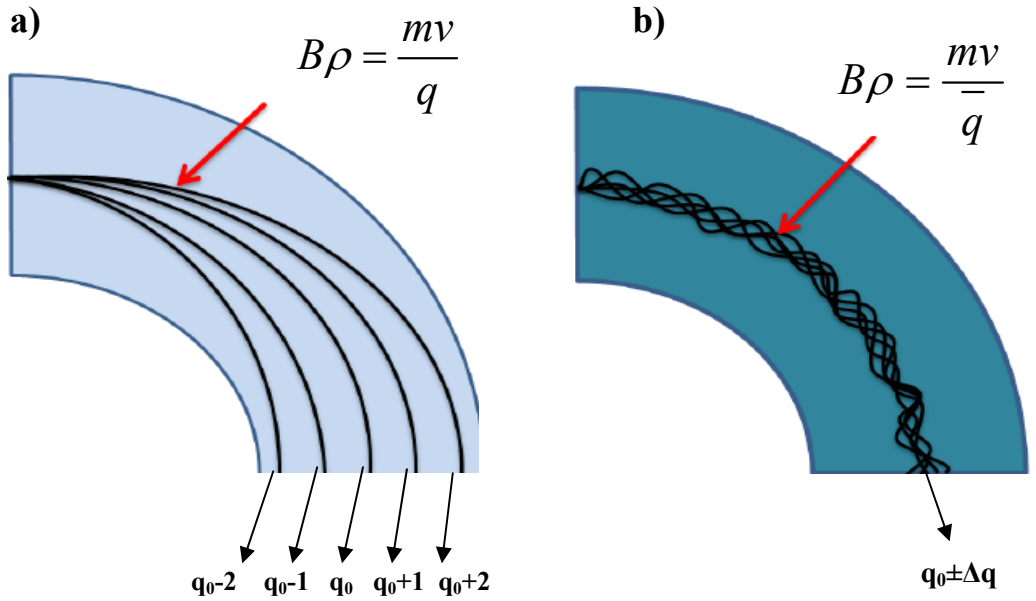

Fig. 2.3: Magnetic rigidities of heavy ions a) in vacuum and b) in He gas. In the gas-filled magnetic field region, the discrete trajectories corresponding to the different charge states collapse around a trajectory defined by the average charge state of the ion in the gas.

The lack of strong electric fields in the separator enables a large opening at the entrance of the separator, which means a high acceptance for a wide angular distribution of products. The filling gas inside the separator is responsible for charge and velocity focusing of the recoils, which leads to a high acceptance in those properties. Thus, the transmission of gas-filled separators for slow evaporation residues, i.e. in asymmetric nuclear fusion reactions, is higher than for electromagnetic vacuum separators.

Deflection of ions moving through a magnetic field is governed by the magnetic rigidity $B\rho$. Before the strength of the magnetic field is selected, it is necessary to know the magnetic rigidity of the EVRs. For a trajectory perpendicular to the magnetic field the magnetic rigidity of EVR's is determined by the formula:

$$B\rho = \frac{mv}{\bar{q}} \tag{2.1}$$

Here, B is the magnetic field strength, ρ is the radius of curvature of the particle, m, v, and q are mass, velocity, and its average charge respectively. The velocity can easily be determined by using kinematics. The mass can be obtained from various mass tables. The difficulty is in estimating of the average charge state, $\bar{q}$. Bohr was the first one who made a major contribution to the problem of average charge states.

Following a theory of Bohr [76], the ions are stripped of all electrons which have an orbital velocity smaller than the translational velocity v of the ion itself, an expression, for the average charge state of ions can be derived using the Thomas-Fermi-Model of the atom. For the velocity range $1 < \frac{v}{v_0} < Z^{\frac{2}{3}}$, where v_0 is the Bohr velocity ($2.1877 \cdot 10^6$ m/s) and Z describes the nuclear charge of the ion, the average charge state is:

$$\bar{q} = \frac{v}{v_0} \cdot Z^{\frac{1}{3}} \tag{2.2}$$

Combined with equation 2.1 and plugging in the numbers for the constants the following expression for the magnetic rigidity is found:

$$B\rho = 0.02267 \frac{A}{Z^{\frac{1}{3}}} \qquad [\mathrm{T \cdot m}] \tag{2.3}$$

This equation reveals one of the big advantages of gas-filled separators. The right side of equitation 2.3 is free of values for the initial velocity and charge state of the ions, which means that reaction products of the same kind have equal magnetic rigidities regardless of their initial charge and velocity distribution and can therefore all be transmitted to the focal plane of the separator. In comparison to vacuum separators this yields higher transmission values of reaction products, which is especially important in SHE research, where the EVR production rate is very low.

A study of the magnetic rigidities of heavy ions in helium gas was conducted by Ghiorso *et al*. [77]. The results of the study follow the same general trend of $\bar{q} \propto v \cdot Z^{\frac{1}{3}}$, but some periodic deviations from this proportionality were found. In Fig. 2.4 experimental values of $B\rho/A$ are shown reflecting the dependence on $\bar{q}$ for constant ion velocities v, with deviations from the general trend.

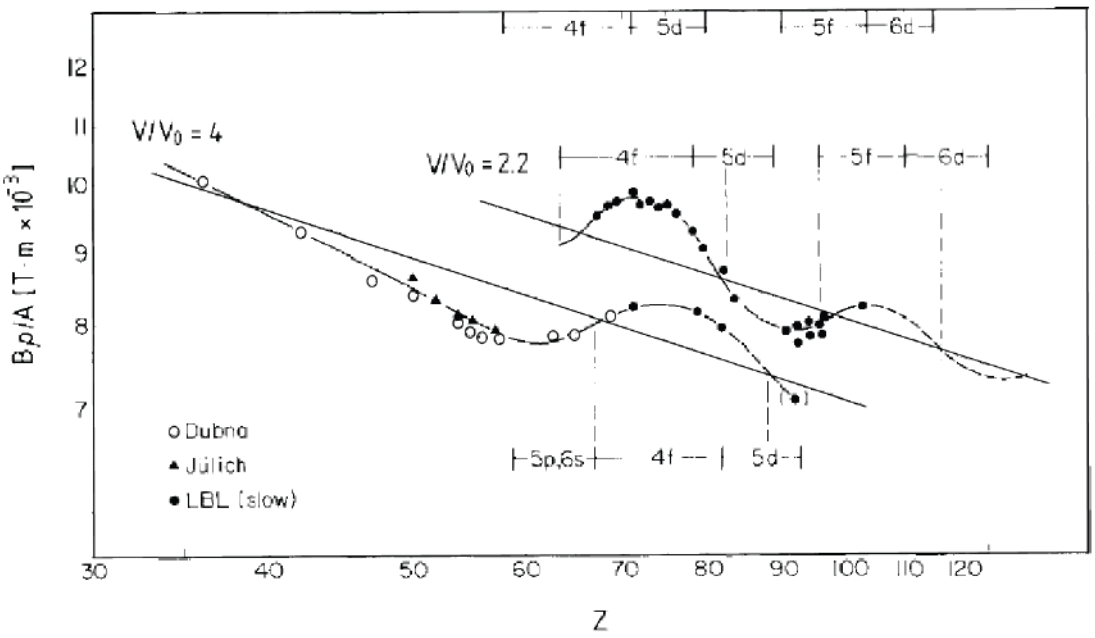

Fig. 2.4: Experimental values for Bρ/A as a function of atomic number Z of the ions. The straight lines are the fits to the data that show the ~ $Z^{1/3}$ dependence. The curved lines show deviations from the trend. The atomic shell configurations of the ions as a function of the number of the remaining electrons are shown, the configuration at the top of the graph applies to the neutral atom. Adapted from [77].

The graph hints towards a close relation of the periodic deviation to the indicated atomic shell structures of the ions. Opposed to the prediction in eq. 2.3 there is a velocity dependence of $B\rho$, which, however, varies for different regions of Z. The magnetic rigidities of heavy ions in helium gas were also studied by Gregorich *et al.* [78], in the $99 \leq Z \leq 111$ atomic number range. Based on these observations a semi-empirical formula for the average charge states of a heavy ion in He gas was obtained. A sinusoidal correction was applied to the data that takes into account the shell structure of the stripped ions:

$$\bar{q} = mx + b + d\sin\{\frac{2\pi}{32}[Z - (mx+b) - f]\} \tag{2.4}$$

Here $x = \frac{v}{v_0}Z^{\frac{1}{3}}$ for $Z \geq 4$ and the best fit is obtained with $m = 0.641$, $b = -0.235$, $d = 0.517$, $f = 74.647$. The first part of the equation shows a linear trend with a relatively small intercept as in equation 2.2. The sinusoidal correction is based on an estimate of the number of electrons that the heavy ion retains, $Z - mx + b$. The amplitude of the sinusoidal correction is d, and it is approximately one half of a charge unit and has a period of 32 that corresponds to the length of the sixth and seventh rows of the periodic

table. The phase parameter *f* shows an ascending node that is approximately half-way through the *5d* electron shell.

Formula 2.4 provides a good fit for fast ions with velocities $v/v_0 \geq 1.6$ in He. Ions traveling at lower velocities show a certain deviation from this behavior, which is thought to originate from the high ionization potential of He. Sytematic studies investigating slow evaporation residues are under way at Lawrence Berkeley National Laboratory (LBNL) [78]. Future SHE experiments with TASCA will foremost deal with slow products from asymmetric reactions, where a correction to eq. 2.4 is needed.

The average charge $\overline{q}$ of ions traversing a gas-filled separator is also sensitive to the used gas type and pressure. During a number of experiments, such gases, as argon, hydrogen, and nitrogen have been studied [79]. However, the most useful gas is He with a pressure of 0.5 ÷ 2 mbar, because $\overline{q}$ has high values for low ion velocities in He compared to other gases, and the $\overline{q}$ value is almost constant over a wide velocity range. A constant value for $\overline{q}$ in He is at the same time a disadvantage: transfer reaction products with similar charge state can be also transmitted to the focal plane. To obtain a better suppression from transfer products, H_2 as filling gas can be used (see Fig. 2.5). As can be concluded from eq. 2.1, the higher the average charge of the ions is, the lower is the magnetic rigidity. One of the possible reasons for the high average charge of slow ions in He gas can be the high ionization potential of the He atom. The EVRs flight out from the target has a specific charge distribution due to the loss of electrons in the target material. The fewer the number of electrons, which are captured passing through the gas, the higher the equilibrium charge state will be. The probability for an EVR to capture an electron from a gas atom is maximized by two issues: first, the mean orbital velocity of the electron in its initial state v_i should be approximately equal to the relative velocity v_{rel} of the EVR in respect to the gas atom. Second, the final orbital velocity v_f of the electron, that was captured, should match v_{rel}.

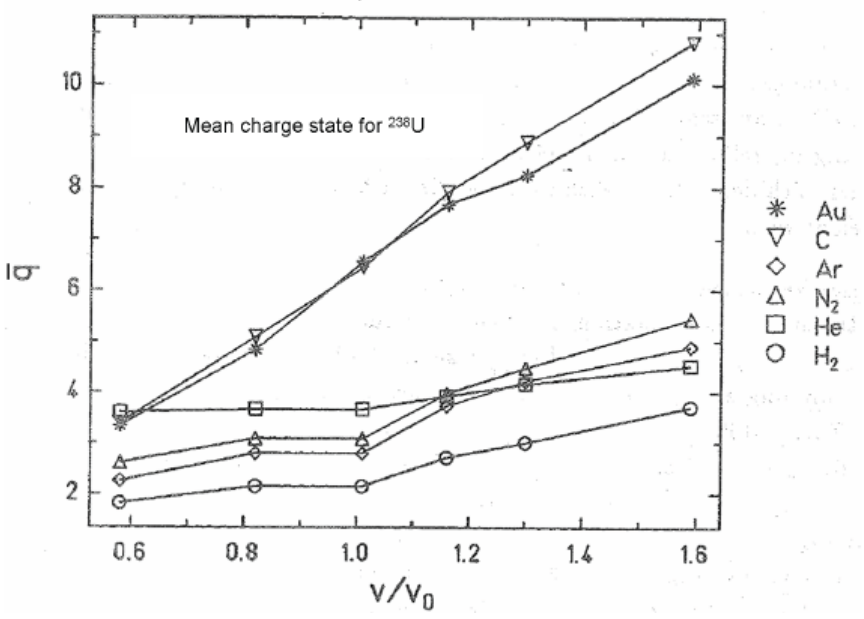

Fig. 2.5: Average charge state $\bar{q}$ of ^{238}U in different gases (Ar, He, H_2 , N_2) and solid media (C, Au). Taken from [79].

Because the orbital velocity of electrons in He is quite high (1.4 v_0) due to their high binding energy of ~ 25 eV (for example, H_2, N_2, and Ar have binding energies ~ 15 eV), slow products from asymmetric reactions with a typical velocity of v_{EVR}= v_0 have a small chance to capture electrons. Thus, the main advantage of He is the suppression of low charge fractions of EVRs leading to lower average magnetic field strengths, and hence, to a better resolution $\Delta B\rho/B\rho$. Furthermore, because of their low mass, He and H_2 cause less multiple scattering of the ions than a gas such as N_2. Multiple elastic scattering makes the resolution of a separator worse and is therefore unfavorable. H_2 is the most convenient filling gas, because of a better separation of EVRs from transfer products, but many laboratories avoided its use mainly because of safety reasons. N_2 is useful only for energetic ions, because of the higher stopping power of the larger molecules, and therefore, a better resolution due to increased probability of charge exchange interactions. For studies of reactions with inverse kinematics usually argon is chosen as a filling gas.

2.3.3 Main design principles of a gas-filled separator

The magnet setup is the main body of the separator. A configuration of magnets has to be chosen, to obtain a transmission as high as possible at a background as low as possible. The main idea is that a dispersive component (a dipole magnet) should be placed close to the target in order to avoid long drift distances and to have a large acceptance, and therefore, a better transmission and focusing of the products. Long drift distances in the gas-filled separator enlarge the image size due to multiple scattering. The bending angle of the dipole magnet is an important issue. A small angle of around 30˚ is favorable to keep the dispersion ($cm/\%B\rho$) in the focal plane low.

A higher dispersion would widen the spot size and cause losses of products when the $B\rho$ value is not well known. Nevertheless, the bending angle of the dipole magnet should be large enough to reduce the background.

Quadrupole magnets are installed for focusing of the products passing through the dipole into a focal plane. Usually two quadrupole magnets are used – one, for horizontal focusing, the other one – for vertical.

Many aspects have to be considered when designing a new gas-filled separator. In this chapter the main design parameters will be discussed. Extensive calculations and studies of the magnetic fields inside the magnets are usually undertaken in advance to estimate the behavior of the ion trajectories.

A compact magnet setup and a shorter length result in a shorter transport time through the separator and higher transmission. To reduce background even more, an additional dipole magnet can be placed behind the quadrupole magnets, but that makes the setup longer and decreases the transmission.

A crucial factor is the design of the gas-filled chambers inside the dipole and quadrupole magnets. The chambers should be as wide as possible to provide a high acceptance and transmittance of the products.

The material as well as the design of the beam stop installed inside the dipole chamber also have a strong influence on the performance of the separator. Beam particles hitting the beam stop at high velocities may sputter off material and can be scattered. It is important to prevent or to minimize this. Further, nuclear reactions may occur from the interaction of the beam with the beam stop material if the Coulomb barrier is overcome. The resulting compound nuclei or evaporated particles (n, p, α) can

reach the detector and generate background events. Often Ta is used as a beam stop material because it has a high Z leading to a high Coulomb barrier.

Some gas-filled separators used in SHE research with respect to the properties mentioned above are presented in Table 2.1.

Table 2.1. Comparison of some gas-filled separators, h – horizontal focusing and v – vertical focusing magnetic element

Separator	DGFRS	GARIS	RITU	BGS	NASE	TASCA	
						HTM	SIM
Configuration	DQ_hQ_v	DQ_hQ_vD	$Q_vDQ_hQ_v$	Q_vD_hD	DQ_hQ_v	DQ_hQ_v	DQ_vQ_h
Solid ang., msr	10	12.2	10	45	10	13.3	4.3
Bend. angle, deg	23	45+10	25	70	30	30	30
$B_{\rho max}$,Tm	3.1	2.16	2.2	2.5	2.2	2.4	2.4
Length, m	4.03	5.76	4.7	4.7	3.85	3.5	3.5
Dispers.ion, cm/%	0.63	0.97	1.0	2.0	0.61	0.9	0.1
Transmission*, %	41	~40	~40	49-59		60	36

*Transmission measured or calculated for the reactions $^{238}U/^{244}Pu(^{48}Ca,xn)E112/E114$.

2.4 The gas-filled recoil separator TASCA

In superheavy element research one of the main challenges is the theoretical understanding of nuclear structure and nuclear reaction mechanisms. Another one, not less difficult, is the synthesis and identification of the heaviest elements. The utilization of recoiling products has provided ways for the investigation of the heaviest elements since the discovery of mendelevium in 1955 [80]. Because of the success of this method for the search for new elements a number of separators has been built. Nowadays, SHE research requires the development of new improved experimental techniques. The TransActinide Separator and Chemistry Apparatus (TASCA), is a newly constructed gas-filled separator at the Gesellschaft für Schwerionenforschung (GSI) in Darmstadt, Germany, devoted to the studies of the physical and chemical properties of superheavy elements. This project is being supported by a broad international collaboration. A schematic picture of TASCA is shown in Fig. 2.6.

The main goals of the TASCA design were to obtain a maximized transmission and effective separation of elements with $Z > 103$ synthesized in hot fusion reactions.

Thus, TASCA is focused on the separation and investigation of neutron-rich transactinide nuclides produced in reactions of highly intense ion beams with actinide targets. Further, the setup is intended to act as a preseparator for chemical investigations of SHE which have proved to be very effective and promising [81]. The installation of the TASCA separator into the newly constructed cave X8 at the UNILAC (UNIversal Linear ACcelerator) experimental hall ended in 2005. To keep the costs low, it was decided to use existing magnets from the old NAch SEparator, NASE (later named HECK) at the GSI. In the following sections, a motivation for the new gas-filled separator TASCA will be given and the special features of the new setup will be described.

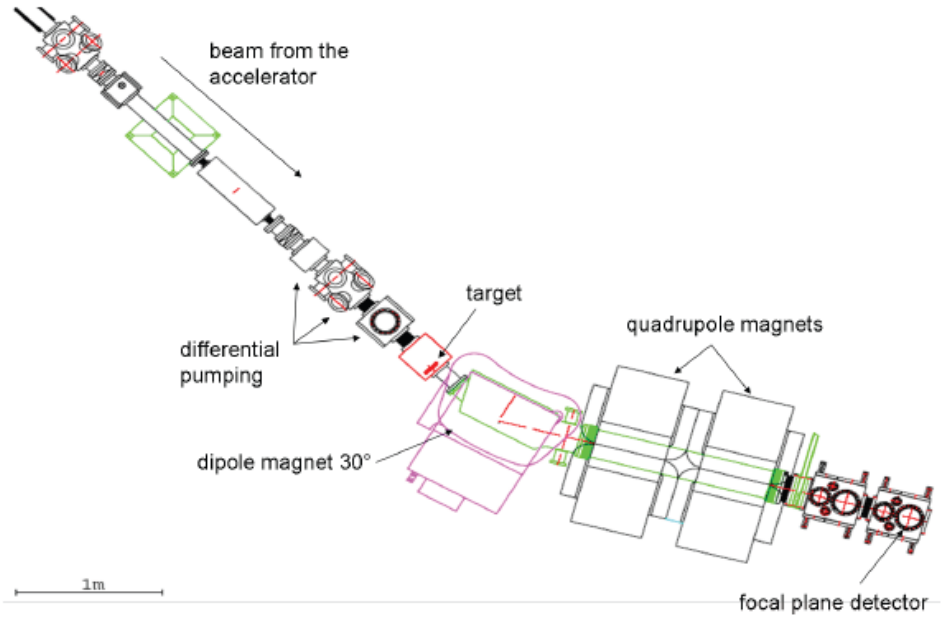

Fig. 2.6: Schematic drawing of TASCA.

2.4.1 Motivation for TASCA

One of the main motivations to build TASCA was the requirement to significantly reduce the background especially from transfer reaction products like Po, Rn, and At in future SHE chemistry experiments. Physical preseparation constitutes a useful method for this purpose.

Envisioned advantages are the absence of the primary beam, which strongly reduces the jet-transport efficiency in "traditional" SHE chemistry experiments [81] and the very often crucial reduction of transfer products. In addition, such a combination will allow for the investigation of new chemical systems that were not accessible before [82] and will

avoid all the problems associated with the interaction of the intense primary beam with the thin entrance window foils, which have to stand a pressure difference of about 1 bar. However, to introduce slow recoils formed in asymmetric nuclear reactions into the chemistry, a new challenge arises from the need of large and very thin entrance window foils between the rear end of the separator and the Recoil Transfer Chamber (RTC) [82-84]. In chemistry experiments the RTC is used instead of a Focal Plane Detector (FPD) and serves as an interface to chemistry setups.

The most central research goals for TASCA are the synthesis of new elements, chemical investigations of elements 104 to about 116, nuclear reaction– and nuclear structure studies of the most neutron-rich nuclides of these elements.

2.4.2 Special features of TASCA

This section is devoted to those aspects of TASCA, which make it unique amongst gas-filled separators involved in superheavy element research and thus very promising to obtain new results in this field.

2.4.2.1 Differential pumping

A differential pumping system for the separation of the gas-filled volume in the separator (typically 1 - 2 mbar) from the vacuum in the beam line of the accelerator (around 10^{-7} mbar) has already been realized in the gas-filled separators GARIS (Gas-filled Recoil Isotope Separator) at the RIKEN laboratory in Japan and RITU (Recoil Ion Transport Unit) in Jyväskylä, Finland. In TASCA, differential pumping consists of three stages on a length of approximately 1 m. Each section involves 2 pumps, with which a pressure reduction roughly by a factor of 10^{-2} is achieved [85]. A schematic drawing of the differential pumping setup at TASCA is shown in Fig. 2.7.

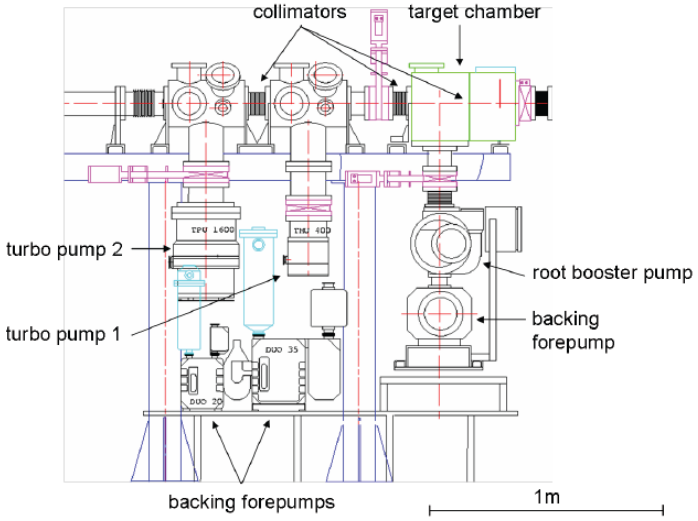

Fig. 2.7: Technical drawing of the differential pumping system of TASCA. The gas collimators have the following diameters: C_1 = 10 mm, C_2 = 13 mm, C_3 = 18 mm (from right to left).

The main advantage of this system is the windowless operation of the separator, i.e. no window between the accelerator and the separator is needed. Earlier, the beam intensity was limited by the stability of such a window. Now, it can be increased and is limited only by the stability of the target backing. In addition, complications connected to the possible breaking of the window are avoided.

2.4.2.2 Target wheel

The target wheel ARTESIA (A Rotating Target wheel for Experiments with Superheavy element Isotopes at GSI using Actinides as target material), developed for chemistry experiments, can also be used in TASCA. The target wheel is divided into three sections, each having an area of 1.9 cm^2. In experiments the rotation of ARTESIA with typically 2000 rpm is synchronized with the pulsed particle beam from the accelerator in such a way that every third beam pulse irradiates the same target segment. The with 50 Hz pulsed beam has a duty cycle of 25%, thus, a beam pulse lasts 5 ms with 15 ms pause between pulses. This way the target foil can cool down between subsequent pulses. In comparison to a stationary target a larger area of target material can be irradiated, which offers the advantage of reducing the deposited energy in the target per area unit. In addition, a wobbling of the beam is applied, which allows a spread of the beam spot over a surface of approximately 0.5 cm^2. All these factors together result in the possibility of using more intense beams and/or a longer life time of

the target and backing foils. Fig. 2.8 shows the target wheel prepared with uranium targets with different backing materials for a target tests. The burned spots on the target foils on the right picture demonstrate the area of irradiation.

The synchronization of the target rotation with the pulsed beam is based on a photodiode signal passing the target edge. To prevent damage from the neutron field when placed close to the target wheel, the diode is situated in a remote place and receives the light signal through a glass fiber cable.

Fig. 2.8: Pictures of the front side of ARTESIA mounted with ^{238}U target material. Backing/target material/fronting: left: C/U/C, top: Ti/U/-, bottom: Ti/U/C. The left picture was taken before, the right one after irradiation.

2.4.2.3 Two ion-optical modes

In the design phase of TASCA ion-optical and magnetic field calculations using the TRANSPORT code [86,87] have been performed for different possible magnet arrangements, such as DQQ, QDQ and QDQQ (here, D denotes a dipole and Q a quadrupole magnet) [71]. The results of these calculations are summarized in Fig. 2.9.

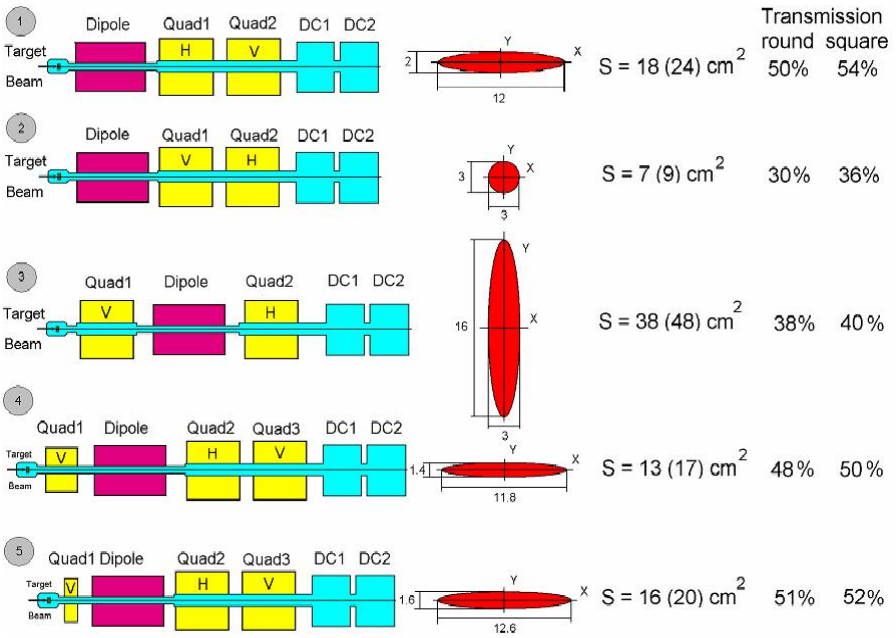

Fig. 2.9: Ion-optical calculations of different configurations of TASCA (*h* denotes horizontally focusing quadrupole magnets, *v* vertically focusing quadrupole magnets).

From the five calculated configurations shown in Fig. 2.9, two have been selected with the shortest separator length: DQ_hQ_v as the High Transmission Mode (HTM), which has the highest transmission, and DQ_vQ_h as the Small Image Mode (SIM) (see Fig. 2.10). They result from the possibility of changing the polarity of the two quadrupole magnets (Q_1 and Q_2) of the separator. The HTM is achieved by focusing the products horizontally with the first quadrupole magnet and thereafter vertically with the second quadrupole magnet. The SIM uses the opposite polarity settings of the quadrupole magnets.

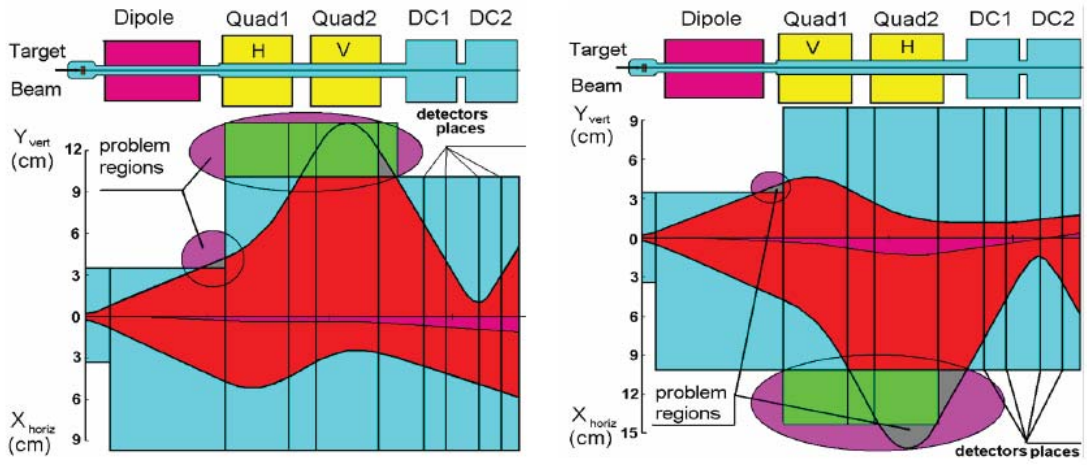

Fig. 2.10: The two final ion-optic TASCA configurations: (a) SIM and (b) HTM. Adapted from [88].

In Fig. 2.10 a) the results of ion optical calculations [88] of the classical DQ_hQ_v configuration of the existing NASE gas-filled separator structure with first horizontal and second vertical focusing quadrupoles are shown. The vertical beam shape shows, that products are cut off at the exit of the dipole magnet vacuum chamber. Another problem region is the vacuum chamber of the second quadruple and the valve between the quadrupole chamber and the detector chamber. It is not possible to increase the field in the exit quadrupole in order to focus the beam closer to the quadrupoles because of the existing power supply and the current limitations of the magnet. The areas where reaction products are lost are highlighted as “problem regions”. A possible solution of the problem is by using a vacuum chamber with large apertures in all the magnets, the dipole and the quadrupoles. By increasing the total length of the quadrupole duct and using a large flange between dipole and quadrupole ducts already improves the situation by a lot. This measure should increase the total transmission up to 30 - 50%. The momentum dispersion in this case is quite large 0.8 cm/%. The product beam size image is acceptable (~ 7 x 2 cm^2).

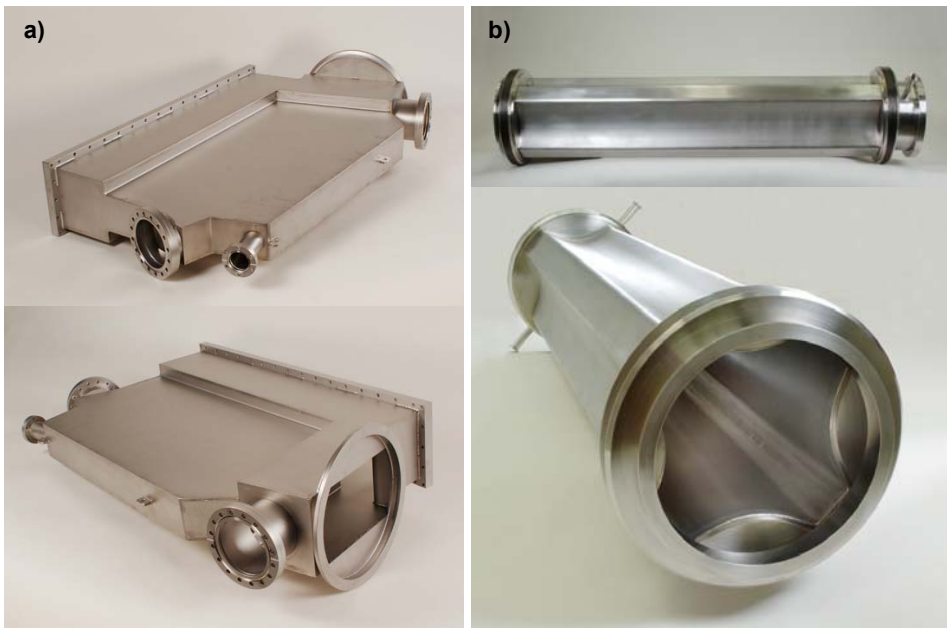

Fig. 2.11: New vacuum chambers for TASCA: (a) dipole chamber and (b) quadrupole chamber.

In Fig. 2.10 b) the inverted focusing (DQ_vQ_h configuration) is presented, for the existing NASE vacuum chamber. The calculations show, that the transmission of the recoiling products is cut off due to the large momentum dispersion in between the quadrupoles and inside the second quadrupole magnet. In addition, the products are cut off at the exit of the dipole magnet vacuum chamber in the vertical plane. The transmission is much lower in this case. Using a square vacuum duct inside the quadrupole magnets already improves the situation significantly. The big advantage of the DQ_vQ_h configuration is the very small image size at the exit focus (4 x 3 cm^2) due to the small (close to 0) momentum dispersion which is very useful in chemistry experiments with short lived isotopes.

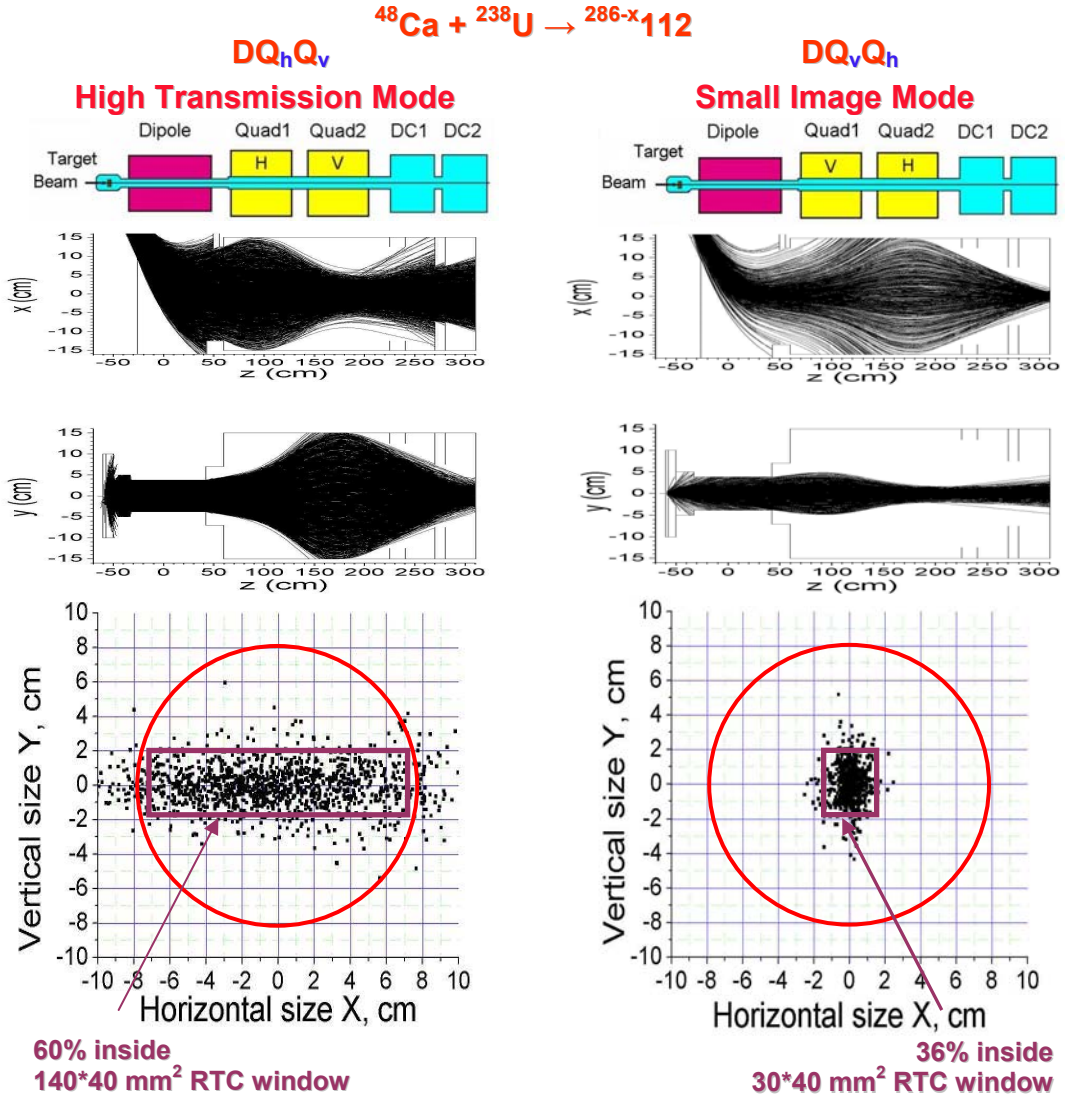

Fig. 2.12: The two final ion-optic TASCA configurations: (a) SIM and (b) HTM.

According to ion-optical calculations, the transmission can be improved significantly by building new vacuum chambers for the dipole magnet and the quadrupole magnets with the highest possible volumes. The new vacuum chambers, which were built based on this consideration, are shown in Fig. 2.11.

Monte Carlo simulations [89,90] have been performed for instance for the reaction $^{238}U(^{48}Ca, xn)^{286-x}112$ resulting in a transmission of products through the separator in the HTM of 60%, with an image size in the focal plane of approximately 56 cm^2 (see Fig. 2.12). The spot size in the focal plane in the SIM has been computed to be only 12 cm^2, at the expense of a decreased transmission of 36% [91,92].

While almost half of the products are lost in the separator with respect to the HTM, the SIM is expected to outweigh the HTM in efficiency when investigating short lived (i.e. half lives of $T_{1/2} \approx 1$ s) isotopes by chemical means. A faster flushing of the smaller SIM RTC chamber and, therefore, a faster transport of the activity to the detector is expected to compensate for the loss of products in the separator. A photograph of TASCA is shown in Fig. 2.13.

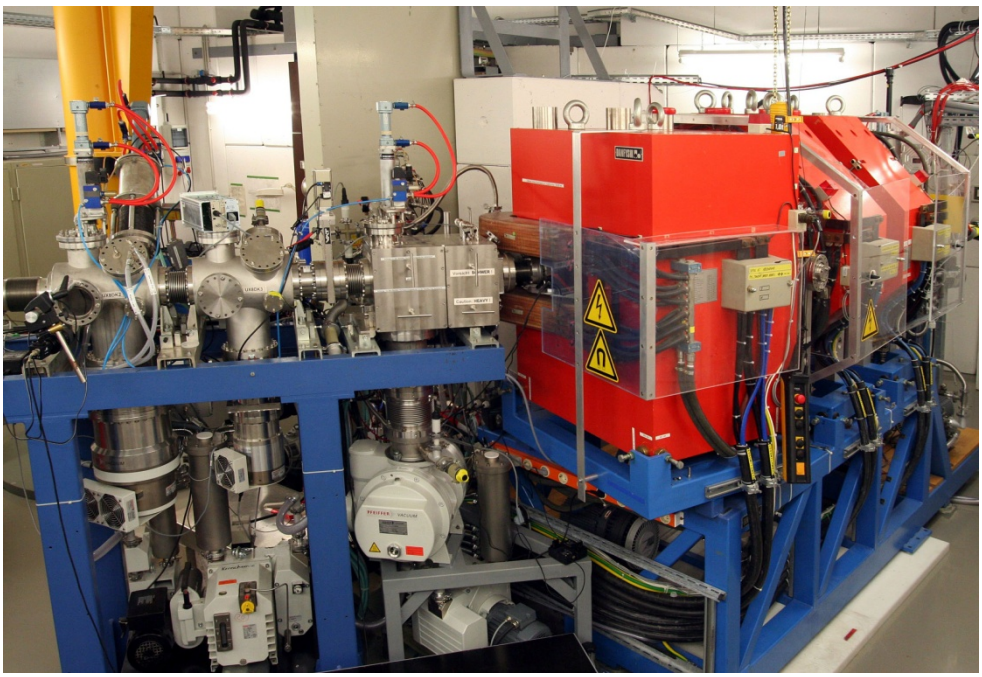

Fig. 2.13: TransActinide Separator and Chemistry Apparatus (TASCA)

2.4.2.4 The chemical interface

One of the major tasks of TASCA is to provide the possibility of both physical and chemical separation of superheavy isotopes. TASCA gives the possibility to place a position-sensitive detector in the focal plane and study the decay properties of implanted radioactive nuclei, or to place the RTC in the focal plane and to transport the fusion products to different counting setups and chemistry apparatuses.

The RTC is, in principle, a chamber attached to the exit of the separator, where products are thermalized in a gas and made ready to be flushed out and transported to a chemical setup. The RTC in the TASCA setup fulfills the same tasks as the RC in a chemical experiment, described in Section 2.2. The gas pressure inside the RTC is kept at 1-2 bar, which means that an entrance window is needed to separate the RTC and the separator volumes (~ 1mbar).

Because asymmetric reactions will predominantly be used in TASCA, the recoil energy of the EVRs from the nuclear fusion reactions in the target is small (low momentum transfer because of light projectiles and heavy targets). This calls for thin windows, which must withstand a pressure difference corresponding to 100 kg for the HTM RTC. Table 2.2 illustrates the correlation between the required thickness of the Mylar window foils and the asymmetry of the selected reaction.

Table 2.2: The range of EVRs in Mylar depending on the recoil energy from nuclear fusion reactions.

Reaction	Recoil energy [MeV]	Range in Mylar [μm]
$^{208}Pb(^{50}Ti,1n)^{257}Rf$	45.5	6.0
$^{244}Pu(^{30}Si,5n)^{269}Hs$	18.1	2.9
$^{244}Pu(^{26}Mg,5n)^{265}Sg$	13.5	2.4
$^{244}Pu(^{22}Ne,5n)^{261}Rf$	9.5	1.7

In order to prevent the breaking of a window foil, a supporting honeycomb structure is used. The grid should be constructed as thin as possible to minimize losses due to non parallel trajectories of products, while still being sufficiently stable in order to hold the weight of the pressure difference. The laser cut supporting grid of 1mm thick stainless steel, with 0.3 mm wide spokes and holes of 2.9 mm in diameter, features a geometrical transmission of 80%.

For each of the two ion-optical modes of the separator an appropriate RTC has been built and tested to make use of the different spot sizes in the focal plane [93]. Pictures of both RTCs are displayed in Fig. 2.14 and 2.15.

Fig. 2.14: Left: The HTM RTC viewed from the side which is attached to the separator. The supporting honeycomb structure 140×40 mm2 can be seen. Right: HTM RTC from the other side, the many gas valves for an adjustable gas flow are visible.

Fig. 2.15: Left: The SIM RTC with an entrance window of 30×40 mm2. Right: Side view of the SIM RTC. Spacers can modularly be introduced to the setup to change the depth of the RTC.

Chapter III

Identification of superheavy elements

Identification of SHE

Recoil separators are designed to filter out products which are produced in fusion reactions from byproducts with highest possible efficiency. Since higher overall yields result in increased background levels, the positive identification of the reaction products is accomplished by detector systems. The detector type to be selected depends on the particle rate, energy, decay mode, and half-life.

3.1 Physical aspects of detection systems

Experimental as well as theoretical data on the stability of heavy nuclei show that they decay by α emission, electron capture, or fission, with half-lives ranging from microseconds to days. Therefore, silicon semiconductor detectors are well suited for the identification of nuclei and for the measurement of their decay properties. If the total rate of ions striking the focal plane of the separator is low, then the particles can be implanted directly into a silicon detector. Using position-sensitive detectors, one can measure the spatial distribution of the implanted particles. This is important for search of correlated decay chains and for optimization and control of the ion optical properties of the separator.

The implantation detector can be accompanied by other strip detectors at its sides, forming a box, to increase the detection efficiency by trapping escaping α-particles. The identification of an isotope is performed by observing the characteristic α decay chains. In a decay chain, all subsequent decay processes take place at the same position, where an evaporation residue was implanted, because decay products have a very small recoil range. Hereby, the correlation of the decay chain members has to be consistent in position, time, and energy deposition in the detector. Once a decay chain is observed, the decay properties, the α- or SF- half-life of the nucleus, and E_α of the chain members can be derived.

3.1.1 Recoil-Decay Tagging Technique

For the heavier proton rich nuclei exceeding Z = 70 and A = 150 α-emission is becoming the predominant decay mode, hence α-spectroscopy is a useful identification method. A combination of an efficient separator with an appropriate detection system gives a powerful tool for investigating new isotopes and elements.

3.1.1.1 α − α correlation method

So far the only method that has proved itself usable in search for neutron deficient isotopes[1] and in investigation of their spectroscopic properties is the one of delayed α−α coincidences. This method is based on analysis of a generic decay chain starting with the implantation of an EVR into a silicon position sensitive detector followed by a subsequent series of alpha decays according to the scheme:

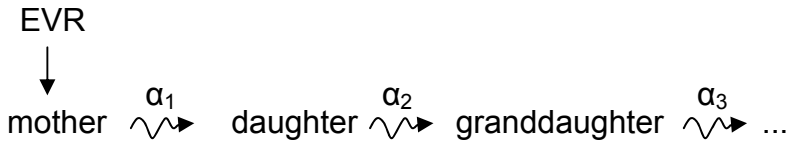

Such a process allows us to search for intrinsic correlations in specified energy and time windows for each of its members, corresponding to their expected α-decay energies and half lives. Inevitable condition for recognition of the correlation chain is the occurrence of the decay of all its members at the same position in the detector within the spatial resolution of the detector. Such a process links the previously identified α-energies and half-lives of daughter and/or granddaughter generations to the corresponding values of unknown mother nuclei.

The method also allows the determination of branching ratios in more complicated modes of decay by introducing the possibility of spontaneous fission or EC-decay.

[1] The technique of α- α correlation is in general useful for identifying unknown isotopes. For known isotopes it is sometimes useful to distinguish them, if several isotopes have similar decay energies

3.1.1.2 α − γ coincidences

Due to the very low production cross-sections, information on nuclear structure in the transfermium region depends almost entirely on the tool of α-decay measurements. Only limited information on nuclear structure could be drawn on the basis of Nilsson levels for transfermium isotopes in connection with hindrance factors of α-decays. Enhanced sensitivity of experimental setups makes it now possible to detect γ-rays and conversion electrons in coincidence with α–decay of a given recoil.

These γ-rays are emitted in cascades de-exciting the daughter nucleus to provide insight into the structure of the level scheme. Along with γ-rays, X-rays can be observed in coincidence to α-decays, indicating that the levels populated by this α-decay de-excite by internal conversion.

Successful decay studies by the α-γ coincidence method were recently performed at SHIP, for example on isotopes ^{253}No [94] and ^{255}No [95]. Positive results gave way to new investigations of neutron deficient isotopes of mendelevium, nobelium, and lawrencium.

3.1.1.3 Electron tagging technique

Recently, a new tagging method was put in operation in data analysis of experimental runs at SHIP. For the sake of identification of new isomeric states in transfermium isotopes an α–γ correlation analysis method was introduced. In contrast to α-γ coincidence measurements, this procedure requires a time difference between the α-particle and the γ-quantum larger than 4μs (time defining a single event). In order to do this, γ-acquisition must run in a "free" mode, meaning that all γ-events are being recorded, not just those accompanying other events within a 4 μs time window. This of course introduces a large γ-background and in many cases makes it impossible to observe true γ-events originating from an isomeric-state populated either by a preceding α-decay or a recoil implantation. Therefore, advantage was taken from the fact that the de-excitation of such isomeric levels often proceeds through a series of several levels decaying by both internal conversion and γ-decay in one prompt cascade. Internal conversion electrons originating from such a cascade are recorded in the lower part of the low energy spectra (~ 50 - 600 keV). It was possible to clear the spectra from unwanted background by requiring coincidences between these electrons and γ-events.

Indeed, by an EVR → e^--γ correlation analysis it was possible to identify K-isomers in the isotopes ^{252,254}No in experiments at SHIP.

3.2 Overview of operation principles for the detection of ionizing radiation

In this part a short overview of the operation principles of the detectors for nuclear structure and nuclear spectroscopy studies is given.

3.2.1 Gas Ionization Chamber

Most gas detectors register the ionization produced by the passage of a charged particle through a gas by collecting the ionization products or induced charges onto electrodes. The average energy needed to produce an electron–ion pair is 30±10 eV, with a weak dependence on the gas used and the energy of the incident particle.

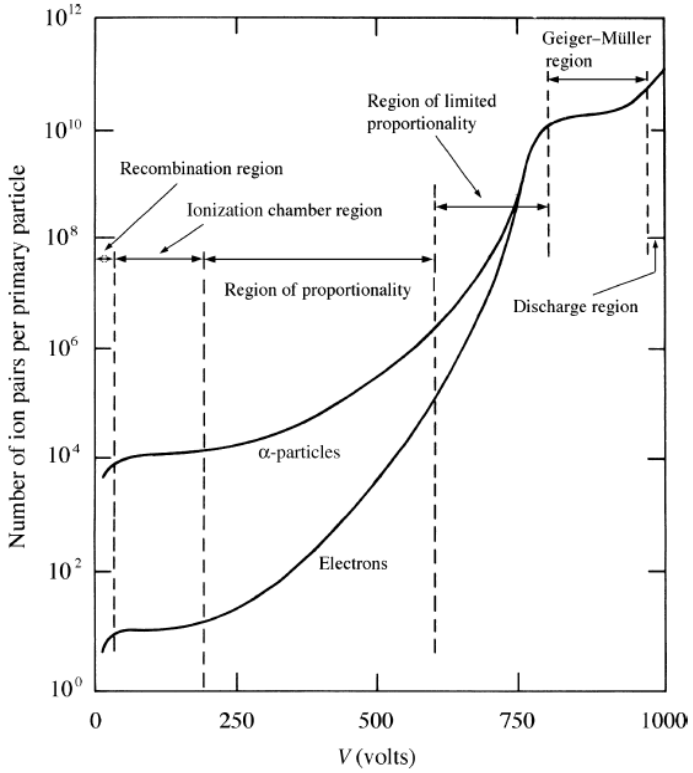

Fig. 3.1: Gas amplification factor as a function of voltage V applied in a single-wire gas detector with a wire radius of typically 20 mm for strongly ionizing particles (α-particles) and weakly ionizing particles (electrons).

To understand the principles of gas ionization detectors Fig. 3.1 shows the number of ion pairs produced per incident charged particle (the gas amplification factor) as a

function of the applied voltage V for two cases: a heavily ionizing particle (e.g. an alpha particle – upper curve) and a lightly ionizing particle (e.g. an electron – lower curve).

At low voltages the output signal is very small, because electron–ion pairs recombine before reaching the electrodes, at high voltage the signals are no longer proportional to the number of ions formed and hence the energy deposited by the radiation. These modes of operation are not suitable for effective energy and time measurements.

If the voltage is chosen in between the regions of operation of the ionization chamber and the region of limited proportionality, the proportional region is selected. Charged particles (EVRs) passing through the isobutane (or pentane) gas ionize the gas molecules. In this region, the electrons from the process are accelerated by the electric field within the chamber thus ionizing even more gas molecules. The electrons freed in the secondary ionization are also accelerated and a cascade of charge is detected. As this is a proportional counter, the avalanche terminates when all free electrons have been collected at the anode, and the number of the secondary ionization events is kept proportional to the number of the primary ion pairs formed, although the multiplication factor can be thousands [96].

The earliest detector using this idea was the proportional counter, which consists of a cylindrical tube filled with gas and maintained at a negative potential, and a thin central anode wire at a positive potential. Subsequently, the resolution of proportional counters was greatly improved as a result of the discovery that if many anode wires were arranged in a plane between a common pair of cathode plates, each wire acts as an independent detector. This device is called a Multi Wire Proportional Chamber (MWPC), and was introduced in 1968. An MWPC can achieve spatial resolutions of 200 μm and a time resolution of about 3 ns. A schematic diagram of a simple MWPC detector is shown in Fig. 3.2.

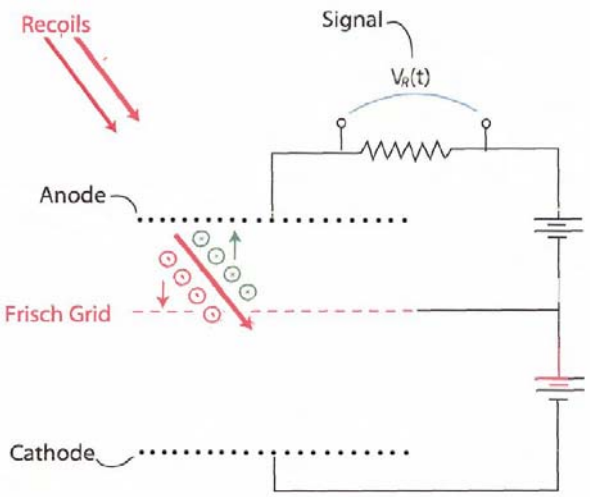

Fig. 3.2: Schematic drawing of a MWPC detector.

The principal function of a MWPC is to distinguish between recoiling reaction products passing through it and their radioactive decays. Ions propagating through the detector generate energy loss, timing, and position signals. The energy loss and timing measurements can be combined with the energy measured in the implantation detector, to obtain a clean distinction between fusion reaction products and scattered beam particles. This is important for maximizing the efficiency for correlating radioactive decays with the correct ion implantation.

3.2.2 Scintillation counters with photomultiplier tubes

For charged particles the energy loss occurs due to excitation and ionization of atomic electrons in the medium of the detector. In so-called scintillators, a small fraction of the excitation energy re-emerges as visible light (or sometimes in the UV region) during de-excitation. In a scintillation counter this light passes down the scintillator and onto the face of a photodetector – a device that converts a weak photon signal to a detectable electric impulse. An important example of a photodetector is the photomultiplier tube, a schematic diagram of which is shown in Fig. 3.3.

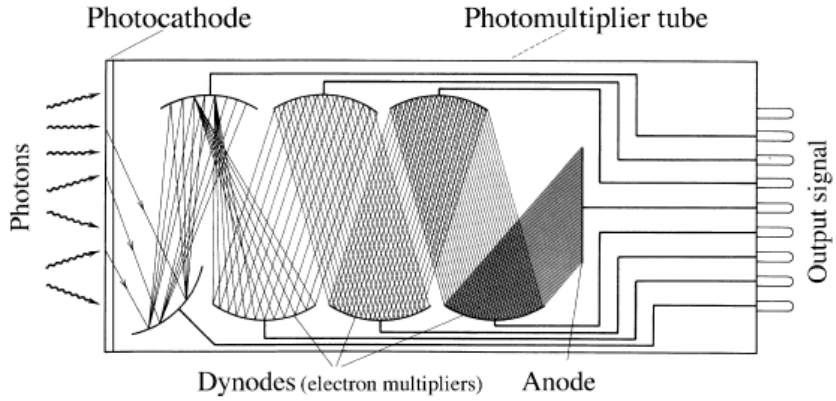

Fig. 3.3 Schematic diagram of the main elements of a photomultiplier.

Electrons are emitted from the cathode of the photomultiplier by the photoelectric effect and strike a series of focusing dynodes. These amplify the electrons by secondary emission at each dynode and accelerate the particles to the next stage. The final signal is extracted from the anode at the end of the tube. The electronic pulse can be shorter than 10 ns if the scintillator has a short decay time.

The scintillation counter is thus an ideal timing device and it is widely used for "triggering" other detectors, i.e. its signal is used to decide whether or not to activate other parts of the detector, and whether to record information from the event. Commonly used scintillators are inorganic single crystals (e.g. cesium iodide) or organic liquids and plastics.

3.2.3 Micro Channel Plates

Micro Channel Plates (MCP) are specially fabricated plates with several million independent channels and each channel works as independent electron multiplier. MCP consist of a two-dimensional periodic array of very-small diameter glass capillaries (channels) fused together and sliced in a thin plate. A single incident particle (ion, electron, photon etc.) enters a channel and emits an electron from the channel wall. Secondary electrons are accelerated by an electric field developed by a voltage applied across the both ends of the MCP. They travel along their parabolic trajectories until they in turn strike the channel surface, thus producing more secondary electrons. This process is repeated many times along the channel; as a result, this cascade process yields a cloud of several thousand electrons, which emerge from the rear of the plate (see Fig. 3.4). If two or more MCPs are operated in series, a single input event will generate a pulse of 10^8 or more electrons at the output.

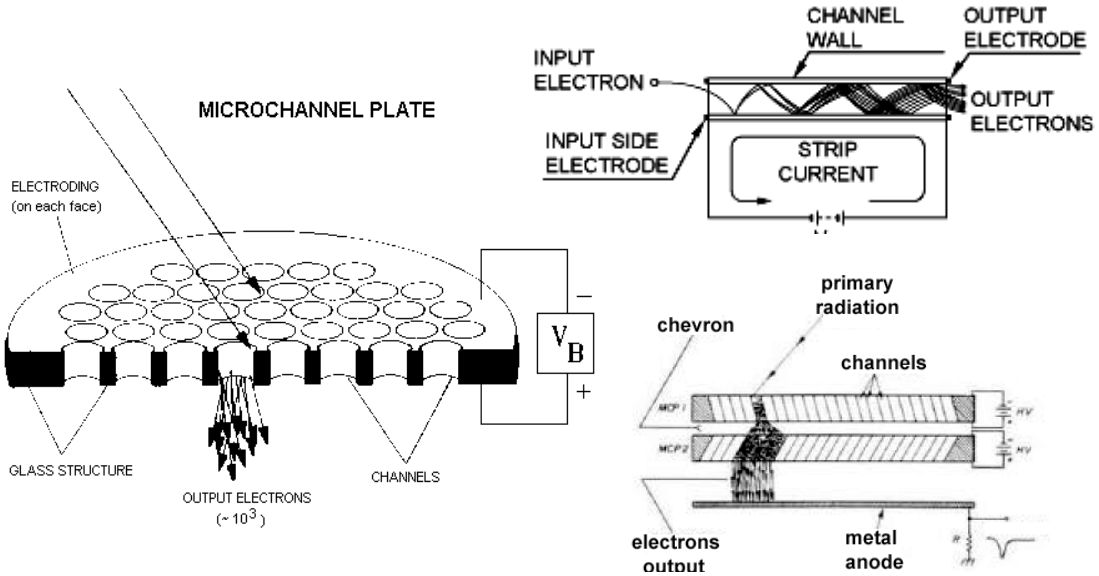

Fig. 3.4**:** Schematic of a continuous channel electron multiplier and two micro-channel plates in a chevron configuration in front of an anode.

Since the individual channels confine the pulse, the spatial pattern of electron pulses at the rear of the plate preserves the image-pattern of particles incident on the front surface. The output signals are typically collected in any of several ways, including metal or multimetal anodes, resistive anodes (one- or two- dimensional), wedge and strip anodes, delay-line readouts, or on a phosphor screen deposited on a fiberoptic or other substrate.

Usually in SHE experiments, MCPs are used to detect secondary electrons produced when a beam or recoil ion passes through a thin carbon or metal foil. The foil is placed orthogonal to the path of the ions, and the produced secondary electrons can be reflected by an electromagnetic mirror to an MCP positioned out of the beam axis, as shown in Fig. 3.5. These thin foils serve the dual role of producing these electrons as well as providing an electrode for the electric field. The foil has typically a thickness of 10 $\mu g/cm^2$ to minimize energy loss and scattering. These components together form a TOF (time-of-flight) detector which provides a start signal for time-of-flight measurements (the stop signal is provided by a second combination of the same detectors or by focal plane silicon detector. Micro Channel Plates work only at high vacuum (about 10^{-6} bar). Typical MCP dimensions usually are not more than 80 x 60 mm^2.

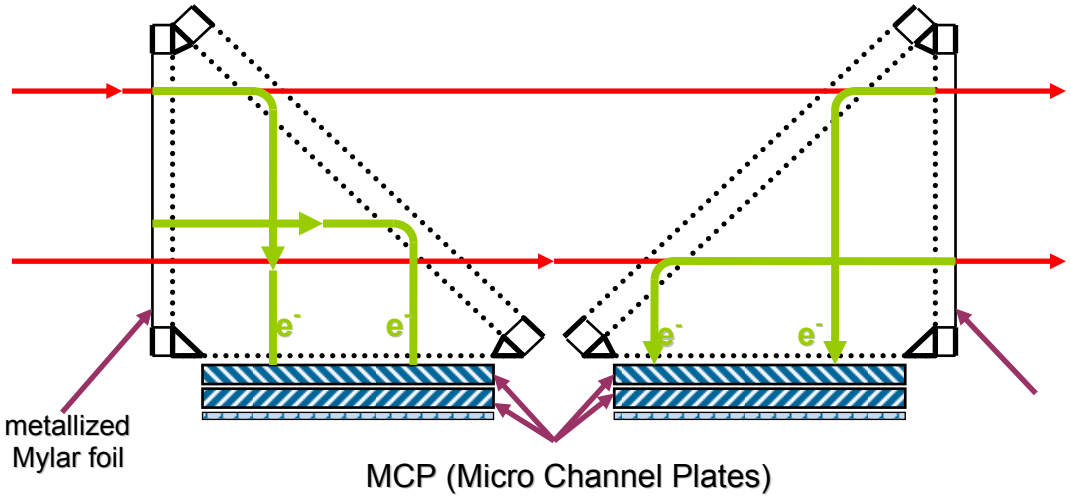

Fig. 3.5: Schematic of a timing detector based on a chevron MCP configuration.

3.2.4 Semiconductor detectors

Solid-state detectors operate through the promotion of electrons from the valence band of a solid to the conduction band as a result of the entry of the incident particle into the solid. The resulting absence of an electron in the valence band (a 'hole') behaves like a positron. Semiconductor detectors are essentially solid-state ionization chambers with the electron–hole pairs playing the role of electron–ion pairs in gas detectors. In the presence of an electric field, the electrons and holes separate and collect at the electrodes, giving a signal proportional to the energy loss of the incident charged particle. Most semiconductor detectors use the principle of the junction diode. Since the band gap in some solids is as small as 1 eV and the energy loss required to produce a pair is only 3 – 4 eV on average (cf. the 30 eV required in a gas detector), a very large number of electron–hole pairs with only a small statistical fluctuation will be produced by a low-energy particle. Solid-state detectors are therefore very useful in detecting low-energy particles. Semiconductors (principally silicon or germanium) are used as a compromise between materials that have residual conductivity sufficient to enable conduction pulses due to single particles to be distinguished above background and those in which the charge carriers are not rapidly trapped in impurities in the material.

The most interesting semiconductor devices are those, which have position sensitivity. A simple silicon detector provides a spatial resolution not better than the size of the detector itself. However, it is possible to segment one (or both) of the electrodes into independent strips. If one electrode has parallel strips in one direction, and the other one

has strips orthogonal to these, then the detector is divided into N_f x N_b segments, where N_f and N_b are the number of strips on the front and back of the detector respectively (Fig. 3.6). When an electron-hole pair is produced, they migrate to the nearest anode and cathode strips respectively, producing two coincident signals which can be recognized as a single event at a particular position on the detector.

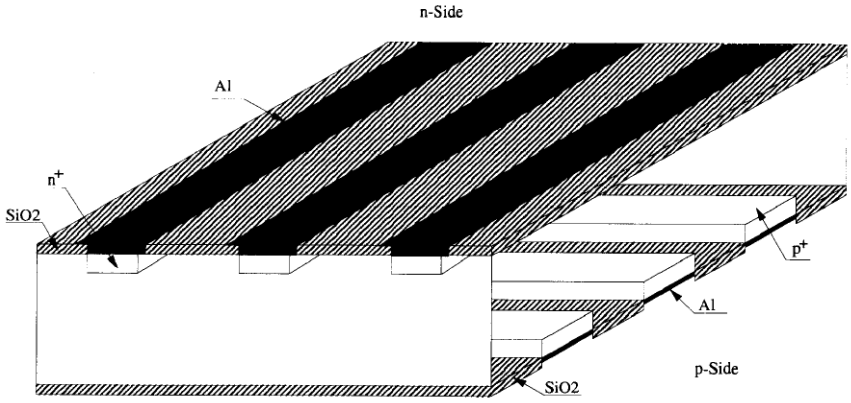

Fig. 3.6: The geometry of a Double Sided Silicon Strip Detector (DSSSD).

Another type of semiconductor detector with spatial resolution are Position Sensitive Silicon Strip Detectors (PSSSD). These detectors are similar to the usual strip detectors, but at the front surface the strips are covered with a resistive layer. Signals are produced from both the top and bottom of the strip when an EVR implantation or radioactive decay occurs, allowing the vertical position of events to be determined. The position of any event is determined by resistive charge division, so that the position is [97]:

$$Position \approx \frac{Q_T - Q_B}{Q_T + Q_B}$$

where Q_T is the charge collected at the top of the strip and Q_B is the charge collected at the bottom of the strip. This definition gives positions from -1 to +1, where -1 is at the bottom of the strip and +1 is at the top of the strip. Multiplying this position by half the strip height gives the absolute position P. The energy of any event is proportional to $Q_T + Q_B$. Usually, resistive layers on the surface of the detector are very sensitive to temperature and are not absolutely homogeneous. So, position calibration for this type of detectors must be done before the experiment and checked from time to time throughout the experiment. Possible spatial resolution of PSSSDs is about 0.3 - 0.6 mm (FWHM).

3.3 Technical aspects of detection systems

In order to achieve the necessary level of sensitivity, a detection system deployed at the focal plane of a high-transmission recoil separator must be highly segmented, provide excellent energy resolution and have the highest possible efficiency. Furthermore, the large number of detector signals must be read out at high rates and the events of interest selected according to temporal and spatial relations.

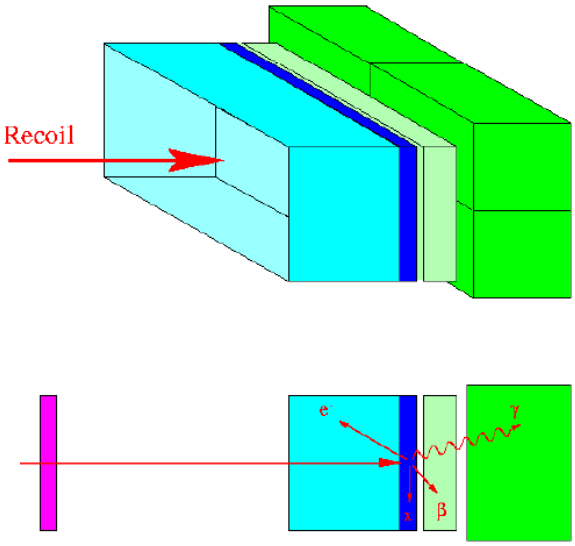

Fig. 3.7: Scheme of a focal plane detection setup of a recoil separator such as RITU, SHIP, or TASCA. The blue shaded regions represent silicon detectors (light blue: side detectors; dark blue stop detector), the green shaded regions germanium detectors (light green: segmented planar Ge detector, dark green: clover Ge detectors). For clarity, the multiwire proportional counter (magenta), through which the recoils pass, is not shown in the upper figure.

The detection system (see Fig. 3.7) for SHE must be designed according to the properties of reaction products and image size of the focal plane of the recoil separator. It can comprise several of distinct components:

1) position sensitive silicon detectors, into which the reaction products are implanted and used to measure subsequent α-particle, β-particle, or proton emission
2) an array of silicon PIN photodiodes or Single Sided Silicon Strip Detectors (SSSSD) to measure conversion electron, escape α-particles, and fission fragments

3) a double sided planar germanium strip detector to measure the energies of X-rays, low energy γ-rays. and β-particles
4) a high efficiency segmented germanium cluster detector to measure the energies of high energy γ-rays
5) a multi wire proportional counter in front of the silicon strip detectors to act as recoil discriminator

The energies of conversion electrons emitted by implanted nuclei through decays of excited states and energies of escaped α-particles can be measured by backward silicon detectors surrounding the implantation silicon strip detector. This requires extremely low (< 5 keV) intrinsic noise for each channel and high geometrical efficiency, allowing excellent energy resolution. In order to obtain the best possible energy resolution this array must be cooled down. The implantation detector is a position sensitive Si detector for detection of EVR's, α-particles, SF fragments, and conversion electrons. It must have a good energy and position resolutions and high detection efficiency.

The silicon strip detectors and the germanium detectors should be segmented in order to enable a position correlated search for associated decays in the particle detectors. The separation of the photon energy range by use of two types of germanium detectors (planar germanium strip detector and cluster detector) gives the greatest flexibility and performance. Such a detection system provides the capability to measure all types of radioactive decays of reaction products and is therefore suitable for radioactive decay– and nuclear structure studies.

A large area planar germanium detector should provide efficient high-resolution detection of low-energy (~ 10 keV to 200 keV) photons and high-energy β-particles. The planar detector can be position sensitive on both surfaces to allow events to be spatially correlated to decays within the silicon strip detectors.

The main design criteria for the high energy (~ 100 keV to ~ 5 MeV photons) germanium cluster detector is that it should have high photopeak efficiency and have sufficient position sensitivity. Another design consideration is that the detector geometry should match that of the focal plane of the spectrometer. Because of the single germanium crystal size limitations, the cluster detector can be made up of several crystals packed closely together in the same cryostat. The efficiency of the cluster

detector can be enhanced significantly by summing signals corresponding to scattered events between adjacent crystals.

Additional detection system called Multi Wire Proportional Counter (MWPC) must be positioned in front of the silicon strip detectors. The MWPC allows distinguishing between evaporation residues and unwanted scattered beam on the basis of their energy loss characteristics in the gas of the MWPC. The MWPC registers the flight of an ion towards the focal plane and measures its energy loss and position. Another vital role of the MWPC is to discriminate between recoils, which generate MWPC signals in coincidence with the silicon strip detectors, and radioactive decays of previously implanted ions, which generate signals in the silicon detector only without triggering the MWPC. The MWPC can also serve for time of flight measurements if two chambers are used producing start and stop signals to better distinguish between different types of ions. The Focal Plane Detector (FPD) can be used also as stop signal detector.

The installation of a Time Of Flight Detector (TOF) before the FPD can also significantly help to reduce background events as follows: If an EVR is registered in the TOF and afterward an implantation signal with a subsequent α decay is recorded in the FPD, where the energies of both, the EVR and the α-particle lie within a preset energy window and the time interval between the EVR and the α-particle lies within a preset time window, the beam is switched off. This has the benefit of strongly reducing the rate of background products associated with implantation of EVRs, transfer products, or scattered projectiles in the FPD, which is important for the detection of further members of the decay chain, especially if the half-lives of daughter nuclei are long. Fig. 3.8 illustrates this case schematically.

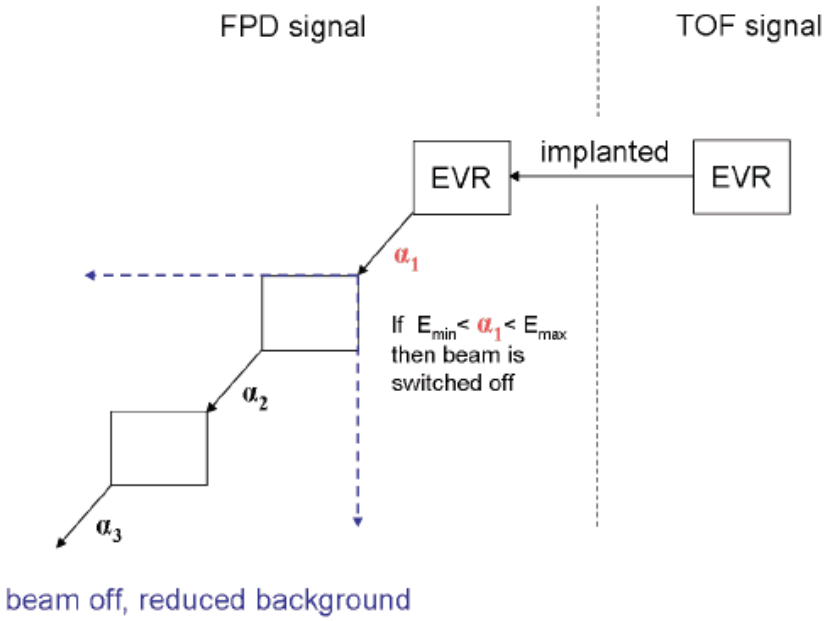

Fig. 3.8: Illustration of how a time of flight detector can help to reduce the background in superheavy element experiments. Once a recoil form the target is detected in the TOF detector the electronic is alerted for a possible detection of an EVR impact and subsequent α decay in the focal plane detector. If the EVR is registered in the FPD and an α-particle is detected in a preset time and energy window, the beam is switched off to increase sensitivity due to background reduction.

The MWPC usually comprises four wire planes and two thin Mylar windows. Position information is obtained from delay line readouts from the ends of vertical and horizontal wire planes and from a fast signal from an anode wire plane. Right/left and up/down signals can then be generated from the time differences between the fast signal and the delayed signals from the delay lines as measured by four Time to Amplitude Converters (TAC). Position resolutions of the order of 1 mm can be achieved. The energy loss of ions passing through the MWPC is derived using signals from a cathode wire plane. The MWPC is usually filled with a few Torr of isobutane or pentane gas, which circulates and is maintained at a constant pressure.

3.4 Presently existing detection systems of several separators for SHE research

As already described previously, there are two general classes of devices, namely separators operating in vacuum, which use magnetic and/or electrostatic deflection elements, as well as gas-filled magnetic separators. The operation principles of these devices are different, but the detection systems to register radioactive decay chains registration are similar. The dimensions of the detector setups are chosen according to the technical details of the separators: planned reactions, ion-optical parameters, and image size of the products in the focal plane. A table of the main separator parameters and the dimensions of their detection setups is presented below.

Table 3.1. Detector dimensions dependent on the ion-optical properties of the different separators.

Separator	DGFRS	GARIS	RITU	BGS	TASCA		SHIP
					SIM	HTM	
Configuration	Gas-filled separators						Velocity Filter
	DQ_hQ_v	DQ_hQ_vD	$Q_vDQ_hQ_v$	Q_vD_hD	DQ_vQ_h	DQ_hQ_v	
Solid ang., msr	10	12.2	10	45	4.3	13.3	
Bend. angle, deg	23	45+10	25	70	30	30	25
Dispers.ion, cm/%	0.63	0.97	1	2	0.1	0.9	
Detector size, mm^2	120x60	60x60	120x60	180x60			80x35

For gas-filled separators, a large dispersion leads to a larger image size and therefore larger detection size. GARIS has a relatively small detector because it is used to study only cold fusion reactions. In the following the detection systems of these separators will be described in detail.

3.4.1 SHIP

The detector system of the velocity-filter SHIP (see section 2.3.1) consists of three large area Time Of Flight (TOF) detectors, each with two foils, a Position Sensitive Silicon Stripe Detector (PSSSD) divided into 16 strips as a stop detector (made by Canberra), 6 backward detectors (28 strips), three silicon veto detectors and a germanium detector [43]. A block scheme of the basic SHIP detectors and the associated electronics is shown in Fig. 3.9

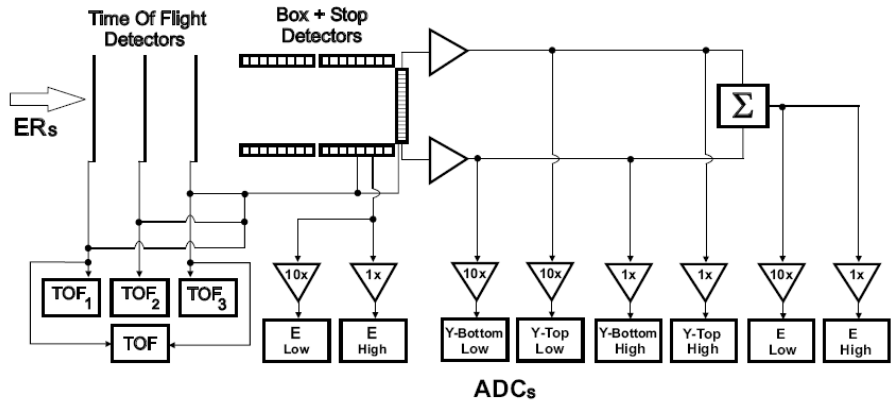

Fig. 3.9: Block scheme of SHIP electronics.

A schematic drawing of a single TOF detector based on Micro Channel Plates (MCP) is presented in Fig. 3.10a. Two foils made of 30 μg/cm^2 thick carbon are needed for each detector. Between the foils an electric potential of 4 kV is applied in order to accelerate electrons emitted from the first foil when a heavy ion passes through. Perpendicularly, a magnetic field is applied in order to bend the electrons onto a micro channel plate for further amplification. The foils are self-supporting and their transmission is nearly 100 %.

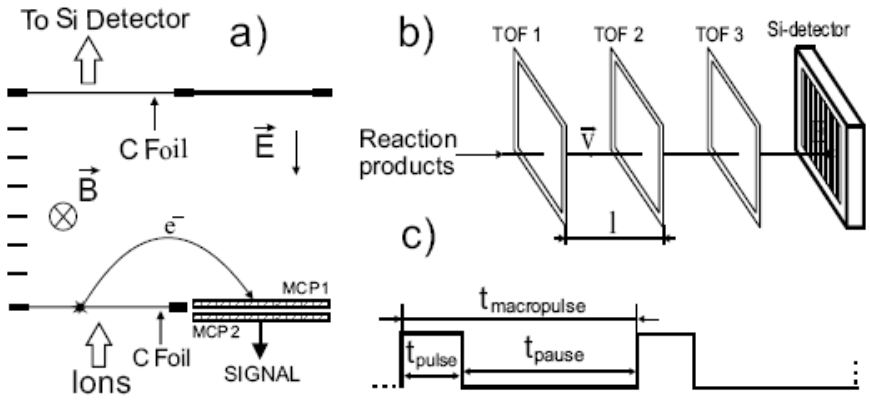

Fig. 3.10: a) Schematic drawing of the working principle of the Time Of Flight detector taken from [98]. Each detector consists of two electron emitting foils. b) Position of the TOF detectors in front of the PSSD. c) Beam macrostructure.

Because of the high efficiency of each of these detectors, the background due to scattered projectiles in the decay spectra is suppressed by a factor of a hundred to thousand as seen from Fig. 3.10b, and the time window for measuring generic parent-daughter decays is significantly prolonged. The time resolution of the foil detectors is about 700 ps. After fulfilling the time and energy condition, the beam is switched off for

a first time interval, while counting for a preset number of α-decays of defined energy opens.

The active area of the PSSSD silicon wafer is 80 × 35 mm^2. Each strip on this wafer is 5 mm wide and has position sensitivity in the vertical direction with a relative resolution of 350 μm (FWHM) for α-decays. For that reason, the stop detector is equivalent to ~ 1600 single detectors, each with an active area of 5 × 0.35 mm^2. The energy resolution is 14 keV for α-particles from a ^{241}Am source measured in a single strip. The resolution is worse (about 20 keV FWHM) when a summed spectrum from all stripes is generated. Fig. 3.11 shows an intensity-, position-, and energy distribution of α-particles and also particles implanted into the detector (background) across the focal plane. The energy spectrum also contains background from scattered projectiles and β-decays.

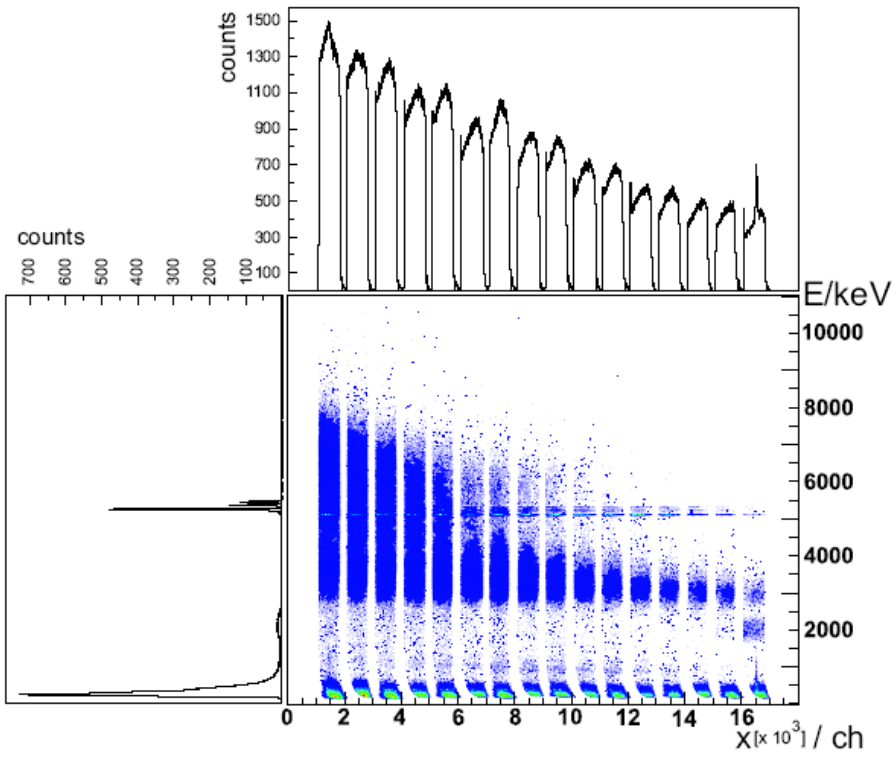

Fig. 3.11: Energy over horizontal position spectrum for all 16 strips of the PSSSD. Each point within the central plot represents one event. Position is defined as: (strip number × 1000 + position in the strip) and the energies are in keV. The integral distributions are plotted on the sides.

Six similar wafers are mounted in the back hemisphere facing the stop detector. This configuration, called a box detector, is for measuring escaping α-particles or fission fragments with a solid angle of 80 % of 2π (in combination with the FPD). In the back detectors, neighboring strips are connected galvanically, forming 24 segments

without position sensitivity. The energy resolution obtained by summing the energy-loss signal from the stop detector and the residual energy from the box detector can reach about 40 keV for α-particles in the best cases. All silicon detectors are cooled to 263 K.

Behind the stop detector another silicon detector (veto detector) is placed. The signals from this detector are used to eliminate high energy light particles (mainly protons) from the analysis, which are not recognized by the time-of-flight system, and pass through the stop detector.

The germanium CLOVER detector consists of four crystals, measuring X-rays and γ-rays, allowing the detection of coincident or delayed α-γ, EVR-γ or SF-γ events within a time window of 5 μs. In particular, this allows the detection of α-transitions to excited levels in the daughter nucleus, which decay by gamma emission. Gamma-rays in coincidence with signals from the high energy region in the FPD can be used as a confirmation of spontaneous fission events. The probability for detecting coincident α–γ events was estimated to be about ~ 14 % in the energy region of interest (100 - 300) keV.

3.4.2 VASSILISSA

The detection system of the electrostatic separator VASSILISSA installed in Dubna, Russia [99] consists of two start and stop time of flight detectors [100] and an array of silicon detectors installed in the focal plane made by CANBERRA. Thin plastic foils (30 - 70 μg/cm^2 thickness, 80 mm diameter) emitting secondary electrons and micro channel plates for detecting these electrons are used in both time of flight detectors. A typical time resolution of about 0.5 ns was obtained for slow recoil nuclei of 10 - 20 MeV with mass numbers of about 200. A value of 99.95% was achieved for the probability of detection of such recoil nuclei by making use of a single timing detector. Having passed the time of flight detectors, the recoil nuclei are implanted into the silicon detectors.

The silicon detector array consists of five identical 16-strip silicon detectors with an active area of 60 x 60mm^2 (Fig. 3.12). The stop detector is position sensitive in the vertical direction with a spatial resolution of 0.3 - 0.5 mm (FWHM). The average energy resolution is 20 keV for α-particles of a ^{241}Am source. Four single side strip detectors mounted in the backward hemisphere are foreseen for detection of escaping α-particles, conversion electrons, and fission fragments. The total geometrical efficiency

is 85% for detection of a single α-particle, the strips do not have any position resolution and each four neighboring strips are connected galvanically, so that 16 segments are formed. The measurement of the time of flight and energy of the recoil nuclei yields their mass values with an accuracy of about 10% thus allowing separation of EVRs from target-like and beamlike particles using two-dimensional TOF energy spectra. The anticoincidence condition for signals from the time of flight and silicon detectors is used to distinguish between pulses originating from recoil nuclei and their α-decays, i.e. to obtain "clean" α-spectra of recoil nuclei implanted into the silicon detectors.

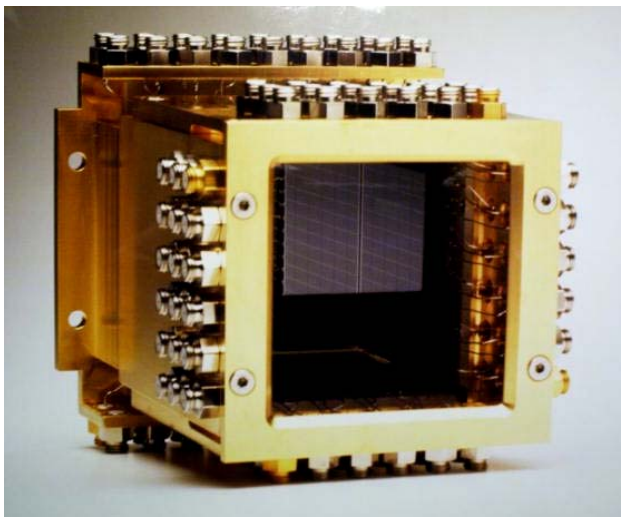

Fig 3.12: View of the VASSILISSA focal plane detector array.

To reduce low-energy background of scattered projectiles or target like ions and to shift their energy distribution to lower energies (less than the range of 6 - 9 MeV) a 200 - 400 μg/cm^2 thick Mylar degrader foil is inserted in front of the silicon detector array.

3.4.3 GARIS

The gas-filled separator GARIS [71] has a similar detection setup as VASSILISSA. Because its detector chamber is separated from the gas volume and operated in vacuum, GARIS has also a TOF system based on MCP plates, as previously described vacuum separators, and an identical silicon detector array as VASSILISSA (Fig. 3.12). A schematic picture of GARIS detection system is shown in Fig. 3.13.

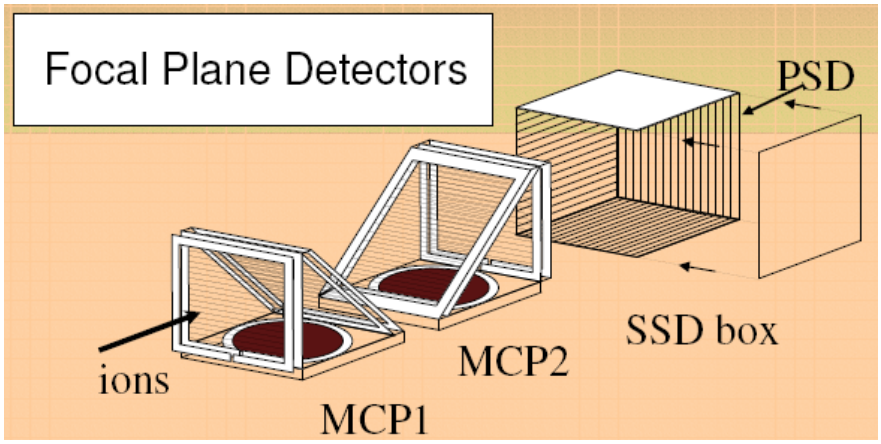

Fig. 3.13: Schematic drawing of the GARIS detection system.

3.4.4 DGFRS

The detection system of the Dubna Gas-filled Recoil Separator (DGFRS) [39] itself consists again of a time of flight system and a silicon focal plane detector (see Fig. 3.14).

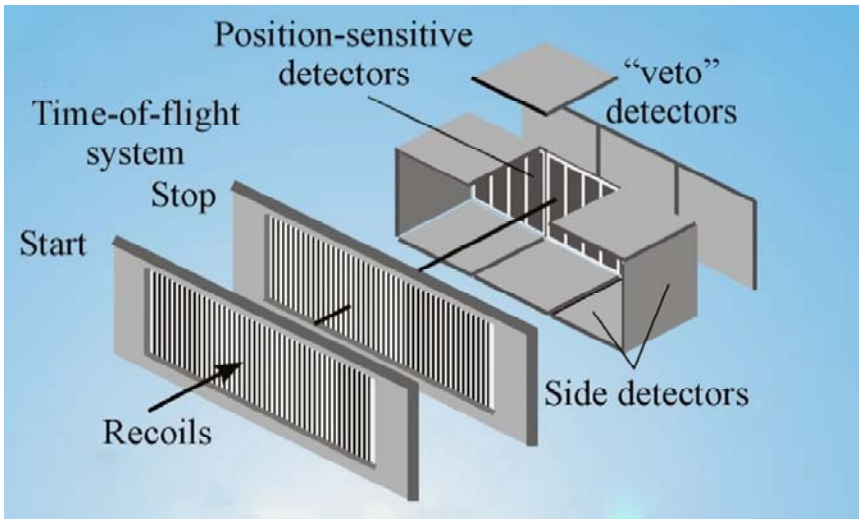

Fig. 3.14: Schematic drawing of the DGFRS detection system.

Before implantation into the detectors, the separated EVRs pass through a TOF measurement system that consists of two start and stop MWPC filled with 1.5 Torr of pentane.

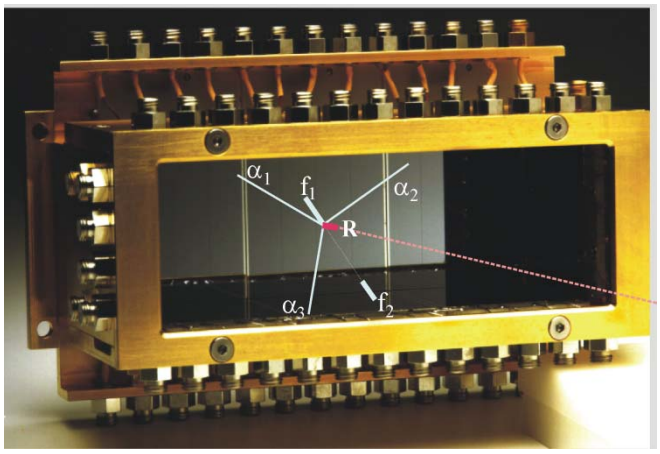

Fig. 3.15: DGFRS detection system.

The stop detector of the focal plane detector array consists of 3 position sensitive silicon strip detectors of 40 x 40 mm^2. In total, 12 vertical strips cover an active area 120 x 40 mm^2, where horizontal (x) positions for the reaction products are obtained by recording the strip number. By measuring signals from both ends of each strip, vertical positions (y) are determined by resistive charge division in the resistive layer. This detector is surrounded by eight 4-strip 4 x 4 cm^2 side detectors without position sensitivity, forming a box around the focal plane detector open to the front side (Fig. 3.15). The detection efficiency for α-decays of implanted nuclei is 87% of 4π. The detection efficiency was tested by registering recoil nuclei, α-decays, and spontaneous fission SF-decays of known isotopes of No and Th, as well as their descendants, produced in the reactions ^{206}Pb(^{48}Ca, 2n) and ^{nat}Yb(^{48}Ca, 3–5n). The efficiency of the TOF module to suppress scattered heavy ^{48}Ca ions was measured to be about 99.996% in the ^{nat}Yb(^{48}Ca,3–5n) reaction. Fission fragments from implanted ^{252}No were used for a fission–energy calibration. A silicon veto detector is placed behind the focal-plane as close as possible from the viewpoint of detector housing design to reject long-path events from light charged particles coming mostly from collisions with the gas and creating no signal in the TOF module. The veto detector is of the same type as the focal plane detector.

3.4.5. BGS

Another gas-filled separator is the BGS (Berkeley Gas-filled Separator), installed in Berkeley, California [67-69]. Before ions are implanted into a FPD, they pass a multi-wire proportional counter, acting as a TOF detector.

The MWPC is a chamber filled with isobutane gas that is isolated by two 0.9-μm thick Mylar windows. The counting chamber contains a central cathode made of metalized polyester foil, and two anode wire grids. The pressure in the MWPC is 3 mbar above the gas pressure in the BGS (usually 0.5 - 1 mbar). The FPD is located approximately 23 cm downstream from the MWPC.

The FPD consists of an implantation detector and a backward detector array. The implantation detector consists of three silicon wafers (each 60 x 60 mm^2), each comprising 16 vertical strips, giving a total of 48 silicon strips which provide horizontal resolution. The vertical position is determined by resistive charge division [97] from charges collected at the top and the bottom of each strip.

Eight additional silicon detectors, each with 4 sets of 4 strips galvanically connected, were mounted perpendicular to the focal plane detector giving a total of 32 signals. This non-position-sensitive backward detector array together with the focal plane detector forms a five-sided box configuration with a base of 180 x 60 mm^2. This configuration provides additional detection efficiency for α-particles or fission fragments emitted from species implanted in the surface of the focal plane detector. When an α-particle or fission fragments are detected both in the focal plane detector and in the upstream detector, the total energy is then the sum of focal plane and upstream energies. The addition of upstream detectors increased the overall efficiency for detection of α-particles from 51% of 4π (when the α-particles deposited their full energy into the FPD), to 75% of 4π (when the α-particles deposit a fraction of their energy in the implantation detector and hit the upstream detector).

The remaining 25% of α-particles either leave a partial signal in the implantation detector while escaping through the front of the detector (~ 16%), or they lack sufficient energy to trigger the data acquisition system (~8%).

A veto detector, consisting of 3 silicon wafers (each with 4 sets of 4 strips joined together, resulting in a total of 12 electronic channels) was mounted directly behind the FPD. Any signal in the punch-through veto detector, typically coming from light and low-ionizing particles passing through the focal plane detector chips, is used to veto any

other coincident signals coming from other detectors in the offline analysis. The five-sided box configuration of the FPD is shown in Fig. 3.16. A side view of the detector box is shown in Fig. 3.17.

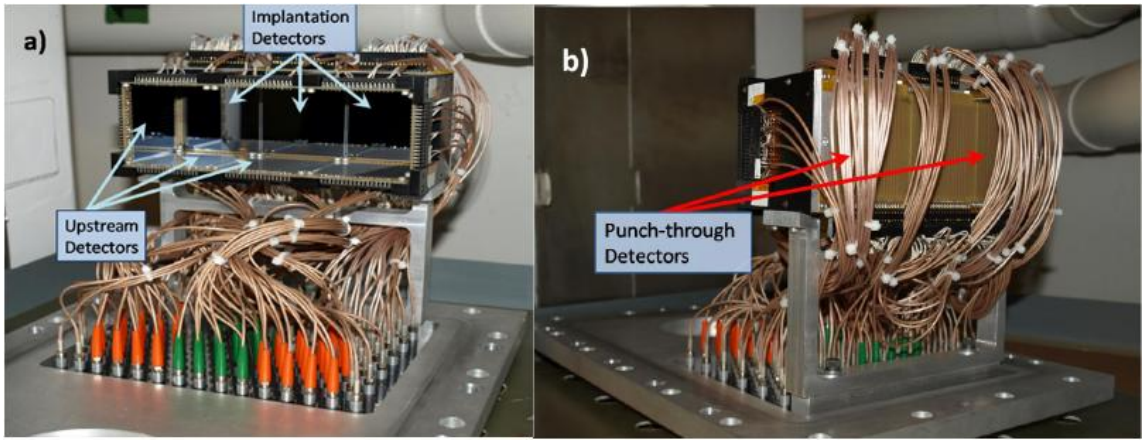

Fig. 3.16: The BGS Focal Plane Detector array (shown upside-down). a) The implantation and backward detectors are shown. b) A view from the backside of the FPD. The veto detectors are mounted directly behind the implantation detectors.

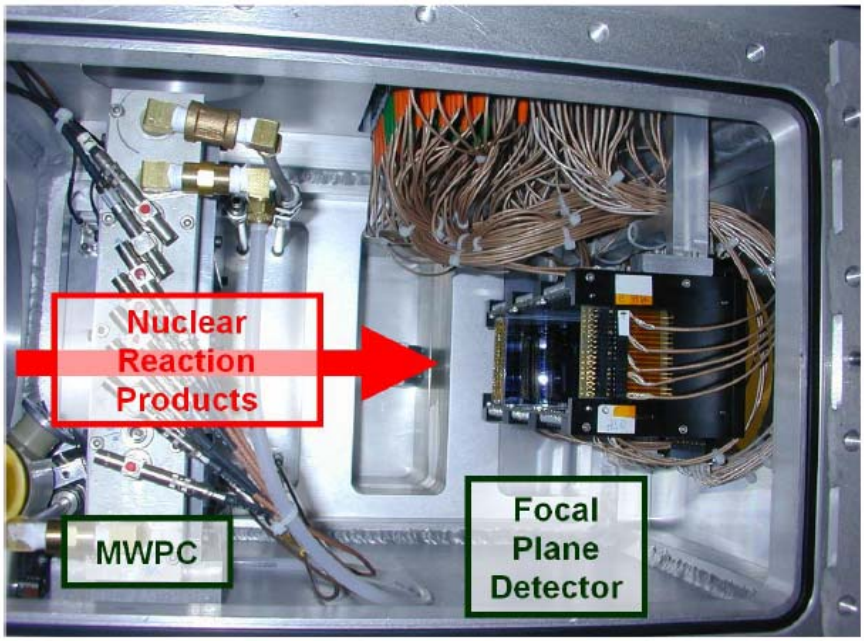

Fig. 3.17: The inside view of the detector box.

3.4.6 RITU

RITU is a gas-filled separator in Juväskylä, Finland [101] working in the research field of spectroscopy of heavy nuclei. The RITU detection system is the only one of all previously described ones, which has a stop detector consisting of Double Sided Silicon Stripe Detectors (DSSSD). The Gamma Recoil Electron Alpha Tagging (GREAT) spectrometer heralds a new generation of implantation detection systems, holistically designed to measure protons, α-particles, β-particles, γ-rays, X-rays, and conversion electrons emitted by reaction products transported to focal planes of recoil separators. GREAT comprises a combination of gas, silicon, and germanium detectors optimized for the study of nuclei produced with very low cross-sections down to the level of pb. GREAT can either be used on its own for focal plane decay studies, or in conjunction with prompt radiation detector arrays deployed at the target position, as a tagging spectrometer for Recoil-Decay Tagging (RDT) [102,103] experiments. One of the limitations of this delayed coincidence technique is the severe dead time losses in the data acquisition system. A novel triggerless data acquisition method, Total Data Readout (TDR), has therefore been developed for GREAT to circumvent this problem [104]. The detection elements that make up GREAT are shown schematically in Fig. 3.18.

A transmission MWPC is positioned at the entrance of GREAT. The MWPC has an aperture of 131 mm (horizontal) x 50 mm (vertical), with a central vertical 1 mm wide strut to support the thin Mylar foil entrance and exit windows. The entrance window separates the isobutane of the MWPC from the low-pressure helium gas of RITU, while the exit window separates the isobutane from the vacuum in which other GREAT detectors are operated.

The transmitted recoils can be slowed down using a system of adjustable degrader foils, before being implanted into a pair of adjacent double sided silicon strip detectors. The DSSSDs are used to measure energies of ions that are implanted and of protons, α-particles, and β-particles they subsequently emit. Each DSSSD has an active area of 60 x 40 mm^2 and a thickness of 300 μm. The strip pitch is 1 mm in both directions, matching the position resolution of the MWPC and giving a total of 4800 pixels. After allowing for the non-uniform distribution of ions across the focal plane, this is at least an order of magnitude increase compared toposition sensitive silicon strip

detectors used previously and provides a significant improvement in correlation performance.

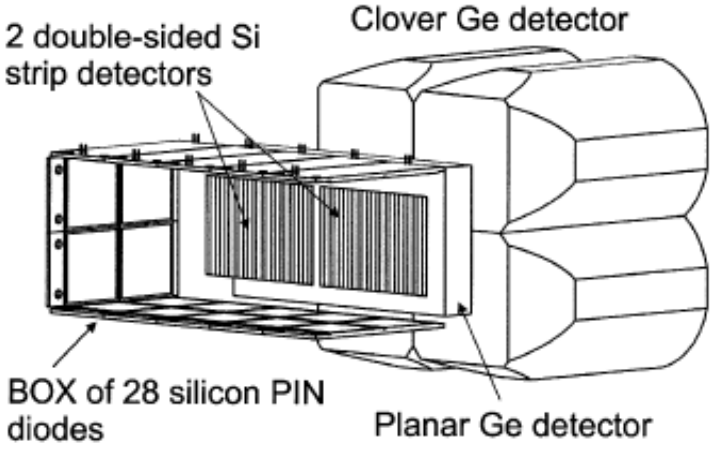

Fig. 3.18: Schematic drawing of GREAT showing the arrangement of silicon and germanium detectors. The separated recoils pass through a multiwire proportional counter (not shown) and enter the detector system from the left.

The DSSSDs are mounted side by side on a hollow block through which coolant is circulated, to reduce their temperature to -20 ˚C. The active areas of the two DSSSDs are separated by a gap of 4 mm, giving an estimated typical recoil collection efficiency of ~ 85%. This compares with ~ 70% for single 80 x 35 mm^2 PSSSD. The strips are individually instrumented using thick-film hybrid charge sensitive preamplifiers [105]. The preamplifier cards are mounted on 10 motherboards that can each accommodate up to 20 modules of either polarity. The motherboards are mounted inside the vacuum chamber on the outside surface of the cooling block and plug directly into connectors on the PCBs housing the DSSSD wafers. This minimizes both the distance and the number of connections between the DSSSDs and the input stage of the preamplifiers, thereby maximizing the energy resolution.

Reaction products are typically implanted into the DSSSDs at depths of ~1 – 10 μm, depending on the target-projectile combination. Conversion electrons that are emitted during a subsequent radioactive decay process therefore have a significant probability of emerging from the DSSSD in the backward hemisphere relative to implantation. An array of 28 silicon PIN diodes is mounted in a box arrangement around the perimeter of the DSSSDs to measure the energies of the conversion electrons.

Fig. 3.19: Photos of the GREAT focal plane silicon detector box at the right-hand side and the FPD with the installed planar germanium detector at the left-hand side.

Each PIN diode has an active area of 28 x 28 mm^2 and has a thickness of 500 um. The PIN diodes are mounted in pairs on a motherboard. The front-end components of the commercial high-resolution charge sensitive preamplifiers are mounted on custom PCBs that plug directly on the back of the motherboards, so as to be as close as possible to the PIN diodes. The 14 motherboards form two rings around the inside surface of the cooling block, so the PIN diodes and the front-end components are all cooled. With this arrangement, an energy resolution of ~ 5 keV can be achieved, which is a marked improvement on the quadrant detectors previously used [106]. The geometrical efficiency of the array is ~30%. This compares with GEANT Monte Carlo simulations that predict that the efficiency for the full energy electron detection in a single PIN diode has a maximum value of ~ 23% for 300 keV electrons, dropping to ~ 13% for 600 keV electrons. However, the probability of electrons scattering between PIN diodes means that the efficiency for registering any signal is significantly higher at ~ 40% for electron energies above ~200 keV. Combined with the lower thresholds that can be achieved with the PIN diode array, this marks another significant improvement in performance.

A planar double-sided germanium strip detector has been designed for GREAT to measure the energies of X-rays and low-energy γ-rays. The rectangular crystal has an active area of 120 x 60 mm^2 and a thickness of 15 mm. The strip pitch on both faces is 5 mm, providing position information that can be correlated with other GREAT detectors.

The detector is housed in its own cryostat and mounted directly behind the SSSSDs, with the front surface of the Ge crystal approximately 10 mm downstream of the DSSSD (Fig. 3.19). It has a thin beryllium entrance window and is mounted inside the vacuum chamber, to minimize attenuation of photons. It can also be used to detect high-energy β-particles (≥ 2 MeV) that penetrate through the DSSSD.

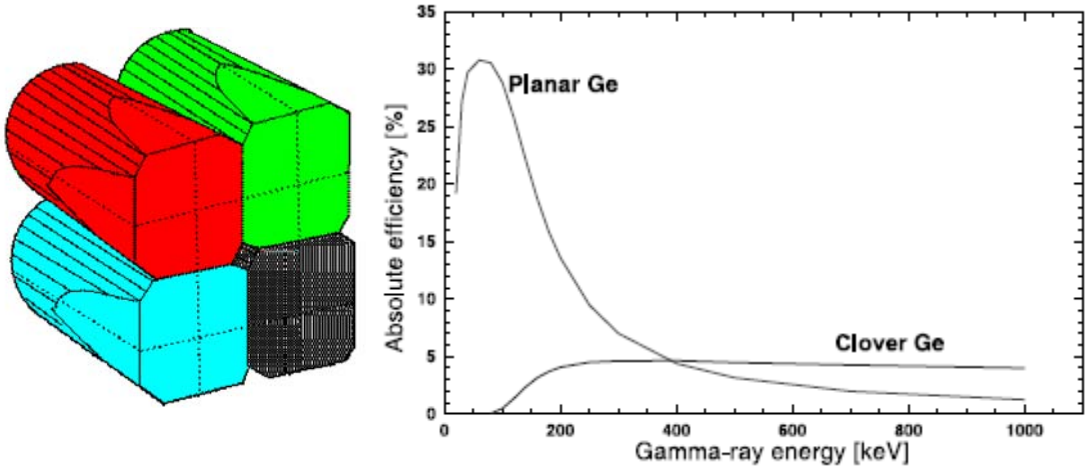

Fig. 3.20: Absolute efficiency of the planar Ge strip detector and the clover Ge detector (a schematic outline is shown on the right-hand side) as a function of γ-ray energy, simulated using the Monte Carlo code GEANT. The simulations assume a realistic source distribution in the DSSSD and take into account the attenuation of γ rays in the intervening materials.

The energies of higher energy γ-rays are measured using a clover Ge detector mounted outside the vacuum chamber. Each of the four crystals has a diameter of 70 mm before shaping and is 105 mm long. The first 30 mm of their length is tapered at an angle of 15˚ on the outside surfaces. The crystals have a fourfold segmentation. The efficiency of the Ge detectors has been simulated using GEANT and is plotted as a function of γ-ray energy in Fig. 3.20. A suppression shield with bismuth germanate crystals, 185 mm long, surrounds the clover detector to improve its peak-to-total ratio (see Fig. 3.21).

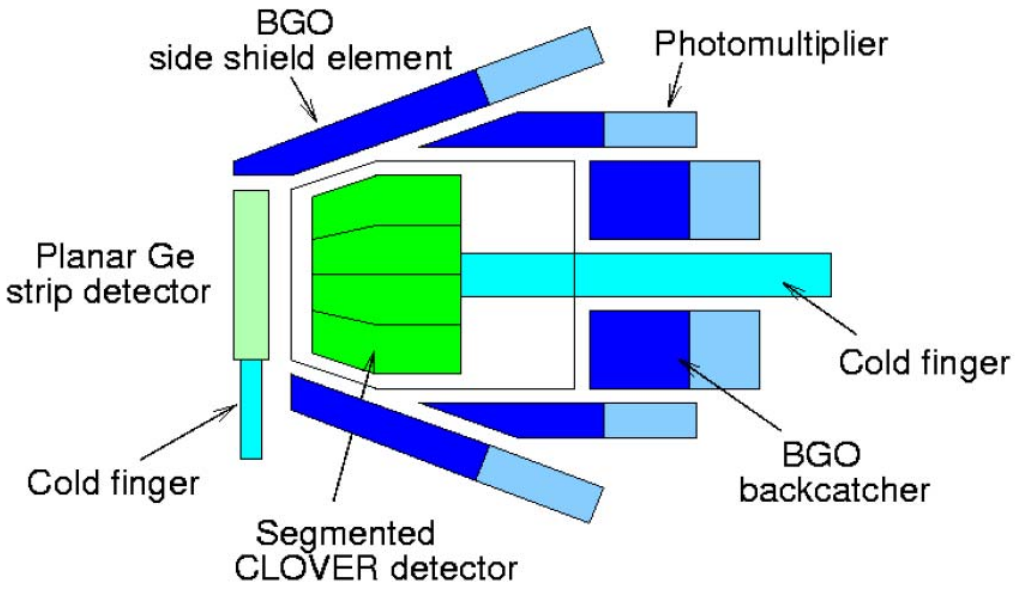

Fig. 3.21: Schematic side view of the planar germanium strip detector, the segmented CLOVER germanium detector and its BGO suppression shield.

3.5 Conclusions

The present thesis deals with the newly built gas filled separator at the GSI in Darmstadt, Germany, designed for research on superheavy elements. This separator, named TASCA (TransActinide Separator and Chemistry Apparatus), is intended to provide new inputs for the investigation of the physical and chemical properties of heaviest elements. The capability of TASCA to perform not only physical but also chemical separation, is one of its great advantages. TASCA's unique ability to run in two working modes, the high transmission (HTM) and the small image mode (SIM), resulting in a high yield and well focused product distribution, respectively, enhances its value especially for chemical experiments.

On 27th April 2006 the first alpha energy spectrum was observed in the focal plane detector of TASCA. The first reaction ^{181}Ta(^{30}Si, xn)$^{211-x}$Fr not only concluded the main building phase of the separator, but also announced the beginning of its commissioning phase, planned on a time scale of 2 years. This thesis contains a brief overview of all kinds of reactions, which were tested during these 2 years, and the results of the last commissioning experiment, starting in April 2008 at TASCA, comprising physical methods of preseparation and chemical quasi-online detection techniques.

At the end of May 2009 a first SHE experiment was planned. Because of the picobarn reaction cross-section, improvements of existing detectors such as switching from position sensitive silicon strip detectors to double sided silicon strip detectors in the focal plane, as well as new additional detectors, for a higher efficiency and better ability of background suppression, were required. Because of the absence of an efficient detection system for SHE studies at TASCA, the main goal of this thesis was the design and development of a new focal plane semiconductor detector array with high geometrical efficiency. All known setups for SHE production at the time used PSSSD detectors as implantation detectors. Only the RITU separator with the GREAT spectrometer used DSSSDs. PSSSDs are already well known, but have certain disadvantages (e.g. position calibration stability), whereas DSSSDs are not studied so precisely, but are devoid of the PSSSDs bugs. Therefore, before the new detection setup development started, both types of detectors must be examined in detail, for a better understanding of the processes taking place in the detectors, especially in the interstrip distances.

In parallel to the ongoing detector developments, further hard- and software developments are constantly required. As will be described in the next chapter, the new detector set-up generates 320 signals, which must be read out and digitized without unacceptable loses of data. Because of severe money and space limitations, it was not possible to build a readout system with usual electronic modules, available on the market. It was necessary to design and produce basically new analogue electronics. In addition, in collaboration with the GSI software department a new Data AcQuisition (DAQ) and analysis programs had to be developed.

Chapter IV

TASCA commissioning program

First steps of TASCA

4.1 TASCA commissioning phase overview

The **T**rans**A**ctinide **S**eparator and **C**hemistry **A**pparatus (**TASCA**) has successfully finished its commissioning phase. A lot of nuclear reactions from very asymmetric, e.g. ^{22}Ne + ^{244}Pu, to symmetric, e.g. ^{64}Ni + ^{150}Nd, have been studied (see Fig. 4.1) during the 2 years of the commissioning phase in order to study and understand the operating parameters of TASCA.

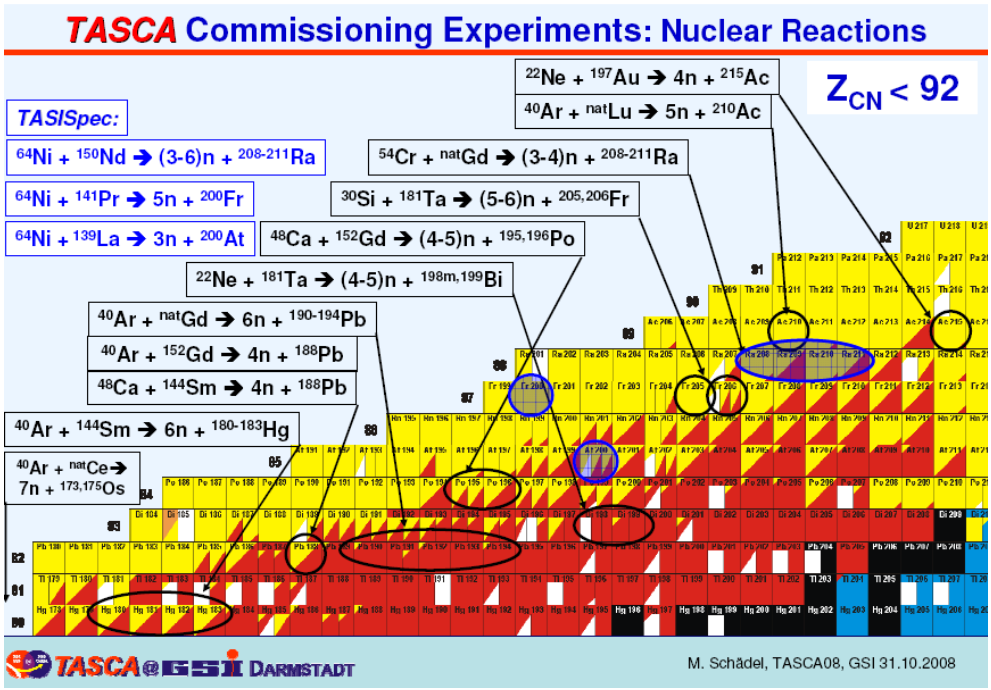

Fig. 4.1: Chart of nuclei and studied nuclear reactions (from a presentation by M. Schädel at the TASCA'08 workshop).

Table 4.1 provides a compilation of all nuclear reactions and reaction products applied in the course of the commissioning program together with the mode TASCA was operated in and the gas filling. Also listed are experiments to test and optimize the Recoil Transfer Chambers (RTC), the gas-jet transport of pre-separated products into the

Rotating wheel On-line Multidetector Analyzer (ROMA) and its performance, and the coupling and use of aqueous chemistry set-ups behind TASCA.

Table 4.1: Nuclear reactions and their products used to commission TASCA; H=HTM, S=SIM, *TAS*=TASISpec, R=ROMA, C=chemistry, catch=catcher foils. [107]

Product	xn	Beam	Target	Mode	Gas	RTC +R/C
^{30}Si	--	^{30}Si	no	H+S	Vac	
^{173,175}Os	7n	^{40}Ar	^{nat}Ce	H	He	C
$^{180-182}$Hg	6n	^{40}Ar	^{144}Sm	H+S	He	C
^{188}Pb	4n	^{48}Ca	^{144}Sm	H+S	He	
^{188}Pb	4n	^{40}Ar	^{152}Gd	H+S	He	
$^{194-196}$Pb	4-5n	^{40}Ar	^{nat}Gd	H+S	He	R
$^{198-199}$Bi	4-5n	^{22}Ne	^{181}Ta	H+S	He	catch
$^{195-196}$Po	4-5n	^{48}Ca	^{152}Gd,	H	He	R
^{200}At	3n	^{64}Ni	^{139}La	*TAS*	He	
^{200}Fr	5n	^{64}Ni	^{141}Pr	*TAS*	He	
$^{205-206}$Fr	5-6n	^{30}Si	^{181}Ta	H	He	
$^{208-211}$Ra	3-4n	^{54}Cr	^{nat}Gd	H+S	He	
$^{208-211}$Ra	3-6n	^{64}Ni	^{150}Nd	*TAS*	He	
^{210}Ac	5n	^{40}Ar	^{nat}Lu	H+S	He,N_2	
^{215}Ac	4n	^{22}Ne	^{179}Au	H+S	He,H_2	
$^{218-x}$Th	xn	^{64}Ni	^{154}Sm	*TAS*	He	
$^{224-x}$U	xn	^{64}Ni	^{nat}Gd	*TAS*	He,H_2	
^{245}Fm	3n	^{40}Ar	^{208}Pb	H+S	He	R
^{252}No	2n	^{48}Ca	^{206}Pb	H+S +*TAS*	He	R
^{253}No	2n	^{48}Ca	^{207}Pb	H +*TAS*	He	
^{254}No	2n	^{48}Ca	^{208}Pb	H+S	He,H_2	
^{255}No	5n	^{22}Ne	^{238}U	H+S	He,H_2	R
^{256}No	4n	^{22}Ne	^{238}U	H	He	
^{260}Rf	6n	^{22}Ne	^{244}Pu	H	He,H_2	
^{261a,261b}Rf	5n	^{22}Ne	^{244}Pu	H	He	R,C
^{262}Rf	4n	^{22}Ne	^{244}Pu	H	He,H_2	

To understand TASCA as a separator and to build up a solid data base providing good predictive power concerning separator operation for future SHE experiments, the following most important parameters were investigated: (i) the magnetic rigidity of reaction products between Z = 76, Os, and Z = 102, No, produced at different recoil

velocities, and the corresponding best settings of the dipole magnet, (ii) the optimum gas pressure with respect to focusing and transmission - being quite different in the HTM and in the SIM -, (iii) the target thickness dependence of the separator transmission – strongly depending on the asymmetry of the nuclear reaction -, and (iv) the quadrupole focusing, which is especially relevant for the SIM. The analysis of a huge amount of data from these experiments is in progress, and it is important to realize that most of the above mentioned parameters are not independent from each other, nevertheless some of the experiments are ready for publishing [108].

The first efficiency measurements with catcher foils behind the target and in the focal plane showed very good agreement with model calculations for the fairly asymmetric reaction ^{22}Ne(^{181}Ta, xn)^{198m,199}Bi [107]. To confirm this agreement in a more symmetric reaction leading to a significantly heavier reaction product and to obtain a standard reaction to test and check the TASCA performance detailed studies were performed with well know reactions of ^{48}Ca with $^{206-208}$Pb leading to $^{252-254}$No. Assuming cross sections of 0.5 µb, 1.3 µb, and 2 µb [108] for the production of ^{252}No, ^{253}No, and ^{254}No, efficiencies of 54%, 56%, and 49% were obtained, respectively, for the HTM, using He as filling gas, and a 80 x 36 mm^2 16-strip PSSSD detector. Taking into account uncertainties in cross sections and systematic errors of target thicknesses and beam current measurements an excellent agreement with model calculations was observed, which [109] predicted a transmission of 52%. Equally good is the agreement in the SIM, at a He pressure of 0.8 mbar, where a 30% efficiency was measured for the reaction ^{48}Ca(^{208}Pb, 2n)^{254}No.

As one of the crucial tests and one of the highlights finalizing the TASCA commissioning program, synthesis of the isotopes ^{260}Rf, ^{261a,261b}Rf, and ^{262}Rf was studied in the very asymmetric reaction ^{22}Ne + ^{244}Pu, which is described in section 4.3.

An additional highlight of the commissioning phase was the first transactinide chemistry behind TASCA designed as a proof-of-principle experiment. It was performed with ARCA with pre-separated 78-s ^{261a}Rf; details of the nuclear reaction and the separation of Rf in TASCA are described in this work, while all chemical aspects are discussed in [110]. This successful experiment which studied the formation of Rf-fluoride complexes and their adsorption behavior on an anion exchange resin, demonstrated that aqueous-phase transactinide chemistry behind TASCA can now be performed.

The new set-up termed *TA*sca *S*mall *I*mage mode *Spe*ctroscopy (TASISpec) [111] exploits advantages of the SIM, i.e. the fact that reaction products can be focused with high efficiency in an area of ~ 3 x 4 cm^2. This provides the unique possibility to built a small Si-detector box for α-particle-, electron-, and fission fragment measurements and to surround it with composite Ge-detectors in very close geometry, resulting in an unprecedented, highly efficient set-up for multi-coincidence measurements with γ-rays and X-rays; see [111] for details of TASISpec. A prototype set-up has been commissioned successfully and first data have been collected for nuclides as heavy as ^{252,253}No.

4.2 Commissioning of the TASCA focal plane detector

During the TASCA commissioning phase competitive tests of two types of focal plane detectors for TASCA – a Position Sensitive Silicon Strip Detector (PSSSD) and a Double Sided Silicon Strip Detector (DSSSD) - have been performed with to make the choice which of the two detector types is more suitable for SHE research. During these tests parameters such as energy and position resolution and detection efficiency were studied for both types of the focal plane detector. This knowledge is used as a basis for the design and manufacturing of a new focal plane detection system for TASCA in the framework of this work.

The 16-strip PSSSD of 80 x 36 mm^2 was used as standard implantation detector during the commissioning phase, the same as the SHIP implantation detector. The thickness of the PSSSD is 300 μm. The test experiments with the PSSSD showed that the image size in the HTM is larger than the detector size (Fig. 4.2) for most of the nuclear reactions, as it was expected according to Monte Carlo simulations [88]. The alpha energy resolution for this type of detector cooled down to -20˚C is about 20 keV for a 8 MeV α-line.

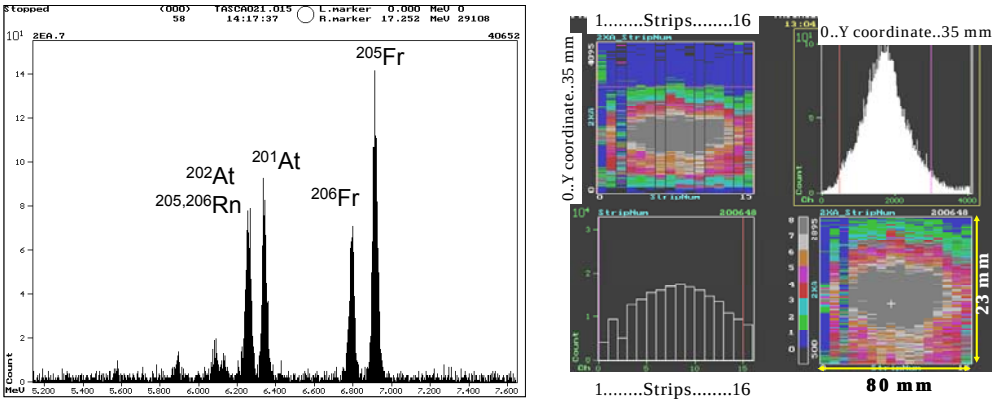

Fig. 4.2: Alpha spectrum and product distribution in the PSSSD detector.

The PSSSD was equipped with the corresponding analogue electronics, which is old and thus was not working reliably. The position resolution of this detector is ± 0.35 mm, in SHE experiments a search for position correlated decay chain members occurs usually within ± 1 mm limits; this corresponds to a pixel size area of 5 x 2 mm^2. The large pixel size makes a search for rare decay chains very difficult because of non-zero background from unwanted products, especially if decay chains have long-lived members.

Some experiments were devoted to test a DSSSD prototype, which is an alternative type of stop detector for the new detection system. We have purchased a 60 x 60 mm^2 DSSSD with 48 strips on the front and the back sides with a thickness of 300 μm (made in Zelenograd, Russia). The strip pitch is 1.208 mm and the pixel size 1.46 mm^2, seven times smaller than for the position sensitive detector. The alpha resolution, as well as the correlated decay chain detection efficiency, have been tested and compared to the PSSSD detector. The resolution of alpha lines in spectra from both front- and back sides are ~ 20 keV for 8 MeV α-line even without cooling (Fig. 4.3).

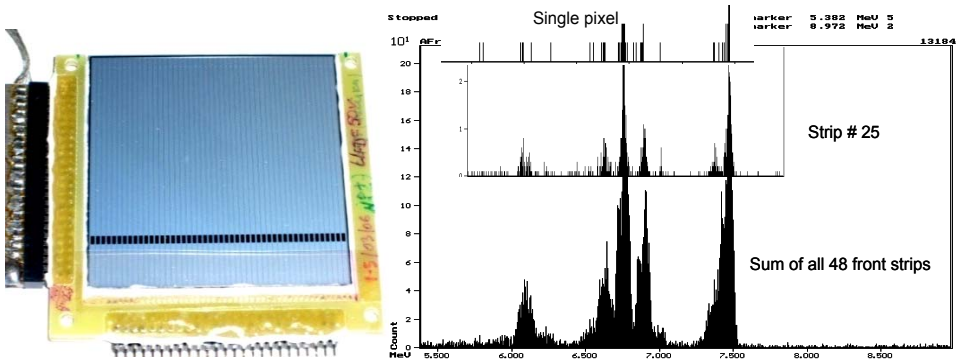

Fig. 4.3: View of the DSSSD prototype detector and alpha particle spectra.

The detection efficiency is comparable to the one of the PSSSD (> 90%), but the search for correlated decay chains is much easier because of the fixed ***x*** and ***y*** coordinates (strip numbers). No position calibrations are needed for the DSSSD, and the smaller pixel size allows search for correlated events also at high counting rates from background activities.

More detailed information about the usage of PSSSD and DSSSD in physics experiments will be given in the next section.

4.3 The final commissioning experiment: Studies on the production of isotopes of the first transactinide element Rf

Studies of the production and decay of isotopes of the heaviest elements at physical recoil separators have a long history. In recent years, the pursuit of finding elements with ever higher atomic number Z has been a key priority. To reach a region close to the predicted spherical nucleus at Z ~ 114 - 126 and N = 184, nuclear fusion reactions of various actinide targets with neutron-rich doubly-magic ^{48}Ca projectiles have been investigated [27]. More than 30 superheavy nuclei with Z = 112, 114 - 116, and 118 have been synthesized and were observed together with their α-decay daughter products. The existence of the "deformed" closed shell predicted at Z = 108 and N = 162 has been confirmed recently through the synthesis of two hassium isotopes ^{270}Hs and ^{271}Hs [47,48].

Neutron-rich Rf isotopes can only be produced via asymmetric nuclear reactions between heavy actinide targets and light beams (A ~ 18 ÷ 30) or reached as daughters in α-decay chains from higher element mothers. On the one hand the increasing half-lives in the vicinity of the deformed nuclear shell N = 162 makes the investigation of

neutron-rich Rf isotopes more demanding, especially using recoil separators. On the other hand, longer half-lives allow applying techniques based on gas-jet transport and chemical separations. The even-even isotope ^{260}Rf decaying by spontaneous fission (SF) with a half-life of 21±1 ms has first been observed by Somerville et al. in 1985 [112] and was confirmed in an experiment by Hulet et al. [113]. Most recently, ^{260}Rf has been measured as an evaporation residue of the reaction ^{238}U(^{26}Mg, 4n)^{260}Rf at the gas filled separator BGS at LBNL, Berkeley. The obtained half-life $T_{1/2} = 22.2^{+3.0}_{-2.4}$ ms is consistent with the previously reported one. The α-decay of ^{260}Rf followed by α-decay of ^{256}No was not observed [114]. The next isotope ^{261}Rf is known since several decades, and it was believed for a long time to decay exclusively by emission of α particles with an energy of 8.28 MeV and a half-life of ~ 65 s [41]. This isotope, produced in the nuclear reactions ^{18}O + ^{248}Cm or ^{22}Ne + ^{244}Pu, has been extensively used for chemical studies of rutherfordium [115-117]. The values for the half-life of ^{261}Rf obtained in several experiments differ slightly: e.g. 78^{+11}_{-6} s [115], 75±7 s [116] and 68±3 s [118-120]; however all authors agree on a α-particle energy E_α=8.29 MeV and a fission branch b_{SF} < 0.11. The first indication of the existence of an isomeric state in ^{261}Rf has been obtained several decades after discovery of ^{261}Rf in experiments at the recoil separator SHIP (GSI, Darmstadt, Germany), where ^{277}Cn was produced, whose decay chain proceeds through ^{261}Rf [43]. Both states have been observed later in chemical studies on Hs isotopes as a decay chain member from ^{269}Hs produced in the reaction ^{26}Mg + ^{248}Cm [46,47,48]. Hereafter, the two states are referred to as ^{261a}Rf, and ^{261b}Rf [57]. The latter state decays by either SF or α particle emission (E_α = 8.51 MeV, b_α =0.09, b_{SF} = 0.91) with a half-life of $T_{1/2}$ = 3±1 s) [48]. The chemistry experiments were not optimized for a 3-s ^{261b}Rf and the SF background was usually not negligible. 42 α-α correlations originated from the decay chain ^{261a}Rf → ^{257}No have been observed in an experiment at the DGFRS, Dubna, Russia to study Rf isotopes produced in the ^{244}Pu(^{22}Ne,*x*n)$^{266-x}$Rf reaction [121]. Assuming an isomeric production ratio σ^{261a}Rf/σ^{261b}Rf of 1 and taking into account the α branch in ^{261b}Rf, about 4 correlations from ^{261b}Rf → ^{257}No could have been expected, while zero were observed, suggesting σ^{261a}Rf/σ^{261b}Rf ≥ 2. Recently, Gates *et al.* studied the reaction ^{238}U(^{26}Mg, 3*n*) [114] and observed one decay chain attributable to ^{261a}Rf as well as one EVR-SF correlation with a lifetime of 9.4 s. This EVR-SF chain would fit to the decay of ^{261b}Rf. The situation concerning the isomeric

production ratio in reactions leading to ^{261}Rf is thus not clear. Conclusive observation of the population of ^{261b}Rf as an EVR is missing.

Knowledge about the heavier neighboring isotope ^{262}Rf is even more obscure. Results from fission track measurements from products implanted into a moving tape obtained in cross bombardments with various actinide targets, were interpreted as SF decay of ^{262}Rf with a half-life of ~ 47 ms [112]. However, due to the absence of any separation of fusion-evaporation products from, e.g., transfer products, a multitude of SF activities with different half-lives were observed, some of which could not be assigned to specific nuclides. In the studies of Sg isotopes produced via the reaction ^{248}Cm(^{22}Ne, xn)$^{270-x}$Sg at the DGFRS and from experiments at GSI Darmstadt on Sg chemistry, the assignment of events to ^{266}Sg were based on α-decay of evaporation residues (EVRs) folloed by SF from ^{262}Rf, while events decaying through a daughter with an α particle energy of ≈ 8.3 MeV were assigned to ^{265}Sg [39,44]. The half-life of ^{262}Rf as the daughter of ^{266}Sg was deduced to be 1.2 s and $2.5^{+2.4}_{-1.6}$ s (68% c.i.) from [39] and [44], respectively. The work using the ^{244}Pu(^{22}Ne,*x*n)$^{266-x}$Rf reaction, where reaction products were thermalized in a recoil chamber and transported by a gas-jet to a rotating-wheel apparatus, reported observation of SF decaying ^{262}Rf with a half-life of 2.1±0.2 s [42]. Later, recoil separator studies of the reaction ^{244}Pu(^{22}Ne,*x*n)$^{266-x}$Rf at DGFRS have been conducted [121]. However, due to the low kinetic energy of EVRs from such an asymmetric reaction, implantation signals were only measured with a low efficiency and no improved data on ^{262}Rf were obtained. The half-life of about 2 s looked consistent after the experiments described above, until two states in ^{261}Rf have been discovered, and new different decay properties were observed for ^{266}Sg as a daughter in decay chains from ^{270}Hs: ^{266}Sg decays by SF with a half-life of 360^{+250}_{-100} ms [48]. A reanalysis of all the data from previous experiments on ^{265,266}Sg isotopes was made recently by Düllmann and Türler [57]. The excitation function (based on ≈ 240 events) reported by Lane et al. [20] shows a much better agreement with the HIVAP prediction for the ^{244}Pu(^{22}Ne, 5*n*)^{261}Rf than for the ^{244}Pu(^{22}Ne, 4*n*)^{262}Rf reaction concerning the location of the observed maximum cross section. It was argued that it is most likely that the authors of [42,39,44] might have observed the decay of the newly discovered short-lived ^{261b}Rf, which was unknown at the time of their experiments, and not ^{262}Rf [57]. Therefore, no consistent data on the half-life of ^{262}Rf exist.

Several studies on the isotope ^{263}Rf performed exclusively by chemical means have indicated that this nuclide decays predominantly by SF with a long half-life of 10 – 20 minutes. Alpha particles with an energy 7.8-7.9 MeV have also been associated with this nucleus. The latest evidence for ^{263}Rf as a daughter of ^{263}Db after EC decay was reported by Kratz *et al.* [122] in experiments on Db chemistry giving a half-life value of 24^{+15}_{-7} min. More recently, a study of hassium isotopes allowed the observation of one event of a SF decay from ^{263}Rf as decay chain member of ^{271}Hs with a short half-life of 8^{+40}_{-4} s (error limits correspond to 68% c.i. based on one event). Despite large error bars these two half-life values are significantly different and could be associated with two isomeric states. Specific assignments are difficult due to the low number of observed events. This clearly calls for improved experiments to shed more light on the decay properties of Rf isotopes in the transition region between the N = 152 and the N = 162 neutron shells. The best suited nuclear reactions are ^{248}Cm(^{18}O, xn) and ^{244}Pu(^{22}Ne, xn), both leading to the same compound nucleus ^{266}Rf*. We have studied the latter reaction at the new gas-filled TransActinide Separator and Chemistry Apparatus (TASCA) [123], a recoil separator recently installed at the GSI in Darmstadt.

4.3.1 Experimental setup

A pulsed (5 ms on / 15 ms off) beam of ^{22}Ne^{5+} was produced in the PIG ion source from natural Ne and accelerated by the UNILAC linear accelerator to energies of 114, 121, and 130 MeV with an average beam intensity on the target of $5 \cdot 10^{12}$ ^{22}Ne ions per second. A three-stage differential pumping system separated the vacuum of the beam line from the gas-filled region inside TASCA and hence, no vacuum window was used. The beam then passed through 2.2-μm thick Ti backing foils before entering the ^{244}Pu target material. The targets were prepared by electrochemical deposition from isobutanolic solution, a procedure that yielded the oxide form after annealing. A rotating target wheel with three arc-shaped segments [124] contained three ^{244}Pu targets (isotopic composition: ^{244}Pu: 97.9%; ^{242}Pu: 1.3%; ^{240}Pu: 0.7%; other: < 0.1%) with thicknesses of 476, 525, and 388 μg/cm^2. The target wheel rotated synchronously with the beam macropulse structure.

The beam energies at the center of the targets were 109, 116, and 125 MeV. The energy loss of the beam inside the backing and target material was calculated with

SRIM2006 [125] where the missing data for ^{22}Ne in $^{244}PuO_2$ were extrapolated from data of lighter target materials. The energies in the center of the targets corresponded to excitation energies of the compound nucleus of 41, 47, and 56 MeV [126], corresponding to the maxima of the 4n, 5n, and 6n channel, respectively, as predicted by HIVAP [127]. Reaction products recoiling from the target entered TASCA, a gas-filled separator comprising a *DQQ* magnet configuration, where *D* denotes a dipole and *Q* a quadrupole magnet [88]. Reaction products were spatially separated according to their magnetic rigidity, $B{\cdot}\rho$, in the filling gas. The quadrupoles of TASCA were operated in High Transmission Mode (HTM). In HTM, the first quadrupole focuses in the horizontal direction and the second in the vertical direction.

In pure He gas, EVRs of ^{22}Ne-induced reactions on actinide targets happen to have a $B{\cdot}\rho$ very similar to that of elastically-scattered Target-Like Products (TLP) and therefore, no separation between the two species is possible in pure He. Much better separation between EVRs and TLP can be achieved using hydrogen as a filling gas in the separator. TASCA is designed for $B{\cdot}\rho$ values up to ~ 2.3 T·m, which is not sufficient to bend Rf EVRs from the reaction ^{22}Ne + ^{244}Pu in the pure hydrogen gas. We have therefore investigated whether using He/H_2 mixtures as fill gases would allow a sufficient separation of target-like fragments and EVRs while still leading to EVR magnetic rigidities below 2.3 T·m. As will be described elsewhere [108] the use of such gas mixtures indeed combines the advantages of both gas components.

4.3.1.1 Detection of short-lived ^{260,262}Rf in the focal plane

The identification of short-lived, SF decaying products such as ^{260,262}Rf produced in the *4n* and *6n* exit channels was performed using a focal plane detector. To reduce background from TLP, TASCA was filled with 1.5 mbar of a He:H_2 = 2:1 gas mixture [108]. Even with a mixture of two gases relatively high rates of ~ 80 s^{-1} and 800 s^{-1} from TLP in the whole focal plane detector were observed in the EVR energy ranges of 0.5 to 4 MeV and 0.5 to 10 MeV, respectively, which negatively affected time limits for the search for time- and position-correlated events of the type EVR-SF. A much lower rate of $3{\cdot}10^{-3}$ s^{-1} was measured in the high energy range > 80 MeV. Using a Multi-Wire Proportional gas Chamber (MWPC) in front of the focal plane detector to

distinguish between TLP and SF events is not possible due to the low recoil energy of complete fusion products of this very asymmetric reaction. Also, distinguishing between an EVR and an alpha within a beam pulse was not possible.

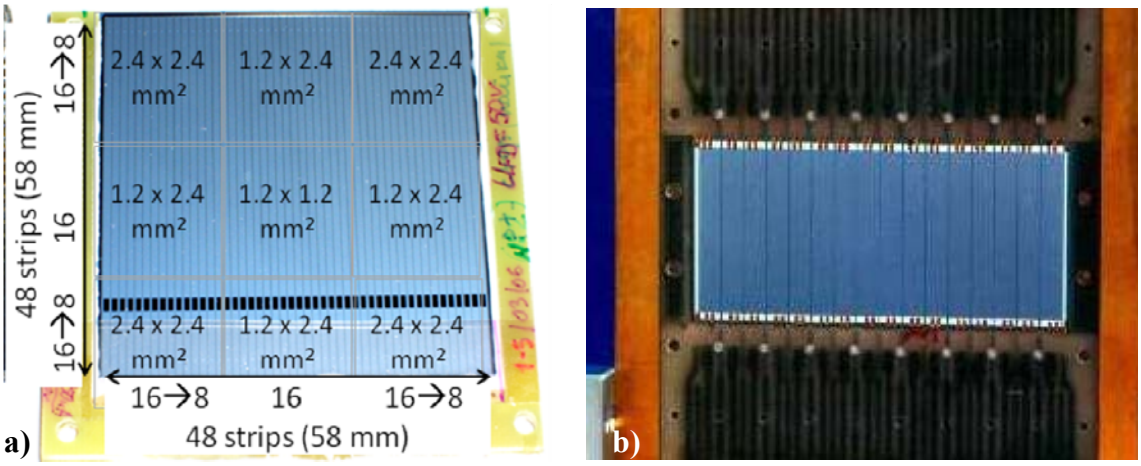

Fig. 4.4: a) The double-sided detector with 48x48 strips (58 x 58 mm^2). The 16 first and the 16 last strips on each side are connected in pairs, b) the 16-strip position sensitive detector (80 x 35 mm^2).

Two types of focal plane detectors were used: a) a 58 x 58 mm^2 48-strip Double-Sided Silicon Strip Detector (DSSSD) made in Zelenograd, Russia and b) a 80 x 35 mm^2 16-strip Position Sensitive Silicon Strip Detector (PSSSD) made by CANBERRA (see Fig. 4.4). Both detectors had a thickness of 300 μm and were operated in fully depleted mode at a bias of 40 and 50 V for the PSSSD and DSSSD, respectively. The DSSSD was operated at ambient temperature and the PSSSD was cooled down to -35 ^{o}C during the measurements. The energy resolution (FWHM) for 5.8 MeV α-particles was about 24 keV for both detectors.

The PSSSD was used for detection of the isotope ^{260}Rf ($T_{1/2}$ = 21 ms) produced in the reaction ^{22}Ne(^{244}Pu,*6n*)^{260}Rf at a center-of-target beam energy ($E_{c.o.t.}$) of 125 MeV. The nominal vertical position resolution of the PSSSD is 0.6 mm, however, a search for position correlated decay chain members occurred within ± 1 mm limits, corresponding to a pixel size area of 5 x 2 mm^2. The relatively large pixel size of the PSSSD did not allow detection of EVR-SF decay chains with a correlation time longer than 300 ms. The DSSSD was used for measurements of ^{262}Rf, as produced in the *4n* exit channel at a beam energy of 109 MeV in the center of the target. This detector had an active area of 58x58 mm^2 divided in 48 strips with a width of 1.2 mm on both, the front (in ***x***) and the back (in ***y***) side. Due to a limitation of the available number of spectrometric channels (64), the first and last 16 strips on each side were connected to 8

spectrometric channels by groups of two (see Fig. 4.4 a)). This resulted in three different pixel sizes over the whole DSSSD: the smallest 1.2 x 1.2 mm^2 in the center of the DSSSD and the largest 2.4 x 2.4 mm^2 in the corners. However, even the largest pixel size in the DSSSD was only half that of the PSSSD. The detection efficiency in both detectors is: i) for an EVR near 100%, ii) for an α particle 50-55%, iii) for a SF fragment 100%. The measurement of both fission fragments in coincidence was not possible, because the implantation detectors only were used without surrounding backward detectors.

4.3.1.2 Preseparation and detection of long-lived ^{261}Rf in ROMA

The measurement of the relatively long lived ^{261a,b}Rf in a focal plane detector of an electromagnetic recoil separator is not an easy task. This neutron-rich isotope can only be produced as an alpha-decay product of heavier nuclides or via reactions of light projectiles with neutron-rich actinide targets, like $^{22}Ne + {}^{244}Pu$ or $^{18}O + {}^{248}Cm$. In these reactions, a high background from TLP and scattered beam ions and the low kinetic energy of complete fusion reactions products do not allow searching for long EVR-α or EVR-SF correlations. To overcome this problem, a combination of physical preseparation and detection after gas jet isolation [128] was applied for measurements of ^{261a,b}Rf. For these studies, TASCA was filled with pure He (pressure 0.4 mbar), as separation from TLP is not as critical in preseparation mode due to the absence of implantation signals and an additional suppression of short-lived activities during the transport time. At the focal plane of TASCA, ^{261a,b}Rf passed through a 1.2-µm thick 140 x 40 mm^2 Mylar window and entered the recoil transfer chamber where they were thermalized in ~ 1.2 bar He. The window separated the 0.4 mbar He in TASCA from the 1.2 bar He in the RTC. The RTC depth was 17 mm. The He gas (flow rate: 3.45 l/min) was seeded with KCl aerosol particles produced by sublimation of KCl at 650 °C. The products were transported through a 4-m long polyethylene capillary (inner diameter: 2 mm) to the Rotating wheel On-line Multidetector Analyzer (ROMA) [129]. The particles were deposited on 40-µg/cm^2 thick polyethylene foils which were mounted on the circumference of an 85-cm diameter large wheel. The wheel was periodically rotated to transport the sample collection position into eight counting positions equipped with pairs of 20 x 10 mm^2 large PIN photodiode detectors suitable

for registering α-particles and fission fragments. For measurements of ^{261a}Rf, a stepping time, t_{step}, of 35 s was used. Search experiments for ^{261b}Rf produced in the *5n* evaporation channel and detected in ROMA were performed with t_{step} = 1.5 s. A photograph of the ROMA setup is shown in Fig. 4.5

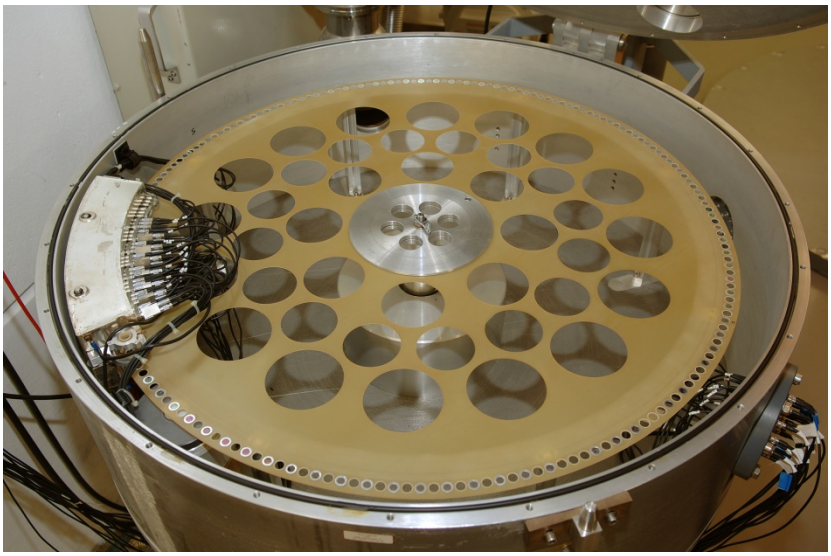

Fig. 4.5: Rotating wheel On-line Multidetector Analyzer (ROMA).

4.3.2 Results and discussion

4.3.2.1 ^{260}Rf

The new measurement of Rf isotopes produced in the *4n*, *5n,* and *6n* evaporation channels of the nuclear reaction ^{244}Pu + ^{22}Ne aids in solving the puzzle about decay modes and half-lives of ^{261}Rf and ^{262}Rf. The *6n* evaporation channel product, ^{260}Rf, is a short-lived SF decaying isotope with a half-life of 21 ± 1 ms [112]. Due to the expected high counting rate from TLP in the focal plane detector measurements with the most short-lived among the studied isotopes, ^{260}Rf, were started that was expected to register with the highest significance also under fairly high-background conditions.

^{260}Rf was produced at $E_{c.o.t.}$ = 125 MeV where the maximum cross section of the 6n channel was expected. The PSSSD was used for this measurement, which took about 30 hours. A search analysis for EVR's [0.5 < E (MeV) < 10, during the beam pulse] followed within Δt ≤ 100 ms by an SF [70 < E (MeV) <200] was performed. The background from scattered beam ions did not allow for SF event identification during

the beam pulse (time interval 0-8 ms), thus, we searched for SF events in the PSSSD during the beam pause (time interval 8-20 ms). 64 SF events were measured, but 7 EVR-SF events only were registered as position correlated chains inside a position window of ± 1.5 mm due to limitations of the electronics. The unambiguous identification of EVR-SF chains with correlation times longer than 200 ms in the PSSSD was not possible due to a high probability for the observation of random correlations. A time analysis resulted in a half-life value of $20.4^{+12.4}_{-5.6}$ ms according to [130] (error limits correspond to a 68% c.i.), which is in good agreement with the value of 21±1 ms published in [112].

4.3.2.2 ^{261a,b}Rf

^{261}Rf was produced in the *5n* channel at $E_{c.o.t.}$ = 116 MeV and was detected in ROMA [129]. Based on knowledge that the isotope ^{261}Rf exists in two isomeric states described in section 4.3, two stepping times were used: 35 s for ^{261a}Rf (run I) and 1.5 s for ^{261b}Rf (run II). The total irradiation time for both runs lasted 105 hours. In the first run, we registered 149 single α-particles (E_α = 7.8 – 8.5 MeV) from ^{261a}Rf and its daughter ^{257}No; among these were 28 α-α correlations. Based on the number of detected single α-particles (^{261a}Rf + ^{257}No) in eight detector pairs a decay curves for ^{261a}Rf ($T_{1/2}$ = 78 s), it's daughter ^{257}No ($T_{1/2}$ = 24.5 s) and the sum of both were plotted (see Fig. 4.6). During the first 35 s collection of activity in the sample and the radiation decay occurred without measurement. The measurement time was 3 times longer than the sum of half-lives of ^{261a}Rf and ^{257}No, thus about 20 decays from ^{261a}Rf and its daughter ^{257}No would be expected after the measurement time interval has passed. The data can be fitted well with a function (equation and solid line in Fig. 4.6) describing the subsequent decay ^{261a}Rf → ^{257}No using half-lives of $T_{1/2}$(^{261a}Rf) = 78 s and $T_{1/2}$(^{257}No) = 24.5 s. This confirms that the detected events are originating from ^{261a}Rf.

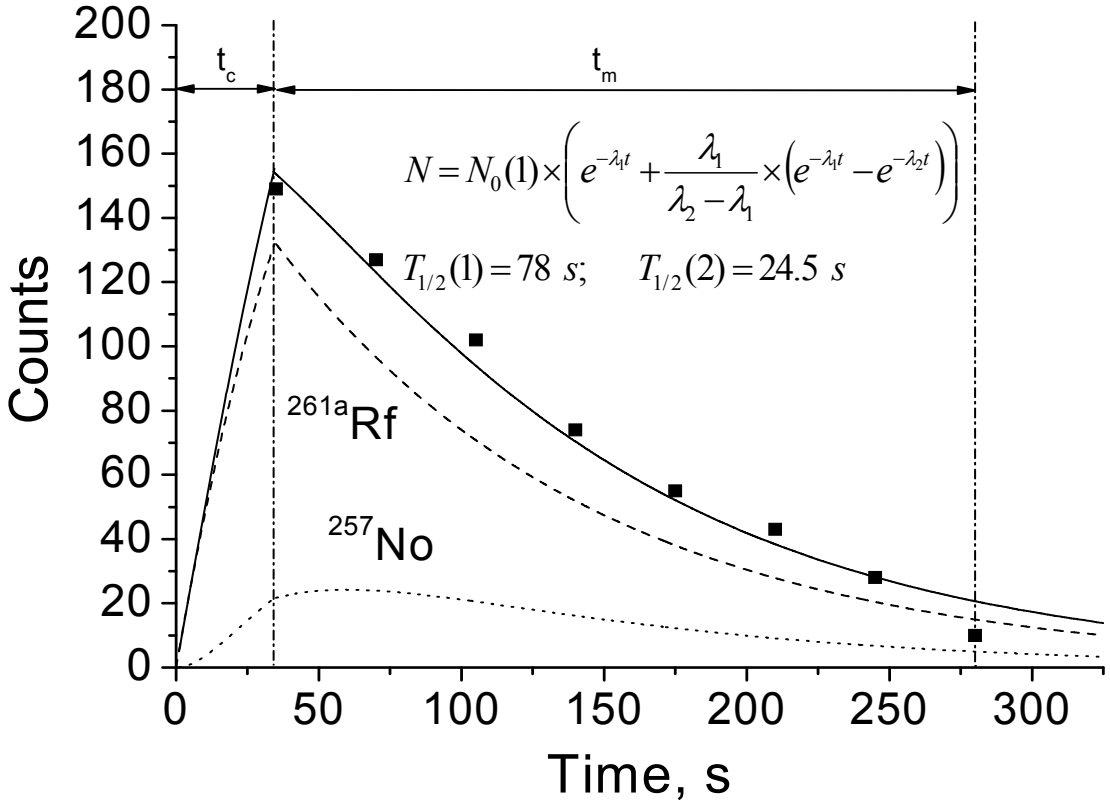

Fig. 4.6: The production and the decay curves for ^{261a}Rf ($T_{1/2}$ = 78 s, dashed line), its daughter ^{257}No ($T_{1/2}$ = 24.5 s, dotted line) and the sum of both (solid line). Symbols represent numbers of surviving ^{261a}Rf + ^{257}No nuclei starting from the beginning of the measurement (t = 35 s). Time intervals t_c and t_m represent the collection time and measurement time, respectively.

The second run was aimed at observation of ^{261b}Rf, produced also as an evaporation residue of the complete fusion reaction and was performed at the same beam energy but with a ROMA stepping time of 1.5 s. Based on the time distribution of 11 registered SF events (Fig. 4.7) and the deduced half-life $T_{1/2} = 2.2^{+1.0}_{-0.5}$ s these events were attributed to ^{261b}Rf produced as an evaporation residue of the complete fusion reaction. Our observation is consistent with the half-life assigned to ^{261b}Rf from previous experiments, where this isotope was detected as the daughter of ^{265}Sg [48, 57] or has been produced directly in a complete fusion reaction and wrongly assigned to ^{262}Rf [42]. No α-particles with an energy around 8.5 MeV have been detected, thus, a SF branch of ≥ 91% was derived, also in agreement with [48].

The study of the ^{22}Ne + ^{244} Pu nuclear reaction at the DGFRS by Lazarev *et al*. [121] resulted in observation of SF activities at two beam energies of 114 and 120 MeV, which are close to the maximum of the *5n* evaporation channel. However, the assignment has been made only for short EVR-SF correlations with a correlation time of

1.4 ms and 26 ms. Longer correlations could not be distinguished due to the low EVR implantation energy, thus the observation of ^{261b}Rf and also ^{262}Rf was not possible.

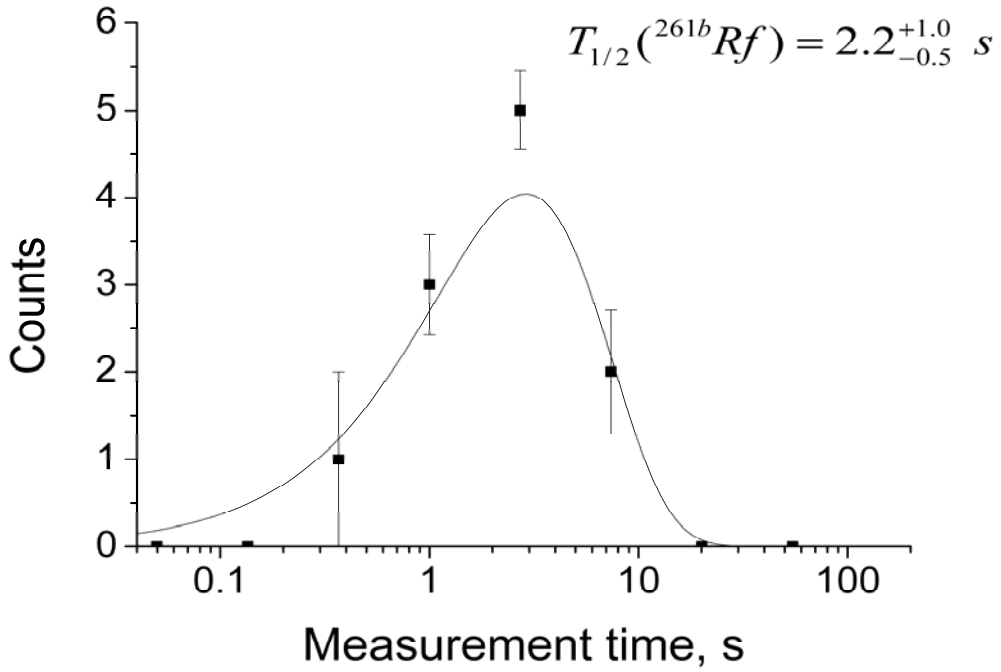

Fig. 4.7: Time distribution of ^{261b}Rf registered in ROMA.

4.3.2.3 ^{262}Rf

As already described in the introduction of section 4.3, no reliable results on the half-life of ^{262}Rf are available, and one of the main goals of this work was to determine the half-life of ^{262}Rf. The measurement of EVR-SF correlations in a focal plane detector of an electromagnetic recoil separator is more preferable compared to other techniques. However, low energies of EVRs from asymmetric reactions and the background from TLP and scattered beam ions significantly affect registering EVR-SF correlations with a correlation time longer than hundreds of milliseconds. ^{262}Rf was produced in the *4n* evaporation channel at $E_{c.o.t.}$ = 109 MeV and measured in the focal plane detector for 27.5 hours. Because the time window for the search of correlated EVR-SF events in the PSSSD was limited to 200 ms only due to the background and the position resolution, the DSSSD was used instead of the PSSSD. The smaller pixel size of the DSSSD allowed increasing the time window of the search time for correlated EVR-SF events up

to 3 s. However, the unambiguous observation of a SF activity with a half-live of 2.1 s assigned in [57] to ^{262}Rf would not be possible.

A search for EVR's [0.5 < E (MeV) < 15 during the beam pulse] followed within $\Delta t \leq 3$ s by an SF [80 < E (MeV) <200] where EVR and SF occurred in the same pixel, revealed 10 EVR-SF events with EVR energies of 1÷3.5 MeV. In addition, 15 EVR-SF events with EVR energies of 4÷15 MeV and a correlation time shorter than 4 ms were observed.

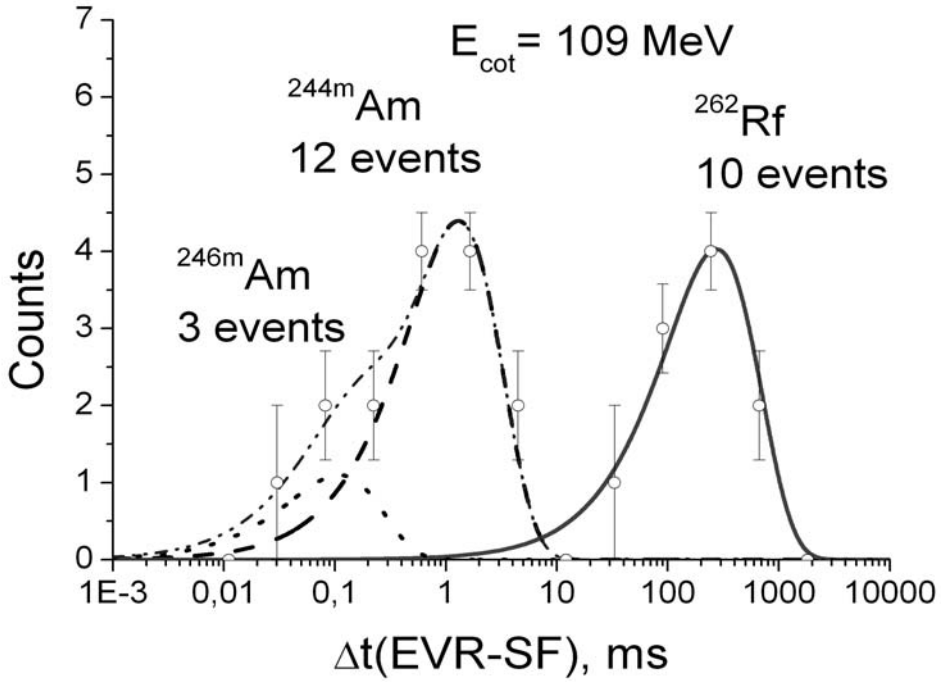

Fig. 4.8: Lifetime distribution of EVR-SF events measured at $E_{c.o.t.}$ = 109 MeV.

The time distribution of all detected EVR-SF events is shown in Fig. 4.8: Two groups of SF events are very clearly separated in lifetime. 10 events with lower EVR energy listed in Table 4.2 were assigned to the isotope ^{262}Rf.

Table 4.2: The detected EVR-SF events from ^{262}Rf.

X strip	Y strip	E_{EVR}, MeV	E_{SF}, MeV	Δt_{EVR-SF}, ms
5	20	2.9	112	223
26	15	3.3	186	78.5
30	26	2.45	181	672.9
31	25	1.8	120	683.9
30	24	1.8	131.5	234.3
30	13	1.37	193	303.7
4	8	1.6	134	114.5
18	19	1.28	112	46.4
1	26	3.27	95	66.3
22	12	1.25	96	295.2

The short lived SF activity was caused most probably by Am fission isomers. They were attributed to decays of ^{244m}Am ($T_{1/2}$ = 0.9 ms [131]) and ^{246m}Am ($T_{1/2}$ = 73 μs [132]). The time analysis of the events listed in Table 4.2 according to [130] resulted in a half-life for ^{262}Rf of 190^{+100}_{-50} ms (Fig. 4.8, solid line), in contradiction to values of 47 ms [112] and 2.1±0.2 s [42]. The measurement in the DSSSD at TASCA allowed clear distinction between EVR-SF correlations from evaporation residues of the complete fusion reaction and Am fission isomers due to significant differences in correlation times and EVR energies. The measured half-life for ^{262}Rf of 190 ms is by factor of 4 longer than the one reported by Somerville *et al*. [112]. Most likely, the SF activity, which has been assigned to ^{262}Rf in [112] was not free from contaminants: fission isomers and/or other short-lived isotopes produced via different channels.

Because of the relatively high counting rate of EVR-like events in the DSSSD, a random event analysis was performed for the detected 190-ms SF activity within a time window of Δt = 1 s. The counting rate depended on the distribution of products in the focal plane and also on the different pixel sizes over the whole DSSSD. The smallest pixel size of 1.2 x 1.2 mm^2 was in the center part of the DSSSD, where the highest counting rate was expected. The random event number, n_b, was calculated individually for each detector pixel. The contour plot of random events over the DSSSD is presented in Fig. 3.9. The background from TLP was higher at lower x strips, where also more

events from Am fission isomers were found. The total random event number in the whole DSSSD is calculated as the sum of n_b over all 1024 pixels and has a value of 0.345. Thus, a random origin for the observed EVR-SF events could be excluded. If the search time is extended to 3 s, one random event is expected. Indeed, we found one EVR-SF correlation within 3 s with a correlation time of 2.6 s. This prohibited the measurement of longer lived ^{261a,b}Rf in the DSSSD.

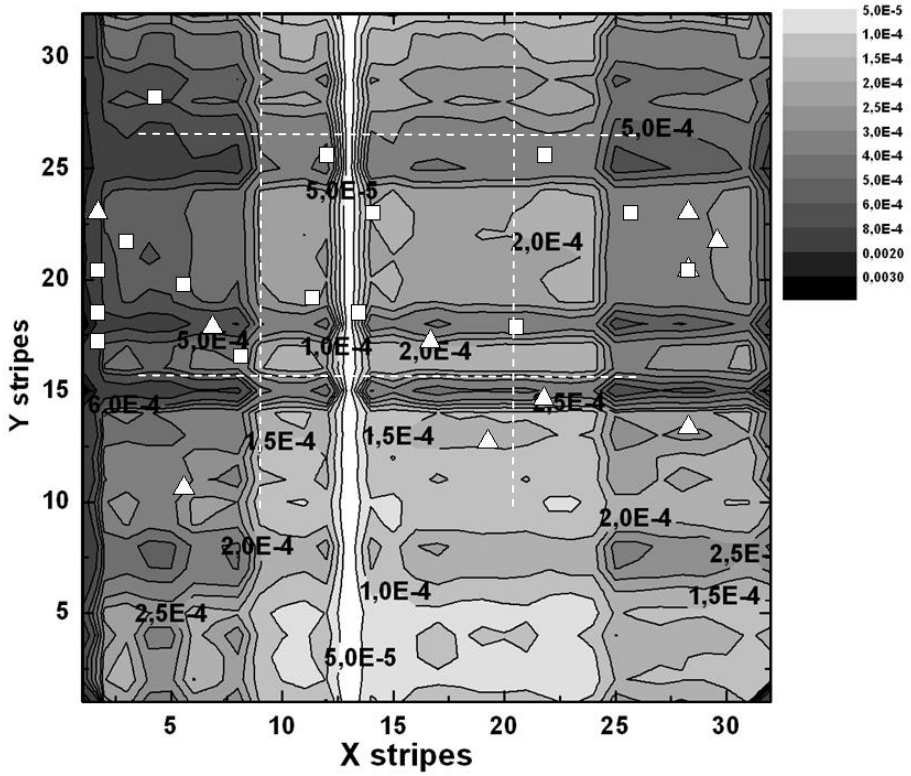

Fig. 4.9: Contour plot of random events over the DSSSD. Positions, where ^{262}Rf and Am fission isomer events were detected are marked with triangles and with squares, respectively. The strip x13 was not working, and strips y15 and y17 had higher noise in at the low energy range.

4.3.2.4 Cross sections

The isotope ^{261}Rf (^{261a}Rf here) has been produced previously in the ^{22}Ne + ^{244}Pu nuclear reaction with a cross section of 4.4 nb at a beam energy of 114 MeV and with a similar cross section of 3.8 nb at a beam energy of 120 MeV [121]. In our experiment we measured products of the *5n* evaporation channels, ^{261a}Rf and ^{261b}Rf at a beam energy of 116 MeV in the center of the target, which is close to the energy reported in [121]. By solving the equation of the subsequent decay ^{261a}Rf → ^{257}No for the

measurement time interval (see Fig. 4.6), it follows that from 149 single α-particles detected in ROMA 107 should be from ^{261a}Rf and 42 from ^{257}No. Taking into account the aerosol transport efficiency of 60%, the RTC grid transparency of 80% and the collection efficiency of Rf EVRs reaching the focal plane into the 140 x 40 mm^2 large exit window of 80%, a number of ^{261a}Rf atoms that reached the TASCA focal plane was calculated as $N_{\text{focal plane}}(^{261a}\text{Rf}) = 358$. The ratio of this number to the calculated number of ^{261a}Rf atoms produced during the 37.5 h irradiation, $N_{\text{produced}}(^{261a}\text{Rf}) = 3377$, yields a transmission efficiency through TASCA for Rf nuclei produced with the ^{22}Ne beam of 10.5%, in case the cross section of 4.4 nb from [121] is used. This value is in a good agreement with a value of 10% estimated with a Monte Carlo model developed by Gregorich for the BGS separator and adapted for TASCA by Semchenkov *et al*. [89,91]. For the second state, ^{261b}Rf produced at the same beam energy, a cross section of $1.8^{+0.8}_{-0.4}$ nb was calculated, assuming decay losses during the transport (~2.5 s) from the exit of TASCA to the detection device of 50% and an aerosol transport efficiency of 60%. The production ratio of ^{261a}Rf to ^{261b}Rf measured in this work is about 2.5:1, thus, the total production cross section of the *5n* evaporation channel of the reaction ^{244}Pu + ^{22}Ne is about 40% higher than it was reported earlier in [121]. Assuming that the activity assigned to ^{262}Rf by Lane *et al.* in [42] was actually due to the decay of ^{261b}Rf, its production cross-section in the same nuclear reaction, ^{22}Ne + ^{244}Pu at a beam energy in the center of the target of 114 MeV, was also more than two times lower than in our experiment.

The focal plane detectors used in our experiments were smaller in area than the TASCA exit window. Using the distribution of EVRs in the TASCA focal plane from Monte Carlo simulations, transmissions of 5.1% and 5.3% were calculated for the PSSSD and DSSSD, respectively. These values were used for the production cross section calculations for ^{260}Rf and ^{262}Rf. The products of the *6n* evaporation channel, ^{260}Rf, and in the *4n* evaporation channel, ^{262}Rf, were produced with production cross sections of $1.5^{+0.5}_{-0.3}$ nb and $4^{+0.8}_{-0.6}$ nb at energies in the center of the target of 125 and 109 MeV, respectively. However, the cross section value for ^{260}Rf can be lower if some of the registered SF events originate from interfering transfer reaction products. Calculations made with the statistical model code HIVAP developed at GSI with the parameter set from [127] predict maximum production cross sections for the *4n, 5n,* and *6n* evaporation channels of 0.75 nb, 2.5 nb, and 0.55 nb, respectively (see Fig.

4.10). The calculated values for the *4n* and *5n* evaporation channel are by a factor of ~ 2 lower than observed in this work.

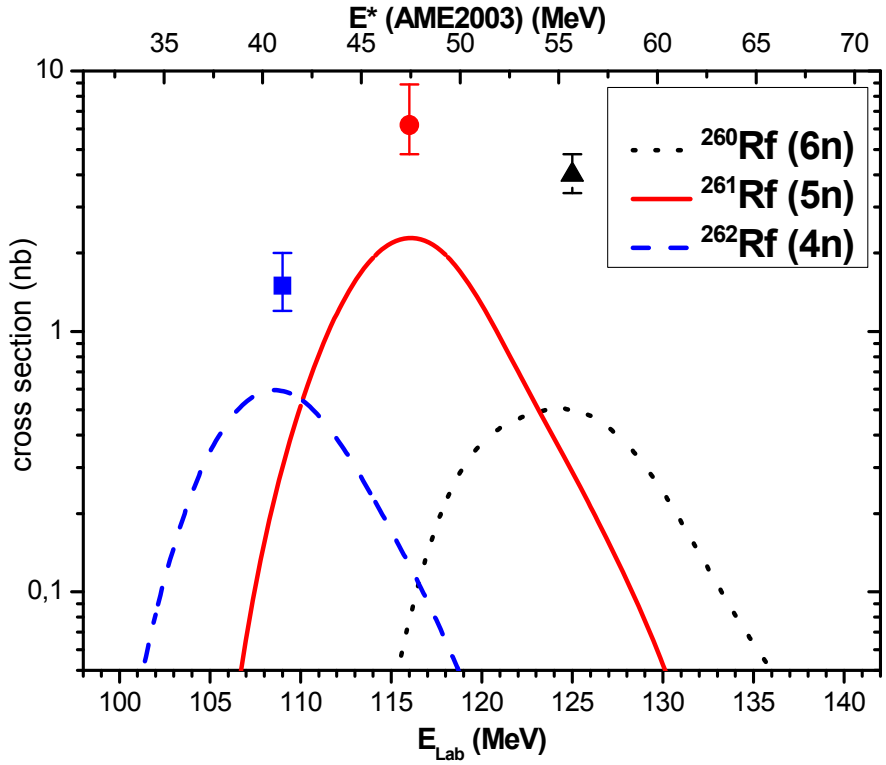

Fig. 4.10: Calculated with HIVAP [127] excitation function of the reaction ^{244}Pu(^{22}Ne, *4-6n*)$^{260-262}$Rf (lines), and experimental production cross section values for ^{260}Rf at $E_{c.o.t.}$ = 125 MeV (square), ^{261}Rf at $E_{c.o.t.}$ = 116 MeV (circle), and ^{262}Rf at $E_{c.o.t.}$ = 109 MeV (triangle) (this work).

The measurements of SF decaying ^{260}Rf and ^{262}Rf in the TASCA focal plane detector have demonstrated the advantage of the DSSSD over the PSSSD due to the smaller pixel size and absolute position determination.

Chapter V
New TASCA detection system

New focal plane detector array and electronics

5.1 Design of the new FPD setup for TASCA

Taking into account the results from the TASCA commissioning experiments described in the previous Chapter and the experience of other groups in this field, the TASCA FPD working group has decided to build a new focal plane detector setup based on a DSSSD as a stop detector, which provides better position resolution due to smaller pixel size. A backward array and a *veto* detector behind the stop detector should consist of single-sided silicon strip detectors (SSSSD).

The new setup must accept most of the separated recoils, which are guided to the focal plane when TASCA is operating in the HTM within an image size of ~ (140 x 40) mm^2. The use of backward detectors surrounding the implantation detector increases the detection efficiency of α-particles and SF fragments emitted from nuclei implanted in the stop detector and allows the measurement of conversion electrons. This increases the efficiency for the detection of α-particles from ~ 55% to ~ 70% depending on the geometry (see Table 5.1) using summing techniques and reduces the background in the low-energy region of the spectrum.

As a compromise between small pixel size and low number of spectrometric electronic channels, a pitch width of 1 mm on the front and back side of the DSSSD has been chosen. The number of strips on each side of the DSSSD and on the SSSSD should be proportional to 8 to reduce the number of spectrometric modules. A 32-channel preamplifier and a 8-channel amplifier with an integrated multiplexer were developed for the TASCA focal plane detector in cooperation with ERIKON (Dubna, Russia). The multiplexers were implemented into 8-channel amplifier modules to reduce the necessary number of ADCs.

All PSSSD and DSSSD detectors available on the market were analyzed and two types were chosen for comparison, a 60x40 mm^2 DSSSD and a 60x60 mm^2 PSSSD from Canberra™ (see Table 5.1). Using two of them, the stop detector would cover an

area of 120 x 40 mm^2 or 120 x 60 mm^2, which is still not large enough to cover the whole EVR distribution in the TASCA focal plane.

Table 5.1: Choice of the components for the TASCA focal plane detection setup.

Implantation detector	Backwards array	Total number of channels	Geometrical efficiency, %
120 x 40	**Depth 60 mm**		
DSSSD 60 x 40 (Canberra) 2 det.	Canberra 60 x 60 6 det. 16-strips	296	72.1
	Canberra 60 x 60 4 det. + Micron 60 x 40 2 det.	278	72.1
120 x 60	**Depth 60 mm**		
PSSSD 60 x 60 (Canberra) 2 det.	Canberra 60 x 60 6 det. 16-strips	192	69.9
144 x 48	**Depth 72 mm**		
DSSSD 72 x 48 (Warsaw) 2 det.	SSSSD 72 x 48 8 det. 16-strips 8-strips	368 304	72.1

The development and production of new detectors of custom size, which allow collecting almost 100% of the separated nuclei in the focal plane, and in addition, would be less expensive than detectors available on the market was one of the main goals of our project that was very important due to strict money limitations. The detector chip size for the SSSSD and the active size area for the DSSSD have been fixed as 72 x 48 mm^2, taking into account the selected pitch width and the number of strips proportional to 8. The production of the detector structures of similar size is well established and detectors are not as expensive because they can be produced from 4 inch silicon wafers. The DSSSD and SSSSD detectors have to be designed, manufactured and tested, as well as the construction of the whole detector setup. The design of the detector masks for both SSSSD and DSSSD, production of the new detectors and their quality control have been performed at the Institute of Electronic Technology in Warsaw, Poland in the framework of a long-term cooperation program. In general, DSSSDs with a relative narrow pitch size (1 mm) need more spectrometric channels than PSSSDs of similar area. The first two detection setups from Table 5.1 based on PSSSD that are even larger

in area need about 100 channels less, even if 3 spectrometric channels are connected with one PSSSD strip for better position measurement. The new detector setup of custom size of 144 x 48 mm^2 has the same efficiency for the detection of αparticles emitted from implanted nuclei; however, it has the largest number of spectrometric channels.

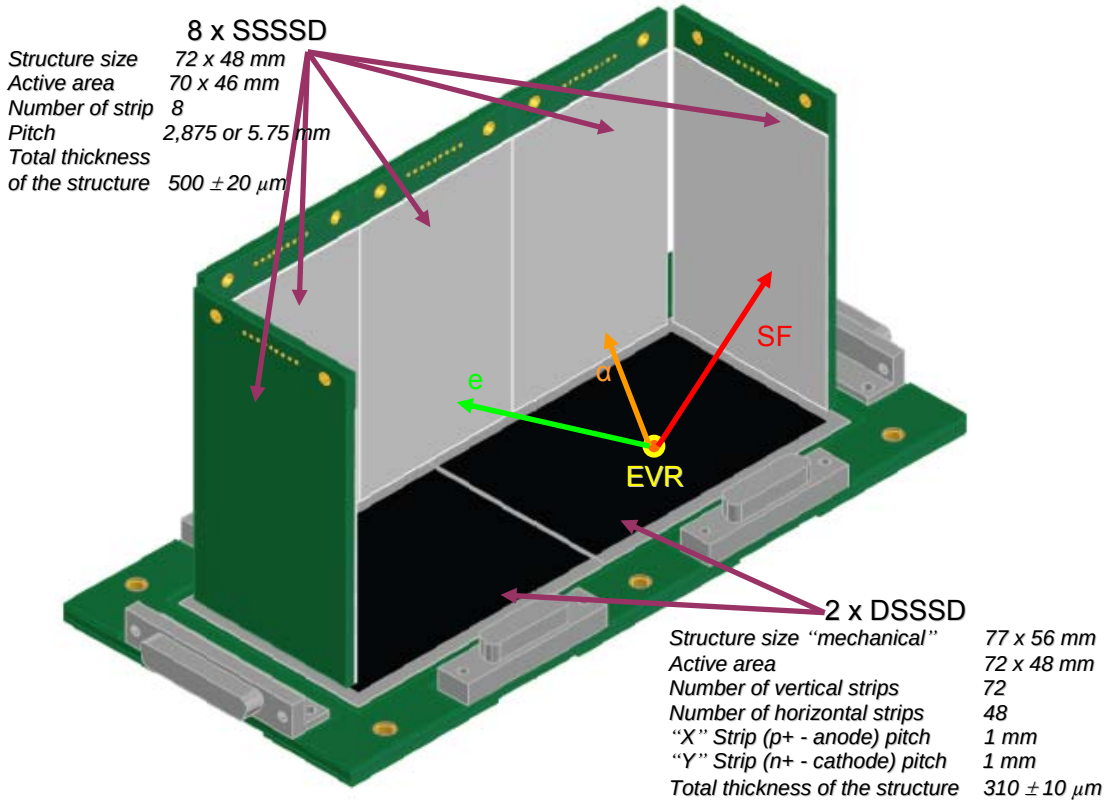

Fig. 5.1: Backward detectors are perpendicular to the strips and protrude roughly from the edges. Veto detectors (not visible) are mounted behind and parallel to the strips.

The principal design of the new detector setup as well as all tests of the manufactured DSSSDs and SSSSDs have been performed in the framework of this PhD work. The principal 3D CAD model of the designed detector setup without supporting metal construction is shown in Fig. 5.1. The Focal Plane Detector Box (FPDB) consists of two DSSSD detectors with an active area of 72 x 48 mm^2 and ten SSSSD detectors with a chip structure size of 72 x 48 mm^2. 8 SSSSDs form an open box and are mounted as close as possible to each other and to the implantation detector.

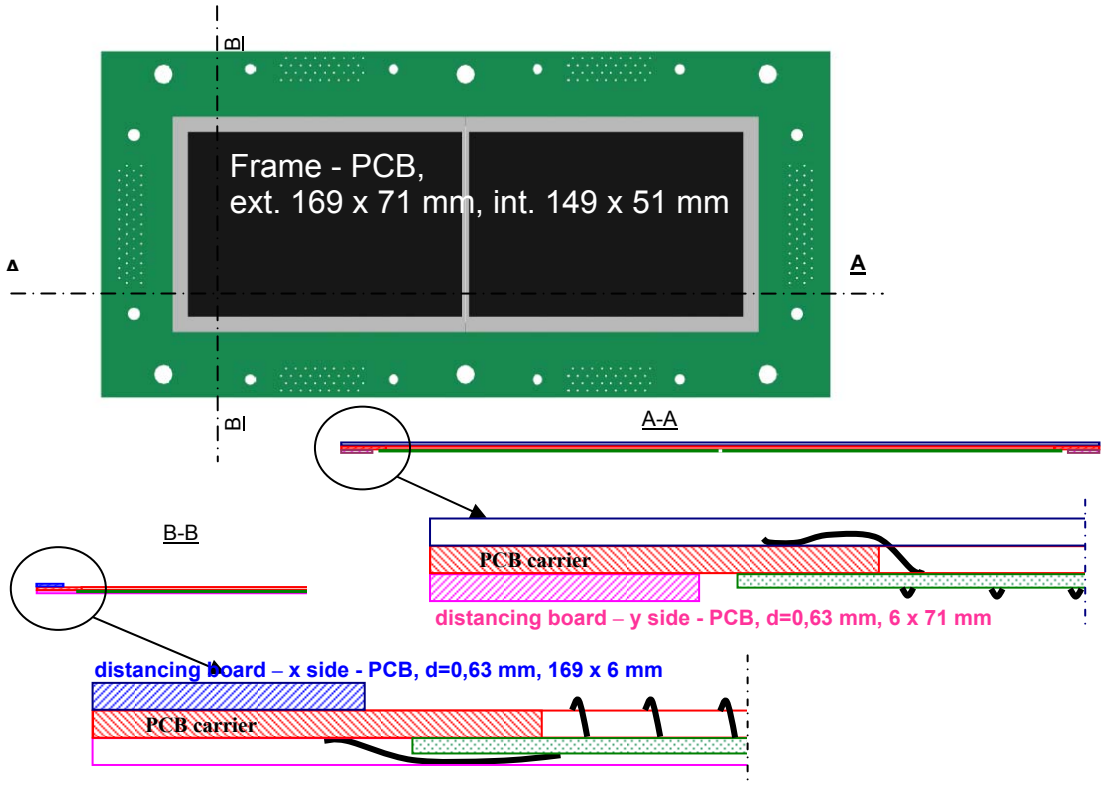

Fig. 5.2: Implantation detector frame and wire bonding.

The most important part of the FPDB is the implantation detector perpendicular to the trajectory of incoming EVRs. This detector must provide very good detection efficiency for implanted reaction products transmitted through the recoil separator to the focal plane, as well as a very good energy and position resolution. In our FPDB the implantation detector consists of two silicon structures with a thickness of 300 μm and a size of 77 x 56 mm^2 made of n-type silicon. Both structures have an active area of 72 × 48 mm^2, comprising 72 vertical strips on the front face and 48 horizontal strips on the back side with a pitch of 1 mm. On the entrance face of the detector (junction side), the 900 μm wide strips are obtained by p^+ implantation of 600 nm thickness. The boron (p^+ implantation) and phosphorus (n^+ implantation) atoms were implanted into the silicon material by thermal diffusion. The p-junction areas are covered by aluminium layers and are isolated by 100 μm wide silicon dioxide layers grown during the passivation step of the process (thickness 650 - 700 nm). The charges are collected from both faces of the detector through a 400 nm thick aluminium metallization deposited on the strips and 25 μm Al wires. On the rare face (ohmic side) the 500 μm wide Al electrodes are

evaporated on the 2000 - 2500 nm thick n^+ implantation zones, which are separated by p^+ type implantation zones.

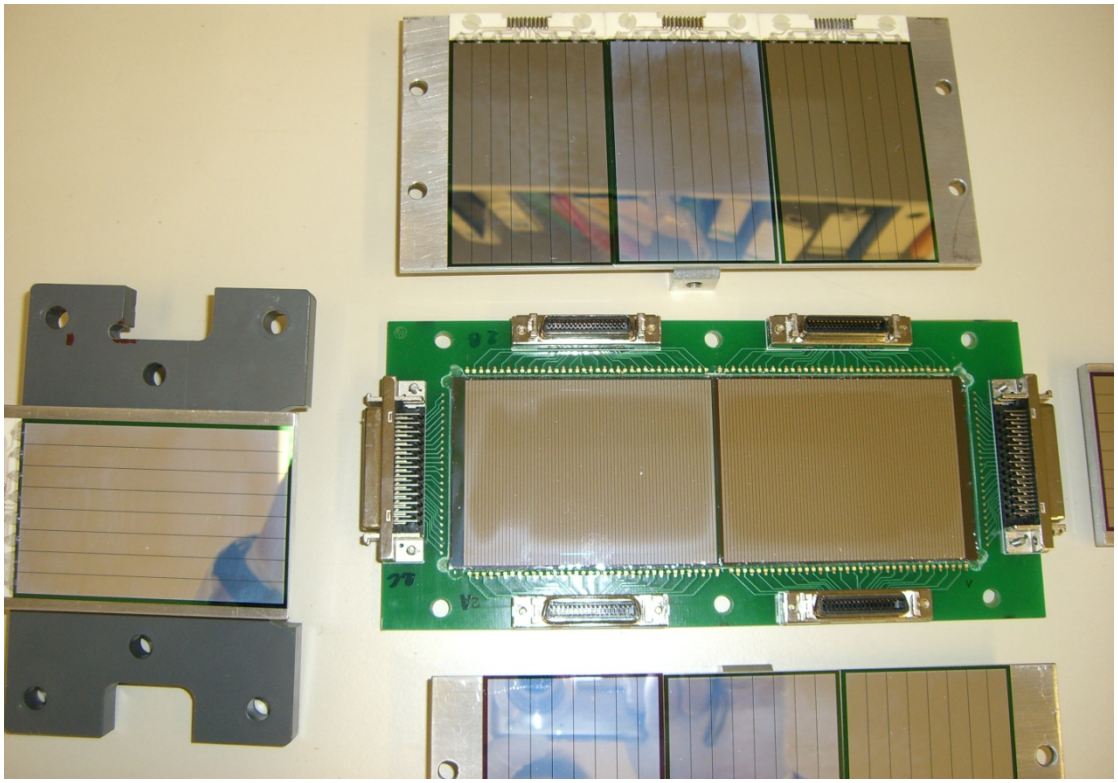

Fig. 5.3: Implantation detector frame with DSSSDs and backward SSSSD detectors.

Two DSSSD structures are mounted side-by-side on the common PCB frame with 6 multi-pin connectors. The opening in the frame is larger than the active area of the implantation detector and allows detection of fast light particles passing through into the veto detector. The active areas of the two DSSSDs are separated by a gap of 4 mm (see Fig. 5.2). Front strips are numbered from 0 at the high magnetic rigidity end to 143 on the low magnetic rigidity end of the focal plane. Each DSSSD structure is connected to three connectors. Signals are produced from both the front and the back strips of the detector when an EVR implantation or radioactive decay occurs, allowing the position determination in both directions with a resolution of 1 mm. The strips of the detectors on the two faces are orthogonal, providing effectively 6912 individual detector position elements within which the time of correlated events consisting of an ion implantation and radioactive decays can be searched for. The 72 front strips are divided between two 36 pin connectors on the top and the bottom of the PCB board in such a way that all odd strips are connected to the top connector and all even strips to the bottom connector (see

Fig. 5.3). because of the use of analogue amplifiers with multiplexers. If two neighboring strips collect the charge from a decay which occurred in between strips or on the border of one, the signals must be processed in different amplifiers. Otherwise, only one signal from one strip connected to a lower input number of an amplifier can pass through the multiplexer. A more detailed explanation can be found in Section 5.3. All 48 back strips of one DSSSD structure are connected to the 50 pin connector. The signals from neighboring odd and even strips are also provided to different amplifiers. SHE EVRs are implanted to a narrow depth (<10 μm), and the geometric probability to detect α particles emitted from implanted EVRs with full energy in the implantation detector is ~ 55%. The DSSSD structures become fully depleted at −20 V. To increase the collection field the strips are biased at −40 to - 50 V.

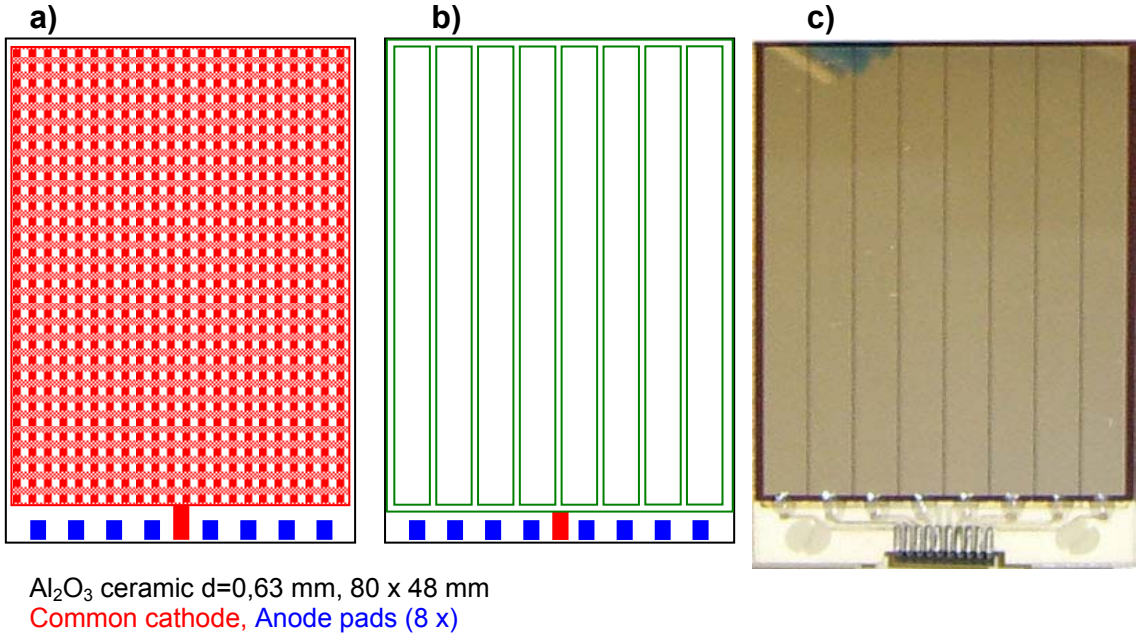

Fig. 5.4: SSSSD detector: a) Al_2O_3 ceramic plate with common contact, b) schematic view of the SSSSD detector and c) photo of the finished device.

Eight "upstream" 8-strip detector structures are mounted perpendicular to the DSSSD detectors forming an open box with dimensions 144 mm x 48 mm x 72 mm. The gap between the implantation detector and the side detectors is about ~ 3 mm. The SSSSD dimensions allow mounting three SSSSD detectors along the long side of the implantation detector and one along the short side; thus, eight detectors together with the implantation detector form a five-sided box configuration (Fig. 5.1). These upstream detectors provide additional detection efficiency of ~ 25 % for alpha particles and fission fragments emitted from implanted nuclei and serve for the detection of

conversion electrons. The SSSSD structures are made from 500-μm n-type Si wafers and are divided in 8 strips 72 mm long and 5.75 mm wide. The gap between the wide SSSSD strips is also 100 μm, similar to the DSSSD. The thickness of 500 μm allows the detection of conversion electrons in the energy range up to 450 keV with high efficiency in future spectroscopy experiments. The parameters of implantation zones and metallization thicknesses for SSSSDs are similar to that of DSSSDs (except 1500 nm thick Al metallization on the back side of SSSSDs). Each SSSSD structure is glued to an Al_2O_3 circuit board and the strips are connected to the multi-pin connectors by Al wires (see Figure 5.4). The Al_2O_3 boards with the SSSSDs are mounted on the support construction made from an Al alloy, which can be cooled for better energy resolution. The SSSSD detectors are fully depleted at −40 V and were biased in the experiment at −40to -60 V.

Particles with ranges in silicon greater than the thickness of the DSSSD detector pass through the DSSSD and generate signals from two Veto detectors mounted behind the DSSSD. These particles are typically protons or alpha particles which can be the result of transfer reactions in the target material, elastic scattering of the beam of the He filling gas, or scattered products of nuclear reactions in the beam stop. These signals in anti-coincidence with signals from the DSSSDs provide cleaning up of the spectra from light, low-ionizing particles which may increase the background in the alpha particle range.

The whole FPDB setup offers the possibility to be cooled to obtain optimum energy resolution and to suppress the effects of radiation damage in the silicon. The silicon detectors need only be cooled to modest temperatures (around –20 °C) which can be conveniently achieved using re-circulating coolant refrigeration systems. Possible materials for the metal construction as brass or aluminum alloy were considered, taking into account a reasonable mechanical stability and good thermal conductivity. The calculated weight of the construction made from brass (without screws) is close to 3.5 kg, while that made from aluminum alloy has 1.5 kg only, while both materials have similar thermal conductivity. Based on this consideration, the complete metal mounting construction, except for the cooling frame with a cooling tube, was made from Al alloy. The upper frame and the soldered on cooling tube were made from copper and then covered with a galvanic nickel layer. The nickel coverage layer is required to prevent electro corrosion between the aluminum-copper galvanic

pair, if water vapors would condense after cooling. In the TASCA detector chamber only one position at the focal plane with a flange of 150 mm in diameter was available for the installation of the new detector setup. The design drawing and a photograph of the whole detector setup ready for mounting into the detector chamber is presented in Fig. 5.5. The metal support construction of the FPDB and the mounting flange are separated by a PVC plate for thermal- and electrical insulation of the detector setup from the detector chamber and for noise suppression.

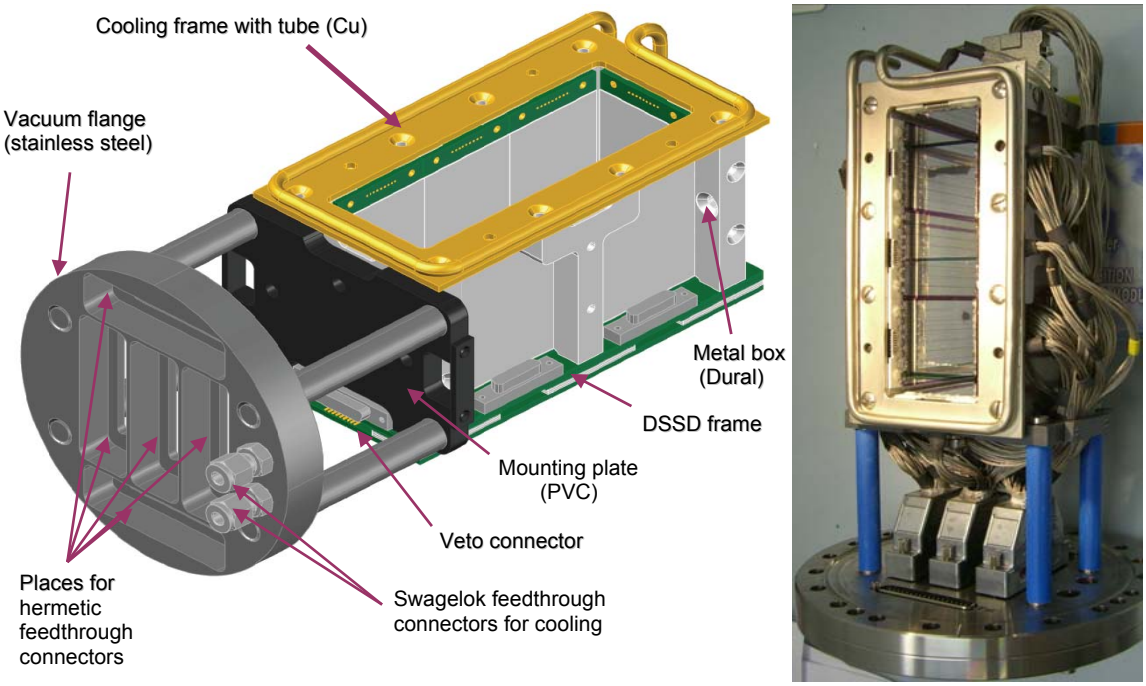

Fig. 5.5. The new focal plane detector setup. On the left-hand side: 3D model of the complete FPDB with its mounting flange On the right-hand side: Photograph of the finished device. In an actual experiment, the whole focal plane assembly reaches into the detector box by the right 150 mm conflate flange.

The new TASCA detector setup was installed in the already available vacuum chamber, which is connected to the exit of the quadrupole vacuum chamber. The flange, on which the FPDB was mounted, was used also for providing all of the required detector outputs and coolant through-feeds. In total there are 320 signal outputs from the implantation detector, backward detector array, and punch-through detector that must go out through the vacuum chamber wall. For this purpose we use three Savac104 (Positronic Industries Inc.) through-feeds with 104 pins each and two Xavac50 connectors with 50 pins each. That gives a possibility to provide up to 412 electrical through-feeds, which also leaves room for a detection system improvement in the

future. The 6-mm Swagelok™ fittings made from stainless steel were used for the connection of the FPDB to the cooling circuit.

5.2 DSSSD and SSSSD tests

An experimental arrangement was prepared for the test of detector prototypes and for measurement of the energy resolution and the detection efficiency of the new TASCA FPDB detectors. For the efficiency measurements, a collimator and an additional 10-μm thick Si photodiode with an active area 10 x 10 mm^2 were positioned (ΔE detector) in front of a detector to be tested (Fig. 5.6).

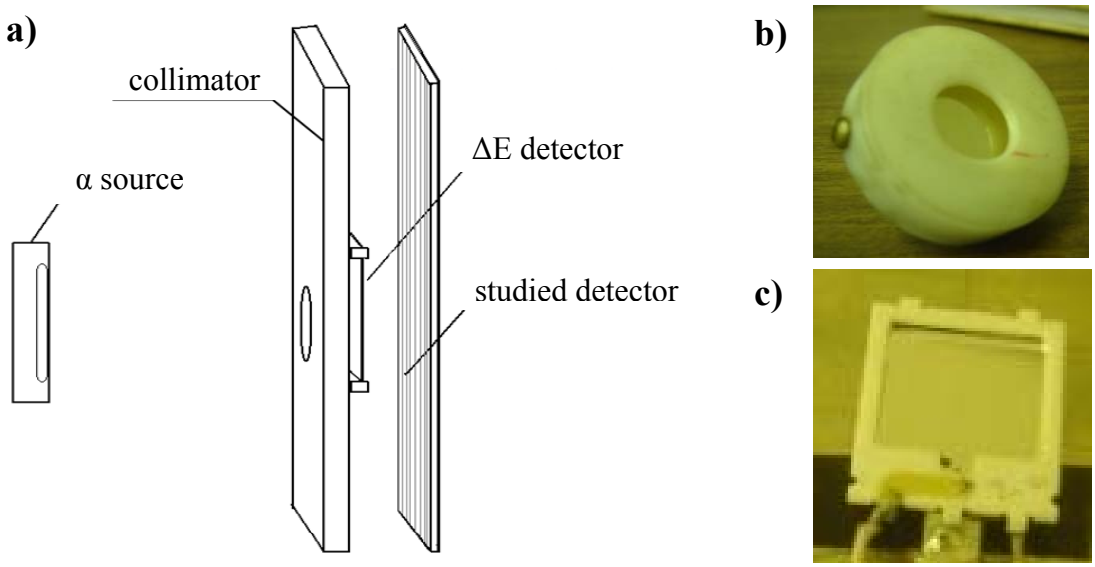

Fig. 5.6. Schematic view of test stand (a), ^{238}Pu α-source (b) and 10 μm thick ΔE detector (c).

During all tests of DSSSD and SSSSD detectors a ^{238}Pu α-source was used wihich has two lines of 5.499 MeV (72% intensity) and 5.456 MeV (28% intensity), which are close to each other and very useful for a measurement of the energy resolution. The thin Si detector was used as a reference detector counting all alpha particles impinging on the test detectors. The alpha particles from the alpha particle source were collimated by a stainless steel collimator of 300 μm thickness with a hole of 7 mm in diameter to prevent scattering at the ΔE-detector frame and the influence of heterogeneity at the borders of the photodiode. The distance between the source and the collimator was about 20 mm.

The tests with the ΔE-detector were aimed at measuring the detection efficiency and to study the charge division process in the interstrip regions. Also the interdependence of the neighboring strips, which can be quite strong, was checked during the tests. For these studies a DSSSD structure was irradiated by alpha particles from the front side, and the shape of the signals was measured directly after the preamplifier with an oscilloscope HP54720D. The main spectroscopy amplifiers have differentiation and integration stages, thus, cross talking studies are not possible after the shaping in the main amplifier. A typical signal shape from the preamplifier output obtained from a single strip is shown in Fig. 5.7. It was found, that almost all implantation signals generate pulses with inverted polarity in the two neighboring strips. This DSSSD structure phenomenon gives information about what kind of amplifiers must be used. Detailed information will be provided in Section 5.3.

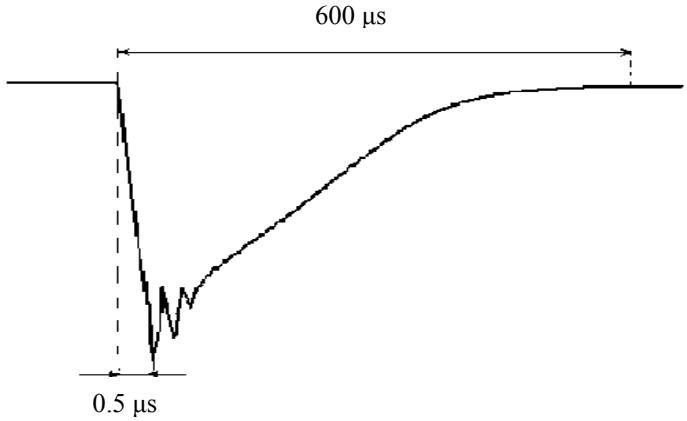

Fig. 5.7. Typical form of the signal from the tested DSSSD detector.

The measured detection efficiency of the new DSSSD detector is about 90% and of the SSSSD detectors is 98%, which is in good agreement with the calculated geometrical efficiency of the detectors. The measured energy resolution with a ^{238}Pu α-source is 20 keV for both DSSSD and SSSSD detectors. This value is limited by the self-resolution of the α-source.

Because of plans to use SSSSD detectors as β-particle detector, they were tested with a ^{133}Ba conversion-electron source. The measured energy resolution is about 9 keV for the line at 322 keV (Fig. 5.8).

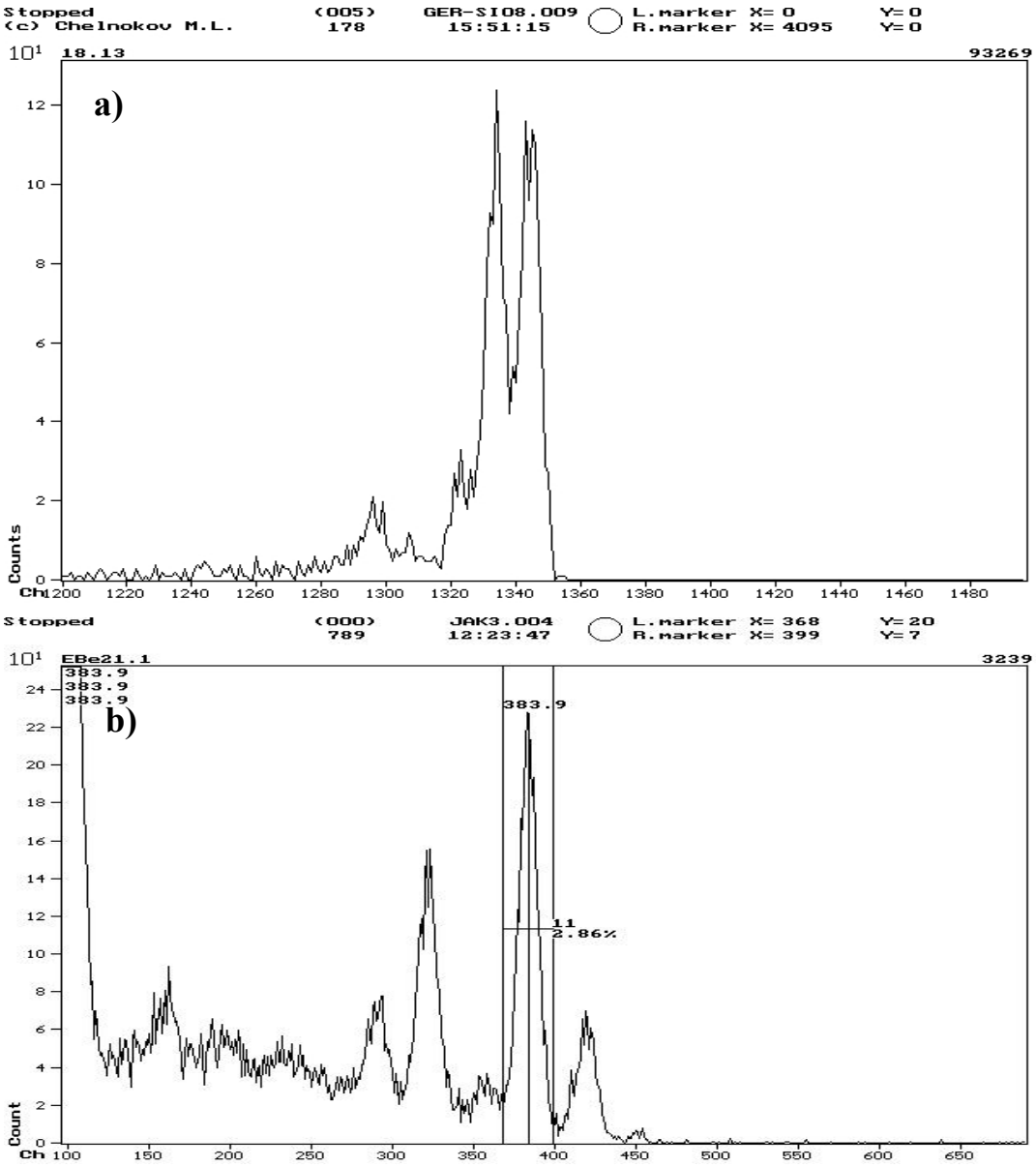

Fig. 5.8. a) ^{238}Pu α-source measured with a DSSSD and b) ^{133}Ba conversion-electron source measured with a SSSSD (x scales are in channels).

5.3 New data acquisition system

The creation of a highly-efficient FPDB with the most compact support structure was only one fraction of the complete TASCA detection system which is needed for a real experiment on the synthesis of SHE. In total, 640 spectrometric channels (320 for the α-particle branch and 320 for the SF branch) are required to readout the new FPDB (Fig. 5.9). The use of conventional electronic modules available on the market was discarded due to strong financial limitations. A new concept of combining analogue electronics and digital electronics has been elaborated in collaboration with Erikon Ltd, Russia. The analogue part of the spectrometric electronics was developed, built and tested by the Erikon Ltd. The new electronics for the TASCA FPDB is described in detail below.

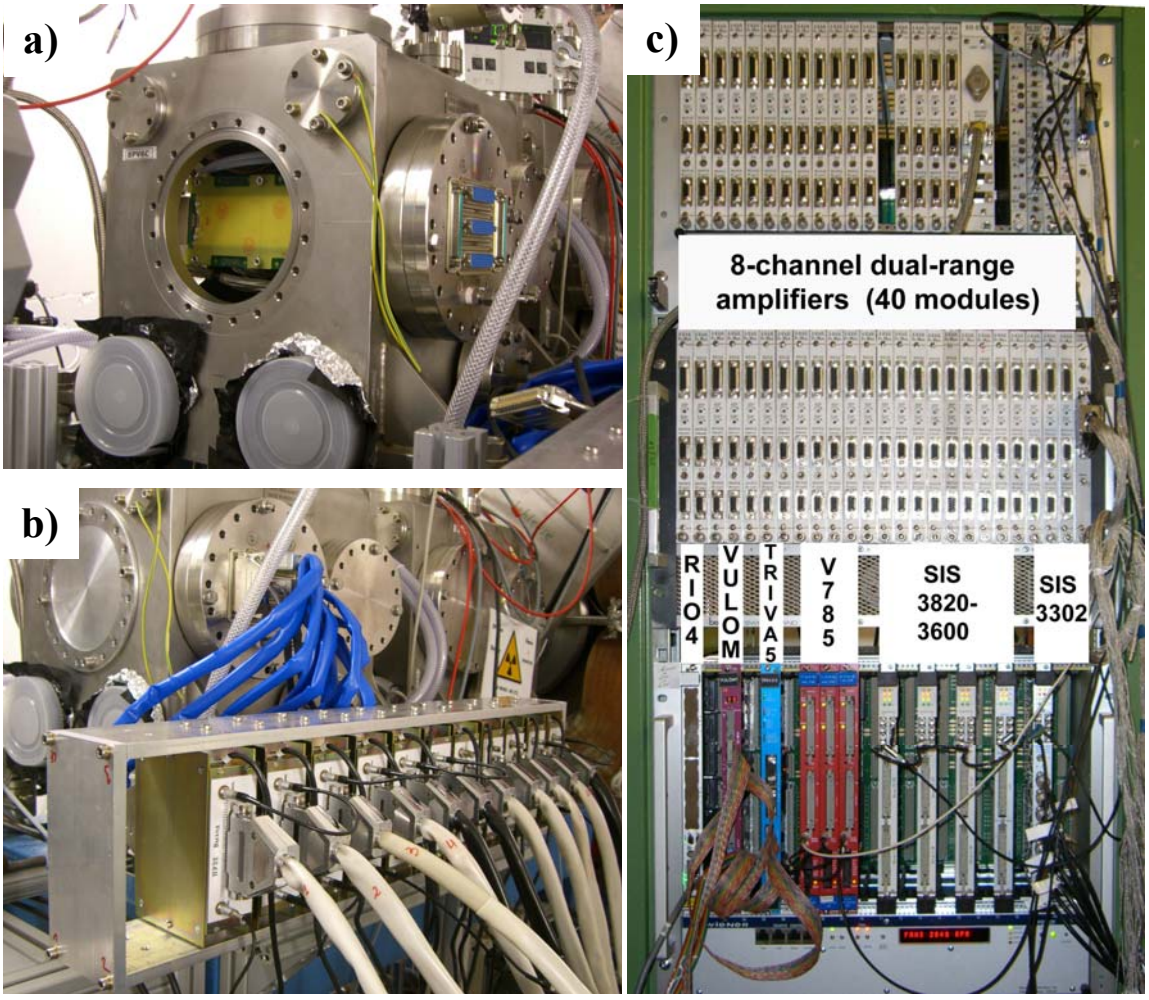

Fig. 5.9: The new TASCA detection setup: a) TASCA detector chamber with installed FPDB, b) 32-channel charge sensitive preamplifiers and c) the electronics rack with main amplifiers and digital VME electronics without connecting cables.

The initial signals produced in the DSSSD and SSSSD detectors are transmitted through coaxial cables to the ten 32-channel charge sensitive preamplifiers. The coaxial cable length is about 30 cm from the FPDB to the flange with through-feeds and 50 cm between the detector chamber flange and the preamplifiers. The spectrometric preamplifiers have a very good signal-to-noise ratio, which is necessary for a good energy resolution. The pre-amplified signals come into the spectrometric amplifiers via 2-m long coaxial cables connecting the outputs of the 32-channel preamplifiers with the inputs of the 8-channel spectrometric amplifiers. Each preamplifier is connected to four 8-channel amplifiers with dual energy range: i) $\times 10$ for α-particles and ii) $\times 1$ for fission fragments. To minimize the total number of ADC channels, two analogue 8-channel multiplexers were integrated into an amplifier for both energy ranges. Each amplifier has the following outputs signals: two analogue signals with a maximum amplitude of ~6 V for two amplification ranges, a 3-bit digital address code of a fired input channel (TTL) and a trigger output (TTL). The multiplexer opens a gate for one fired input only, also if several signals above a threshold from several inputs come into the multiplexer simultaneously. Only the highest-order or lowest-order channel depending on the type of multiplexer will go through and generate an address code; all others will be rejected. Because of the possible charge division process in the interstrip gaps, even and odd neighboring strips were connected to different amplifiers. Such a connection opens the opportunity to reconstruct events from two adjacent strips if charge division occurs.

A schematic of the TASCA analogue electronics is presented in Fig. 5.10. In the first amplification cascade of the amplifier, the signals from the preamplifier are differentiated and amplified by factor of ~ 3. At this point a fine amplification gain (Gain 1) can be adjusted for each channel individually. The signals are split in two after the first amplification cascade – the first one goes to integration and further amplification cascades; the second one is amplified in the fast amplifier by factor of ~10 and provides the logical signal if it is greater than the threshold adjusted with the low level discriminator. The first analog signal that passed two integration stages is amplified in the second cascade. At this point a coarse amplification gain (Gain 2) can be adjusted. The amplified signal in the second cascade is again split in two. One is defined as "*SF"* output and goes directly to a (SF)-multiplexer. This output serves for detecting signals with high amplitudes, such as from fission fragments. The other one defined as "*Alpha"* is amplified by factor of ~10 and goes to the second (α)-multiplexer.

In total 40 analog output signals from the α-particle branch and 40 from the SF branch are connected to inputs of three 32-channel peak sensing ADCs V785 (CAEN). The shaping time in the amplifier is fixed and has a value of 2 μs.

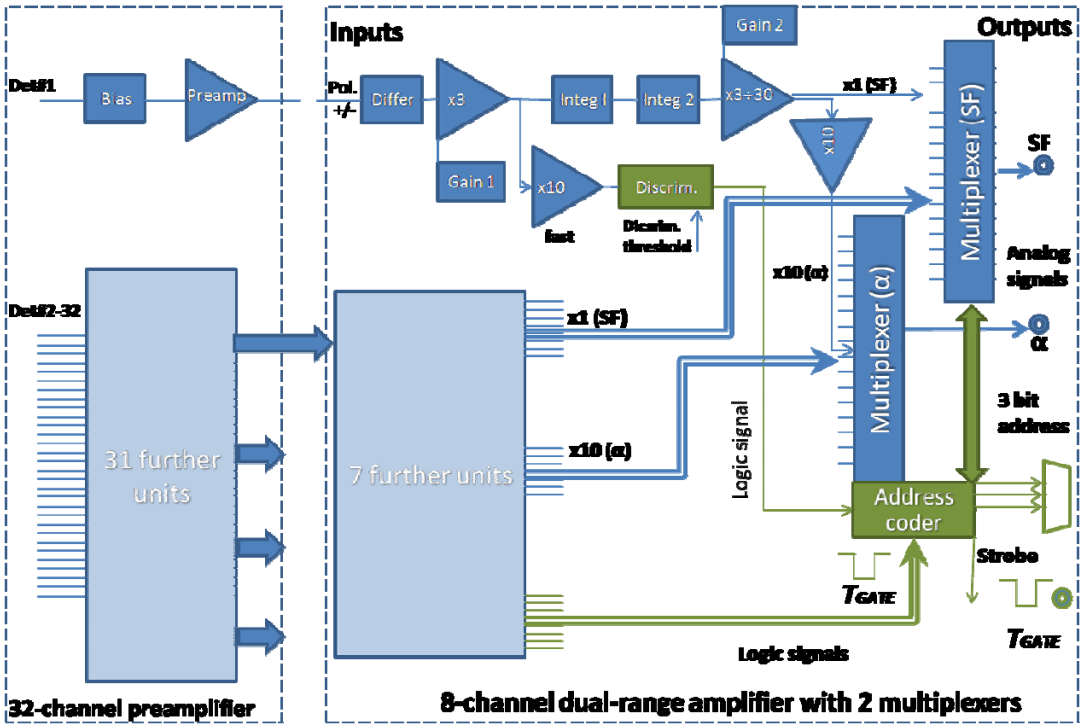

Fig. 5.10: Schematic of the TASCA analogue electronics.

Logical signals from low level discriminators go to the priority address coder, where they are converted to a 3-bit address *Code* for each of the 8 channels. The signals from channels with smaller numbers have priority: if two signals come in 2 different amplifier inputs at the same time, only the one with the smaller number will be processed. At the same time a *Strobe* signal (trigger) is created in the discriminator, its duration can be adjusted in the range from 1 to 10 μs (S_{trobe}). The address code opens the corresponding input of the 8-channel multiplexer for the time S_{trobe}.

If a detector has backswings, the base line restorer of the amplifier will generate an artificial potential to compensate a signal with inverted polarity to the zero level. This property of conventional amplifiers plays a negative role in processing signals from our strip DSSSD structures. By readout of the signal from the strip, “echo” signals with inverted polarity are generated in the neighboring strips. The base line restorer creates a positive potential compensating the negative input signal, and additional peaks from neighboring strips are generated artificially. Due to this fact, the amplifiers were

produced without base line restorers that do not influence the performance of the amplifiers at the expected counting rates not higher than about 50 Hz per strip.

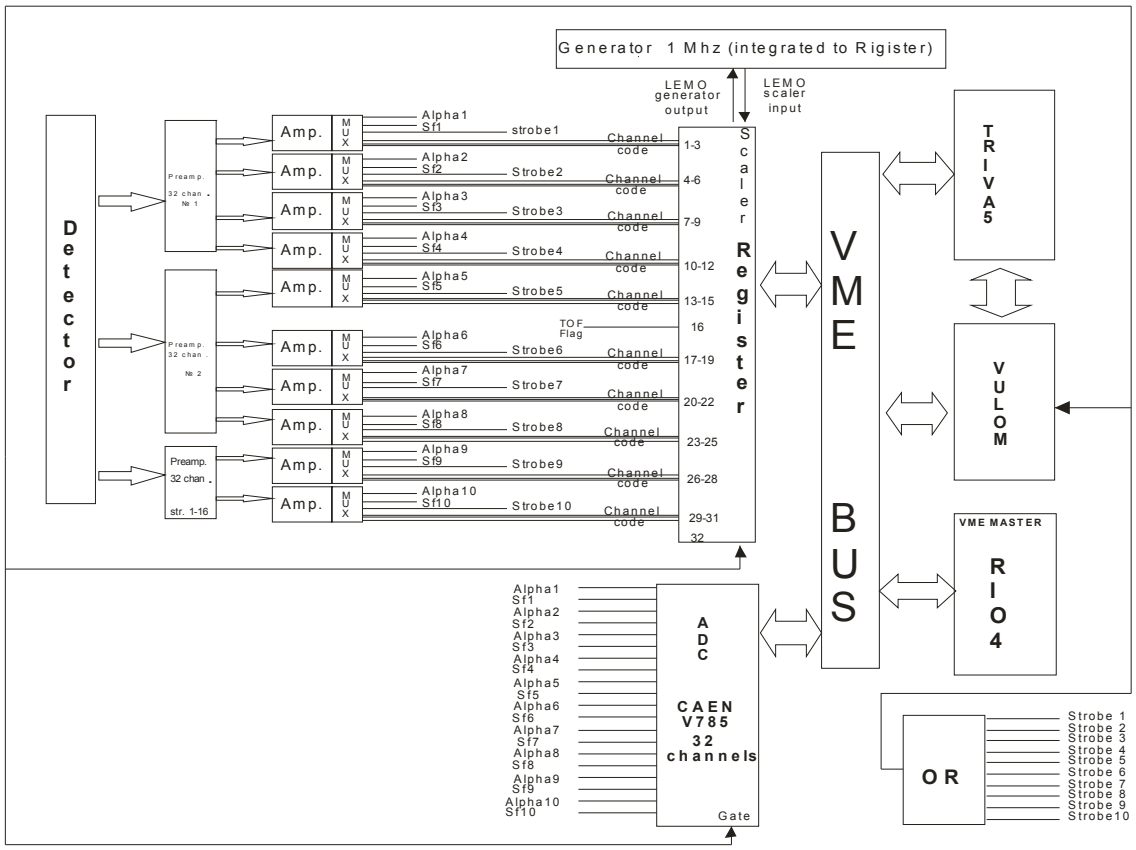

Fig. 5.11: Simplified scheme of the TASCA DAQ.

In total 40 digital 3-bit output signals from the amplifiers with address *Codes* of the fired amplifier inputs are stored in four 32-channel I/O VME registers SIS 3820-3600 (Struck GmbH). The *Code* signals with TTL standard have the high level (logical 1) at +5 V. The first input channel of the amplifier has address code 000, this corresponds to the low level at all three wires; the 8-th input channel has address code 111, this corresponds to the high level at all three wires.

All amplifiers have a logical *Strobe* output (trigger) adjustable by the low level discriminator threshold. All *Strobe* outputs from the amplifiers are collected by "OR" in a CAMAC Common Trigger Module resulting in a *(Common) Trigger* signal (see Fig. 5.11). The high level of the *Trigger* signal (logical 1) is 0 Volts (inverted TTL). The *Trigger* signal is converted to the ECL standard in a *TTL-ECL* converter and then provided to the *VME Universal LOgic Module (VULOM)*, which is connected to the

TRIVA5 VME trigger synchronizing module by an ECL input-output bus. The full scheme of DAQ electronics can be found in Appendix I.

While the *Trigger* signal reaches the *TRIVA5* through the *VULOM*, *TRIVA5* accepts the trigger signal and generates a short pulse at the *TDT* output, which is connected to the *VULOM*. The "busy" logic starts and all triggers will be rejected until the *VULOM* is read out as the last module in the VME crate. One VME reading cycle takes about 100-150 ns, thus, the lowest possible dead time can be 12-20 μs depending on the VME master configuration. The used version of the MBS software showed a total readout dead time of about 30 μs for readout of the whole FPDB. A significantly longer dead time of ~50 μs was measured with 7 additional Ge detectors during the experiment on the synthesis of element 114 (experimental setup is described in the next section).

Each registered event gets a time stamp from a 32-bit scaler with an internal programmable clock generator introduced in the SIS Register module. Analog signals from Ge-detectors are digitized in the 8-channel 100 MS/s 16-bit flash ADC SIS 3302 (Struck GmbH).

If the processed *Trigger* signal is accepted by the dead time logic, the amplitudes of all fired ADC channels, the status of all Registers, amplitudes from the flash ADC and time stamps are read out by a frontend VME controller RIO4 (CES) operating with the Multi-Branch System (MBS) software package [134,135]. Visualization as well as online and offline analysis was performed using the software package GSI Object Oriented On-line Off-line system (Go4) [136-138].

Chapter VI
First studies with the new TASCA focal plane detection system

Tests with No isotope and synthesis of element 114

The first experiment with SHE performed at TASCA using the new detection system was aimed at the synthesis of element 114 via the reaction $^{48}Ca+^{244}Pu$. This experiment must confirm that TASCA has unsurpassed efficiency for this nuclear reaction type and it is ready for the future experiments on the synthesis of new elements.

6.1 Experimental setup

A ^{48}Ca ion beam from the UNIversal Linear ACcelerator (UNILAC) at GSI, Darmstadt, Germany was used for the production of No isotopes and for the synthesis of element 114. The rotating target wheel ARTESIA was installed in the TASCA target chamber, which is separated from the accelerator beam line by a differential pumping system. Reaction products recoiling from the target were guided through the TASCA to the focal plane detector. TASCA was operated mostly in the high transmission mode and filled with 0.8 mbar He. The complete fusion reaction products were separated in the dipole chamber from the primary beam and from transfer reaction products by the magnetic rigidity and focused by two quadrupole magnets into the TASCA focal plane, where the new TASCA focal plane detector was installed (Fig. 6.1).

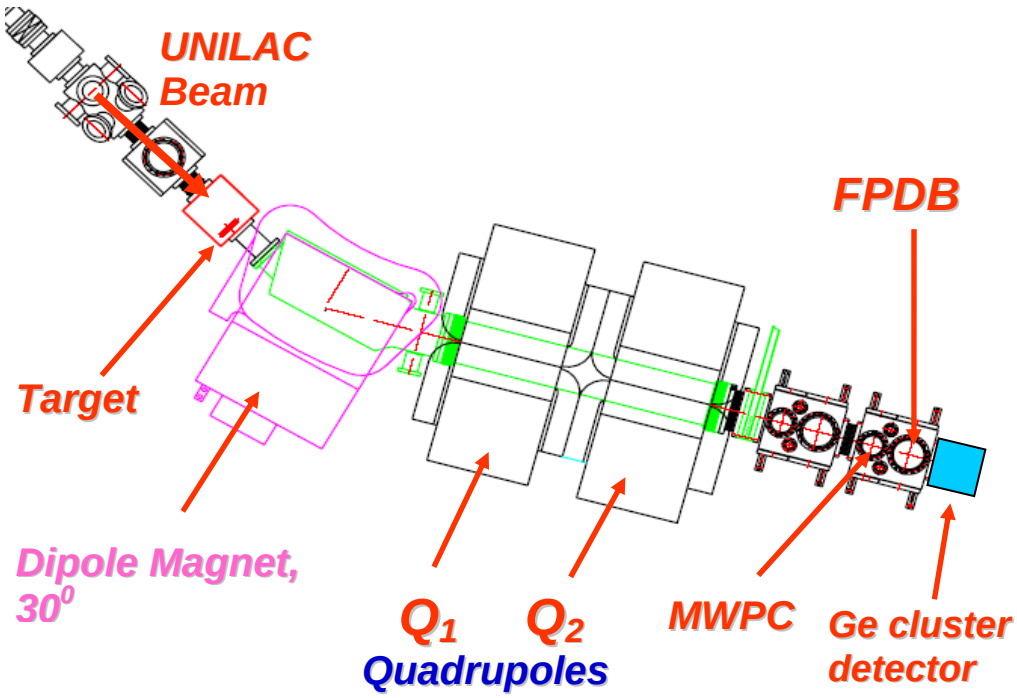

Fig. 6.1. Experimental setup for studies of ^{252}No and E114.

The detection system of TASCA consisted of a Multi Wire Proportional Counter (MWPC), a Focal Plane Detector Box (FPDB) and a germanium cluster detector.

The MWPC was located ~ 20 cm upstream of the FPDB and consisted of two 1-μm thick Mylar windows isolating an isobutane fill gas, held at a pressure of 3 mbar above the TASCA pressure. The MWPC comprised 3 wire grids: 1 anode and two cathode grids. The anode is biased at + 500 V and signals are read out from the cathodes. The distinction of radioactive decays of species implanted in the DSSSD from ions recoiling from the target is based on the (anti-)coincidence of DSSSD signals with MWPC signals.

A germanium cluster detector [111] with 7 independent germanium crystals was mounted behind the 1.5 mm thick Al flange at the exit of TASCA and ~ 2 cm from the FPDB.

The reaction ^{48}Ca + ^{206}Pb was studied before the main experiment on element 114 started. This study was aimed at tests of the new focal plane detection system and the new electronics.

6.2 Tests of the new TASCA detection system with ^{252}No

The FPD was calibrated off-line (in the absence of beam) with an external 4-peak α-particle source (^{148}Gd, ^{239}Pu, ^{241}Am, ^{244}Cm). In the presence of beam, the FPD was calibrated using reactions of ^{48}Ca with ^{206,208}Pb.

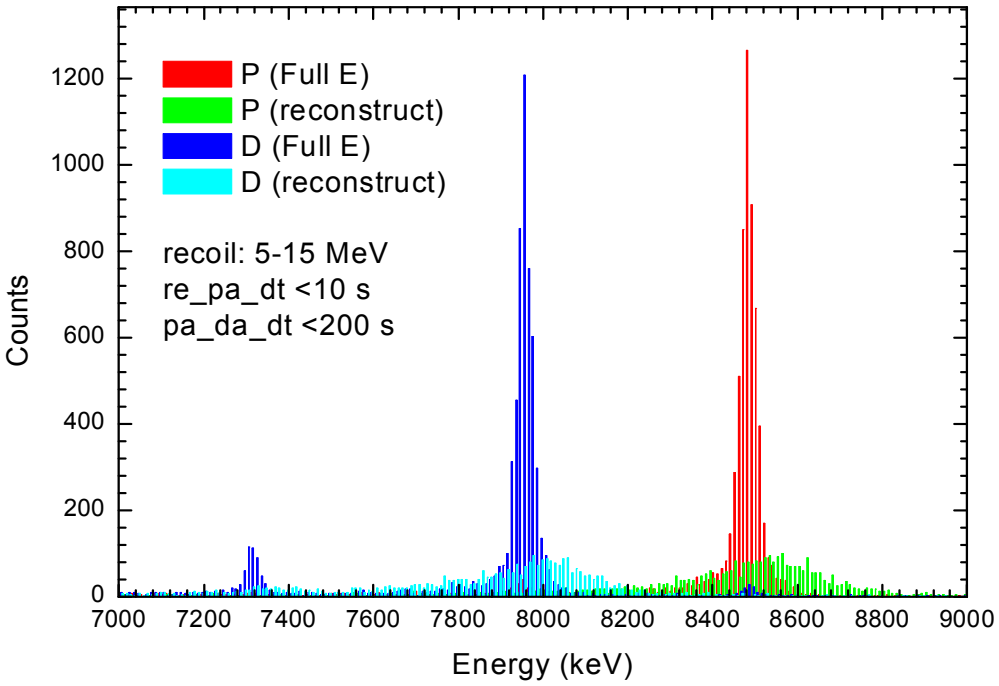

Figure 6.2: The energy resolution of "full energy" and "reconstructed" signals in the alpha particle spectrum of ^{252}No and ^{248}Fm.

The energy resolution was 20 keV full-width at half maximum (FWHM) for 8.1 MeV α-particles depositing their full energy in the DSSSD (full-energy α-particle) and 170 keV for α-particles that deposited a fraction of their energy inside the DSSSD and the remainder in the SSSSD (reconstructed α-particle). The high-energy calibration used for measuring fission fragment energies was obtained from extrapolating the calibration from the α-energy region. The SSSSD's high-energy calibration was rather poor due to the lack of high-statistics calibration data. The alpha particle spectrum and SF spectrum from No isotopes are presented in Fig. 6.2 and 6.3.

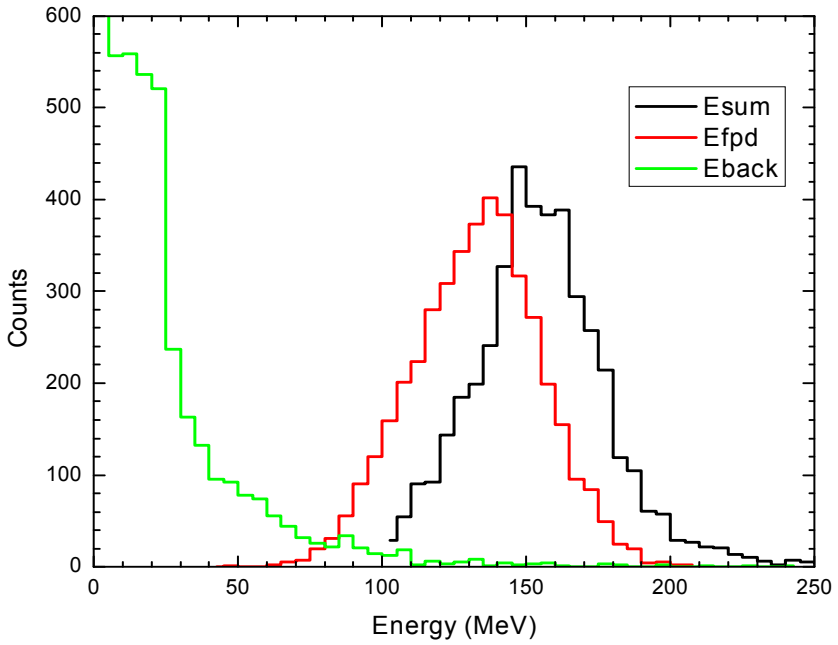

Fig. 6.3: SF spectrum of ^{252}No obtained in the implantation detector (red line), backward array detectors (green line) and the sum of them (black line).

To differentiate between SF events and events originating from unreacted beam, > 8000 EVR-SF correlations were produced in the ^{206}Pb(^{48}Ca, 2n)^{252}No reaction. SF events originating from the decay of ^{252}No had DSSSD energies centered around 150 MeV with a FWHM of ~ 25 MeV. SF-like events that occurred during beam pulses and were not preceded by an EVR had DSSSD energies peaked around 200 MeV with a FWHM of ~10 MeV. Due to this, SF events were defined as events with 80 < E_{SF} (MeV) < 400, E_{DSSSD} (MeV) < 190. To be considered correlated; all events were required to occur in the same pixel. The charge division between two neighboring strips was studied on both front and back sides using alpha particles and fission fragments of ^{252}No. In 21% of all cases the detected SF fragments signals were divided over two neighboring strips on the back side (see Fig. 6.4b)), but the charge division between neighboring strips on the front side was negligible - 0.008% only (see Fig. 6.4a)).

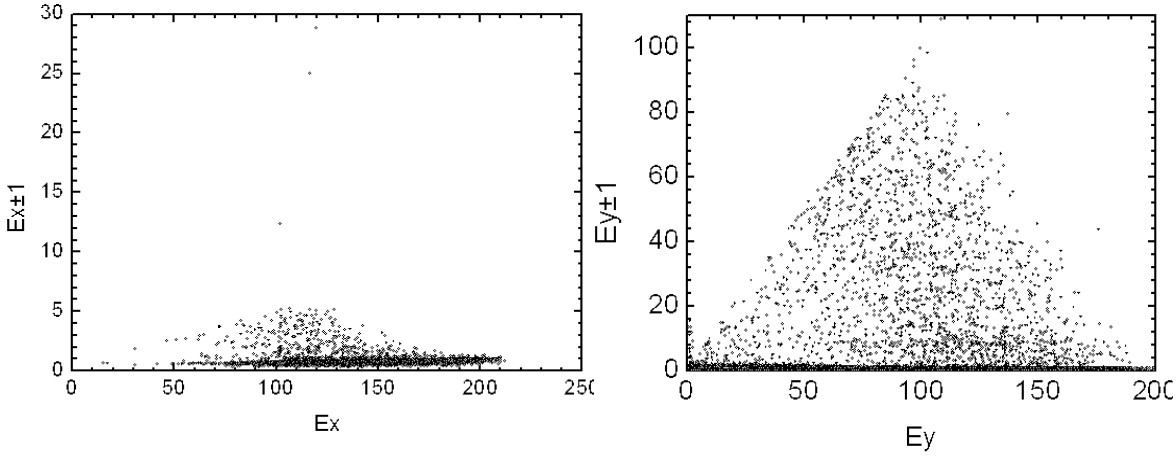

Fig. 6.4: The fission charge division between two neighboring strips of a) the front side and b) the back side.

For the alpha particles, 13% of the signals were divided between two neighboring strips on the back side, while no charge division on the front side could be measured (see Fig. 6.5). Thus, for the search of position correlated decay chains, the *x* position (front strip number) should be the same for all decay chain members, but the *y* position (back strip number) can differ by one.

The efficiency for detecting α-particles was measured to be ~ 72% of 4π: 50% of all α-particles deposit their full energy in the implantation detector. An additional 22% of the α-particles lose a fraction of their energy in the implantation detector and hit an upstream detector of the backward array. Their full energy can thus be reconstructed by summing the signals in both the implantation and upstream detectors. Of the remaining 28% of all α-particles, most escape out of the front of the detector box at an angle that cannot hit the backward array or deposits less than 300 keV in the FPD, below the thresholds required to trigger data acquisition.

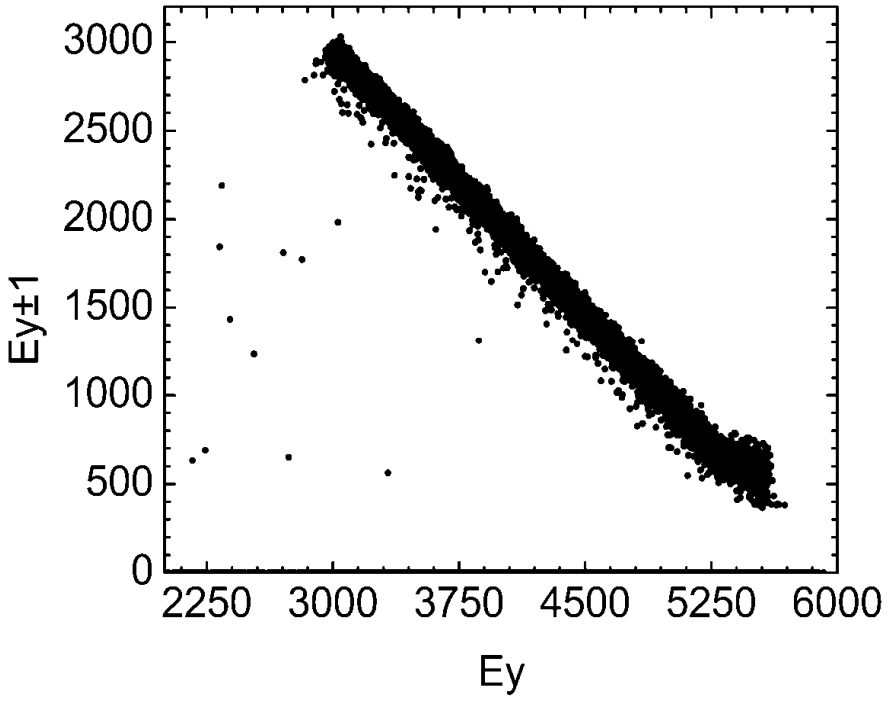

Fig. 6.5: The α-particle charge division between two neighboring strips of the back side.

Standard γ-ray sources of ^{152}Eu and ^{241}Am were used for off-line germanium cluster detector energy calibrations. On-line calibrations were performed using the ^{207}Pb(^{48}Ca, 2n)^{253}No reaction. During this test, ~ 10 000 ^{253}No α-like particles [7.9 < E_α(MeV) < 8.3, anti-coincident with MWPC] were observed. Fig. 6.6 contains a spectrum of all γ-rays coincident with ^{253}No α-like events. Two γ-ray peaks at 222.2 and 279.2 keV were observed. The 222.2 keV peak contained 51 γ-rays and an additional 15 γ-rays were observed in the 279.2 keV peak. Based on these numbers, the intensities from [141], and the efficiency obtained from off-line calibrations with a ^{152}Eu source, we were able to verify the timing of the germanium cluster detector.

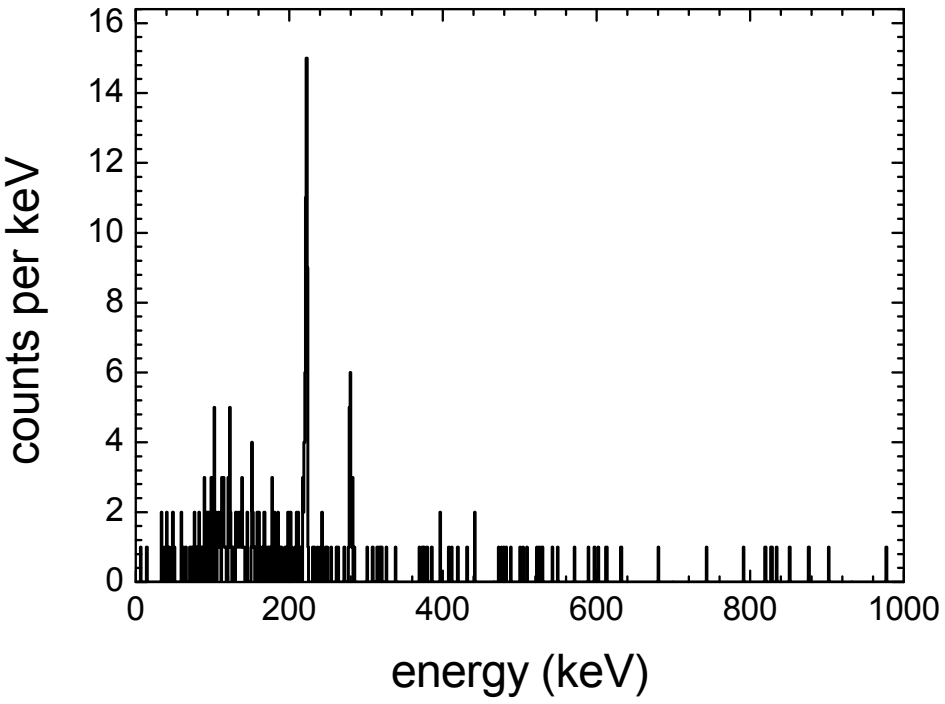

Fig. 6.6: Spectrum of γ-rays in coincidence with ^{253}No α-decays.

6.3 E114 experiment

A pulsed (5 ms on / 15 ms off) $^{48}Ca^{10+}$ beam from an ECR ion source was accelerated by the UNIversal Linear ACcelerator (UNILAC) at GSI, Darmstadt, Germany, to energies of 259.4 MeV and 254.6 MeV. The beam first passed through an induction coil to measure the beam intensity in a non-destructive way. It then passed through 2.22±0.05 μm thick Ti target backings before entering the $^{244}PuO_2$ targets (isotopic composition: 97.9% ^{244}Pu; 1.3% ^{242}Pu; 0.7% ^{240}Pu; <0.1% other). Three arc-shaped target segments were mounted on a target wheel, which rotated synchronously with the beam macrostructure. Over the course of the experiment, four target segments with a beam dose weighted average target thickness of 438 μg·cm^{-2} ^{244}Pu were irradiated with typical beam intensities of $2 \cdot 10^{12}$ particles·s^{-1}. First, beam energies inside the target material were 241.3 - 246.2 MeV [139], corresponding to compound nucleus excitation energies, E*, within the target of 39.8-43.9 MeV (E* in the center of the targets $E^*_{c.o.t.}$=41.7 MeV [140]; hereafter referred to as 42-MeV run). Later, beam energies of 236.4-241.0 MeV resulting in E* inside the target of 36.1-39.5 MeV ($E^*_{c.o.t.}$=37.5 MeV; 38-MeV run) were used. Beam doses of $2.44 \cdot 10^{18}$ (42-MeV run) and

$1.15 \cdot 10^{18}$ (38-MeV run) particles were acquired. Nuclear reaction products as well as the unreacted beam entered TASCA, which was operated in its HTM mode [71]. Recoiling ions were separated by their differing magnetic rigidities, $B \cdot \rho$, in 0.8 mbar He gas inside of TASCA. The $B \cdot \rho$ of $^{288,289}114$ was estimated according to [77].

We searched for time- and position-correlated decay chains consisting of an EVR, one or more α -particles and terminating with an SF. EVRs were defined as events during the beam pulse with $3.0 < E_{EVR}\,(\text{MeV}) < 15.0$ and coincident with a signal from the MWPC. α-particles were events anti-coincident with a signal from the MWPC and could occur either during or in-between beam pulses.

The isotope $^{288}114$ was identified by detection of EVR-α-SF correlations that consisted of and EVR followed by an α-particle [$9.7 < E_\alpha\,(\text{MeV}) < 10.2$] within 7 s and an SF within 1 s. The isotope $^{289}114$ was identified by EVR-α-α-SF correlations that consisted of an EVR followed by an α-particle [$9.7 < E_\alpha\,(\text{MeV}) < 10.2$] within 7 s, a second α-particle [$9.0 < E_\alpha\,(\text{MeV}) < 9.5$] within 150 s and terminated by a SF-like event within 50 s of the last α -particle. All events between the EVR and the terminating SF were also checked for additional EVR- or α - like [$8.0 < E_\alpha\,(\text{MeV}) < 12.0$] events. Direct SF of $^{288,289}114$ was not searched for due to the high rate of SF-like events.

Eleven EVR-α-SF chains observed in the $^{48}Ca + ^{244}Pu$ reaction were assigned to the decay of $^{288}114$ (events 2-9, 11, 12, 14, and 15 in Table 6.1). Nine of these events were observed during the 42-MeV HTM irradiation, two during the 42-MeV SIM irradiation and an additional event during the 38-MeV SIM irradiation. The half-life originating from these 11 decays is $0.52^{+0.13}_{-0.09}$ s for $^{288}114$ and $0.11^{+0.03}_{-0.02}$ s for $^{284}112$, in agreement with those published in [27]. The α-particle energies and the half-lives from $^{288,289}114$ decays observed in TASCA experiment are in full agreement with the reported in [27]. The decay properties for observed nuclei are summarized in Fig. 6.7 in comparison with Dubna data.

During the $^{48}Ca + ^{244}Pu$ irradiation, we searched for X- or γ-rays in coincidence with all decays in the $^{288,289}114$ decay chains. γ-rays were identified with all of the SF events. However, no X- or γ-rays were observed in coincidence with any α-particle from the $^{288,289}114$ decay chains.

Table 6.1: Observed 114 decay chains. For reconstructed energies, the energies recorded in the FPD and upstream detectors, respectively, are listed in parentheses. SF energies are shown in boldface.

E* (MeV)	Event no.	TASCA Mode	X Strip	Y Strip	E_{EVR} (MeV)	Decay Energy (MeV)	Lifetime	^{A}Z
41.7	1	HTM	22	11	6.41	9.847	3.589 s	$^{289}114$[a]
						9.212	22.147 s	$^{285}112$[a]
						8.727	5.688 s	^{281}Ds[a]
						211 (136+75)	4.502 ms	^{277}Hs[a]
41.7	2	HTM	91	18	6.51	9.982	0.242 s	$^{288}114$
						196(187+9)	0.130 s	$^{284}112$[a]
41.7	3	HTM	103	31	7.60	9.814 (1.236+8.578)	1.348 s	$^{288}114$[a]
						272 (130+142)	0.059 s	$^{284}112$[a]
41.7	4	HTM	83	18	5.97	10.062 (0.575+9.487)	0.649 s	$^{288}114$[a]
						163 (151+12)	0.171 s	$^{284}112$
41.7	5	HTM	102	24	8.69	9.915	0.446 s	$^{288}114$[a]
						194	0.087 s	$^{284}112$[a]
41.7	6	HTM	110	19+20 [b]	7.99	9.919	1.164 s	$^{288}114$
						222 (158+64)	0.343 s	$^{284}112$[a]
41.7	7	HTM	119	29	9.10	9.980	0.242 s	$^{288}114$[a]
						180	0.026 s	$^{284}112$[a]
41.7	8	HTM	19	21+22 [b]	13.22	9.947	0.763 s	$^{288}114$
						198	0.029 s	$^{284}112$[a]
41.7	9	HTM	86	20+21 [b]	6.56	9.917	0.345 s	$^{289}114$[a]
						9.194	51.037 s	$^{285}112$[a]
						198	35.476 s	^{281}Ds[a]
41.7	10	HTM	131	26	7.35	9.700 (0.838+8.862)	0.823 s	$^{288}114$[a]
						170	0.063 s	$^{284}112$[a]
37.5	11	HTM	89	24	8.67	9.965	0.482 s	$^{288}114$[a]
						161	0.401 s	$^{284}112$[a]
37.5	12	HTM	100	5	6.93	9.847	0.774 s	$^{289}114$[a]
						9.229	9.542 s	$^{285}112$[a]
						278 (154+124)	28.413 s	^{281}Ds[a]
37.5	13	HTM	122	40	3.26	9.847	0.904 s	$^{289}114$
						9.220	92.202 s	$^{285}112$[a]
						146 (102+44)	46.283 s	^{281}Ds[a]
41.7	14	SIM	59	47	8.458	9947	1.132 s	$^{288}114$[a]
						210	0.043 s	$^{284}112$[a]
41.7	15	SIM	89	0	7.605	9848	0.921 s	$^{288}114$
						196	0.390 s	$^{284}112$[a]

[a] Decay observed in between beam pulse s.

[b] All events in the chain were split between two Y strips

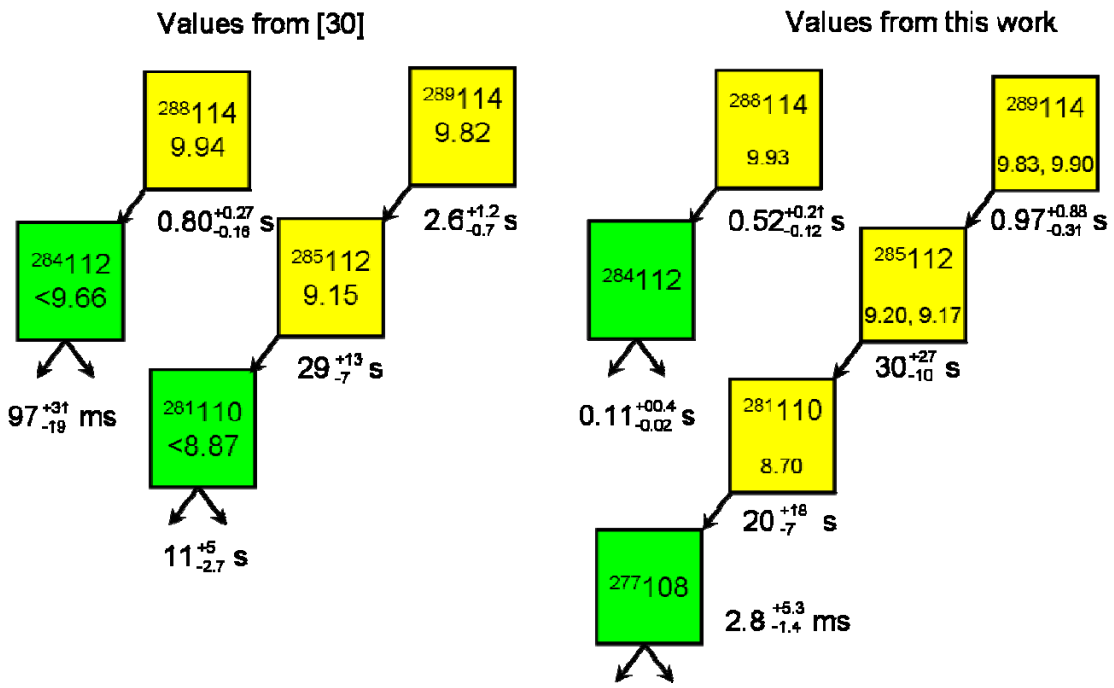

Fig. 6.7: The deduced decay properties for ^{288,289}114 decay chains in comparison with data from [27].

6.4 Random Rates

Fig. 6.8 shows the total low [7 ≤ E (MeV) ≤ 12] and high [25 ≤ E (MeV) ≤ 250] energy spectra recorded in the implantation detector during the HTM and SIM portions of the ^{48}Ca + ^{244}Pu run. The spectra of α- and SF-like events in the implantation detector both during and outside of the beam pulse for the SIM and HTM runs are also included. In blue are the implantation detector energies of events within the decay chains presented in Table 6.1. In the HTM high energy spectra, a peak due to scattered beam reaching the FPD appears at ~ 210 MeV. The peak at ~ 50 MeV in both the HTM and SIM spectra is due to transfer reaction products that are formed with twice the momentum of the beam, recoil out of the target and are guided to the FPD by TASCA. A small portion of these events appear to occur outside of the beam pulse due to an uncertainty in measuring the start of the beam-pulse. An additional peak occurs around 150 MeV in the SF-like events occurring outside of the beam-pulse. These are correlated to high energy of EVRs on the millisecond timescale and were assigned to the decay of americium fission isomers. The number of expected random EVR-α-SF and EVR-α-α-SF correlations was calculated by taking the observed number of SF events and multiplying by the probability of observing an EVR-α or EVR-α-α

correlation in the same pixel preceding the SF within the predefined time window. The rate of EVR-, α- and SF-like events during and outside of the beam pulse during normal operation is shown in Table 6.2.

During portions of the run in which a crack was in the target, the rate of α-like events increased by a factor of 10. The rate of SF-like events inside the beam pulse increased by a factor of 150, however, outside of the beam pulse, the rate of SF-like events did not increase. As such, for portions of the run when there was a crack in the target, SF-like events were required to occur outside of the beam pulse.

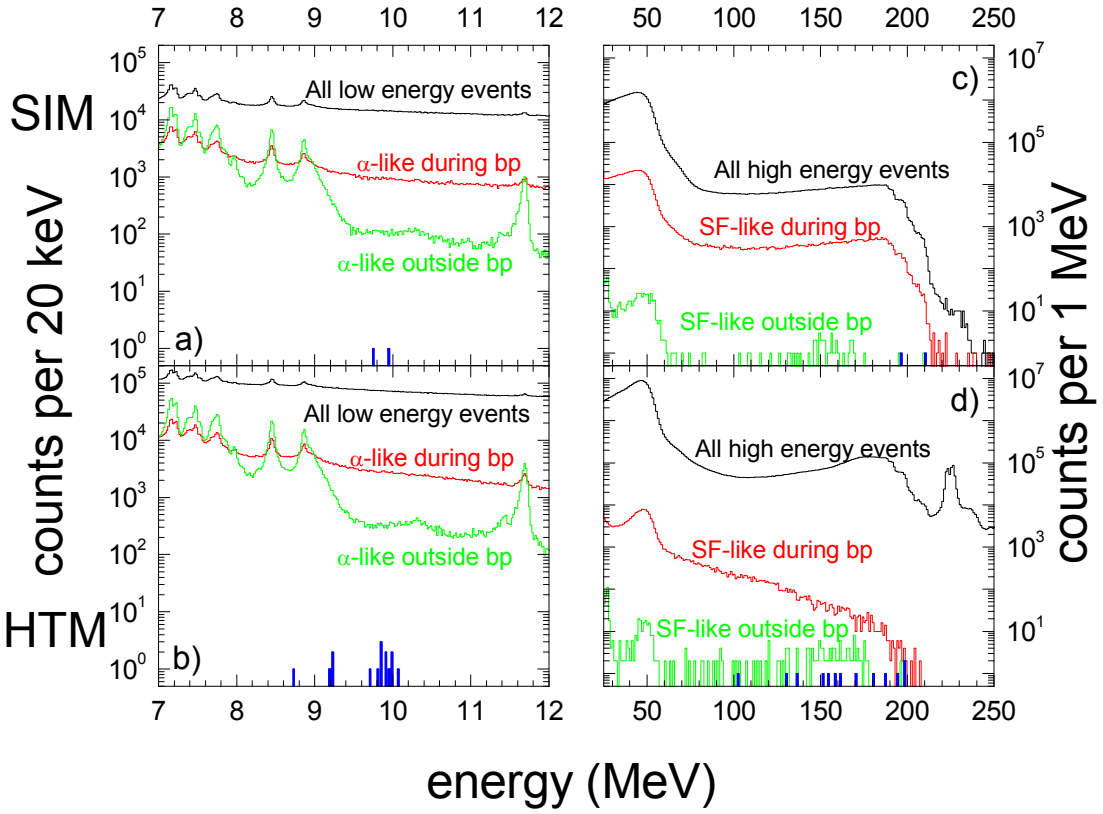

Fig. 6.8: Energy spectra recorded in the DSSSD during the ^{48}Ca + ^{244}Pu run. (Left) Total energy spectra of all low energy events and α like signals during the beam pulse (bp) and outside of the beam pulse for the SIM (a) and HTM (b) portions of the run. (Right) Total energy spectra of all high energy events and SF-like signals during and outside of the beam pulse for the SIM (c) and HTM (d) portions of the run. The blue histograms show the energies of α-events and DSSSD portion of energies the SF-events observed in correlated decay chains.

During the experiment, there were 426 SF-like events occurring outside of the beam pulse. With the caveat that SF events occurred out of the beam pulse, we were able to widen the correlation search gates for ^{288,289}114.

For ^{288}114, correlation gates were widened to EVR [3.0 < E_{EVR} (MeV) < 15.0] followed by an α-particle [8.0 < E_{α} (MeV) < 12.0] within 30 s and terminated by a SF-like event outside of the beam pulse and within 50 s of the α-particle. With these wide gates, we expected to observe 3.0 random correlations of unrelated events. A total of 16 chains were observed. 11 had decay properties similar to ^{288}114 and where thus assigned (see chains 2 - 8, 10 - 11, 14 - 15 in Table 6.1). The remaining 5 chains were assigned to random correlations of unrelated events based on one or more of the following conditions: (i) the alpha energy was more than 500 keV lower than energies reported by the Dubna-Livermore collaboration, (ii) the lifetime of the parent alpha was more than 3 times longer than the longest reported ^{288}114 lifetime or (iii) the lifetime of the fission event was more than 3 times longer than the longest reported ^{284}112 lifetime.

Table 6.2: Average rate of events during the HTM and SIM runs when there was not a crack in the targets.

Event Type	During Beam-pulse		Outside of Beam-pulse	
	HTM	SIM	HTM	SIM
EVR: 3.0 < E_{EVR} (MeV) < 15.0	38 s^{-1}	29 s^{-1}		
Alpha: 9.7 < E_{α} (MeV) < 10.2	0.25 s^{-1}	0.10 s^{-1}	0.03 s^{-1}	0.01 s^{-1}
Alpha: 9.0 <E_{α} (MeV) < 9.5	0.31 s^{-1}	0.14 s^{-1}	0.10 s^{-1}	0.04 s^{-1}
Alpha: 8.0 < E_{α} (MeV) < 12.0	2.29 s^{-1}	0.99 s^{-1}	0.81 s^{-1}	0.37 s^{-1}
SF: 80 < E_{SF} (MeV) < 400	0.01 s^{-1}	0.07 s^{-1}	2.21E-4 s^{-1}	8.88E-5 s^{-1}
E_{FPD} (MeV) < 200				

For ^{289}114 we searched for EVR-α-α-F correlations that consisted of an EVR [3.0 < E_{EVR} (MeV) < 15.0] followed by an α-particle [8.0 < E_{α} (MeV) < 12.0] within 30 s, a seconds α-particle [8.0 < E_{α} (MeV) < 12.0] within 150 s and terminated by a SF-like event outside of the beam pulse and within 50 s of the last α-particle. A total of 5 EVR-α-α-SF correlations were observed where 1.3 were expected due to random correlations of unrelated events. Four of the EVR-α-α-SF correlations had decay properties similar to those published for ^{289}114 and were thus assigned (chains 1, 9, 12, and 13 in Table 6.1). The remaining correlation [EVR (E_{EVR} = 8.88 MeV) – α (E_{α} =

11.89 MeV, τ_α = 13.227 s) - α (E_α = 8.81 MeV, τ_α = 109.602 s) – SF (165 MeV, τ_{SF} = 6.05 s)] was assigned to random, uncorrelated decays of transfer reaction products.

Based on the decay properties of chains ending with out-of-beam SF events, we narrowed the gates to search for chains ending with in-beam SF events. During the portions of the run where the background was considered "low" enough to extend this search, there were 15499 SF-like events. ^{288}114 was identified by detection of EVR-α-SF correlations that consisted of and EVR followed by an α-particle [9.7 < E_α (MeV) < 10.2] within 7 s and an SF within 1 s. ^{289}114 was identified by EVR-α-α-SF correlations that consisted of an EVR followed by an α-particle [9.7 < E_α (MeV) < 10.2] within 7 s, a second α-particle [9.0 < E_α (MeV) < 9.5] within 150 s and terminated by a SF-like event within 50 s of the last α-particle. The number of expected random decay chains with the terminating SF outside of the beam pulse was $4 \cdot 10^{-4}$ and $2 \cdot 10^{-4}$ for ^{288}114 and ^{289}114, respectively. When including in-beam SF events, the number of expected random correlations increased to 0.02 and 0.05 for ^{288}114 and ^{289}114, respectively.

For each chain, all events between the EVR and the terminating SF were checked for additional EVR- or α-like [8.0 < E_α (MeV) < 12.0] events. Chain 1 in Table 6.1 contained an additional EVR between α-particles 1 and 2, in the same pixel as the decay chain. The rate of EVR-like events during the run was 38 s^{-1} over the entire detector. With this rate, we expect 2.3 EVRs to occur during a decay chain and within the same pixel. In addition to the extra EVR in chain 1, chain 13 also contains an additional 14.04 MeV EVR 124.336 s after the 114 implantation. Chain 1 also contains an 8.77 MeV α-particle that was assigned to the α-decay of ^{281}Ds. The rate of α-like events [8.0 < E_α (MeV) < 12.0] during the experiment was 2.29 s^{-1} over the entire detector. The probability that any one of the decay chains contained a random α-like event is <0.1%. No other spurious α-like events were observed in any of the other 14 decay chains.

The original element 114 discovery claim was based on the observation of a 34-min long EVR-α-α-α-SF chain [142]. We extended our correlation parameters to search for chains of similar type with α-particle energy windows of 500 keV and lifetime windows three times longer than the lifetimes observed in [142]. This led to search parameters of EVR-α-α -α-SF correlations consisting of an EVR [3.0 < E_{EVR} (MeV) < 15.0] followed by an α-particle [9.5 < E_α (MeV) < 10.] within 90 s, a second α-particle

[8.4 < E_α (MeV) < 8.9] within 45 min, a third α-article [8.6 < E_α (MeV) < 9.1] within 4.8 min and terminated by a SF-like event outside of the beam pulse and within 50 min of the last α-particle. Unfortunately, with these gates, the number of expected random correlations was too high to allow the identification of chains similar to those reported in [142].

Chapter VII

Summary and outlook

Results and future plans

SHEs exist solely because of nuclear stability enhancement due to shell effects. Experimental studies have shown that cross sections for the synthesis of SHE decrease continuously, with exception of warm fusion reactions of doubly magic ^{48}Ca with actinide targets. Exploration of SHE nuclei is close to the border of present technical limitations due to low cross sections and, therefore, due to the significant increase of the luminosity of experiments and of the background from byproducts. These technical challenges call for a further improvement of the separation and detection approaches for the synthesis of new elements.

Gas-filled recoil separators have acquired a reputation as useful instruments for the separation and investigation of heavy and superheavy elements (SHE) [72,101,77,149]. The most exciting results are the observation of superheavy elements in ^{48}Ca induced reactions [27] during the last 10 years at the DGFRS (Dubna, Russia), the identification of element 113 produced in a cold fusion reaction at GARIS (RIKEN, Japan) [145], systematic studies of synthesis of the SHE in hot fusion reactions with U target at BGS (Berkeley, USA) [146], and detailed nuclear spectroscopic investigations in the element 102 region at RITU (Jyvaskyla, Finland) [101]. The most important characteristics of gas-filled recoil separators are their high acceptance and high transmission, good primary beam suppression and reduction of unwanted transfer reaction products. Compared to vacuum recoil separators, such as velocity or energy filters, the additional auto-focusing of evaporation residues (EVR) due to the averaging of the ion charge in the gas gives gas-filled separators certain advantages [148].

The **T**rans**A**ctinide **S**eparator and **C**hemistry **A**pparatus (**TASCA**) project [149], which is focusing on the investigation of neutron-rich transactinide nuclides produced in reactions with heavy actinide-targets, has successfully finished its commissioning phase. TASCA is ready for the envisioned research program which includes both chemical investigations of transactinide or superheavy elements (SHE) after

preseparation with the gas-filled separator and physics motivated nuclear structure and nuclear reaction studies.

TASCA with a DQQ magnet configuration has the unique ability to run in two different ion-optical working modes, the "High Transmission Mode" and the "Small Image Mode", resulting either in highest transmission or in a well focused product distribution, respectively. The unsurpassed transmission of TASCA in HTM of ~ 60% for the reaction type ^{48}Ca +An is exploited at a relatively low dispersion. In contrast, due its small spot size in the focal plane (< 3 cm) at a still relatively high transmission, the SIM provides a very unique possibility for chemical investigations of short-lived transactinides and for nuclear spectroscopy measurements with high detection efficiency [107,123,149,150].

The final commissioning experiment ^{244}Pu(^{22}Ne, xn) has been carried out in July 2008, to shed more light on the decay properties of Rf isotopes in the transition region between the N = 152 and the N = 162 neutron shells. The measurement of the half-life of ^{262}Rf and the observation of ^{261b}Rf as a direct product of the complete fusion reaction were the two main goals of this experiment. These goals were achieved, as the nuclides ^{260}Rf, ^{261a}Rf, ^{261b}Rf, and ^{262}Rf were successfully synthesized in the nuclear fusion reaction ^{22}Ne(^{244}Pu, xn)$^{266-x}$Rf (x = 4 - 6) and unambiguously identified via detection in ROMA or in one of two focal plane detectors, which were tested as prototypes for the new TASCA detection system. The measured half-lives of $20.4^{+12.4}_{-5.6}$ ms for ^{260}Rf and $2.2^{+1.0}_{-0.5}$ s for ^{261b}Rf are in a good agreement with previously published values [48,112]. The ^{262}Rf half-life of 190^{+100}_{-50} ms was measured for the first time in a focal plane detector of a recoil separator. This value is in contradiction with previous values reported by Lane (2.1 s) and Somerville (47 ms) measured by other techniques [112,42]. However, it is in good agreement with a value of 0.21 s calculated by Smolanczuk *et al.* [4].

The existence of two isomeric states in the isotope ^{261}Rf has been confirmed; both states can be produced on the one hand as evaporation residues in fusion – neutron evaporation reactions, on the other hand also as alpha-decay products of ^{265}Sg. The isomeric production ratio of both states in the reaction ^{22}Ne + ^{244}Pu, σ^{261a}Rf : σ^{261b}Rf, is 2.5:1. The unusually high overall transmission of TASCA of 10.5% was measured for Rf isotopes produced via the very asymmetric reaction. This allows systematical

investigations of the decay properties of ^{261a,b}Rf with reasonable statistics, while the maximum production cross section reaches a few nanobarns.

All setups described above for SHE studies use PSSSD detectors as implantation detectors, and only RITU uses DSSSD detectors in the GREAT spectrometer. Both types of detectors were examined in detail during the TASCA commissioning phase. Many measurements have demonstrated the advantage of the DSSSD compared to the PSSSD in the absolute position determination due to the smaller pixel size. Based on results of test experiments, the new TASCA focal plane detector setup based on DSSSD structures as the implantation detector with a size of 144 x 48 mm^2 has been designed and manufactured in cooperation with the Institute of Electron Technology in Warsaw (Poland). The new TASCA focal plane detector setup consisting of the MWPC and the FPDB has been used successfully in test experiments with No isotopes and in experiment on the synthesis of element 114 at TASCA. The TASCA FPDB provides a good energy resolution of ≤ 25 keV (FWHM) for 8.1 MeV α-particles measured from implanted ^{254}No depositing their full energy in the DSSSD and 170 keV for reconstructed α-particles that deposited part of the energy inside the DSSSD and part in the SSSSD. The average detection efficiency of the FPDB for α-particles emitted from a nucleus implanted in the active area of the DSSSD is 72%. The punch-through detector together with the MWPC serves for discriminating between ions recoiling from the target, radioactive decays of implanted species, and fast light ions. Additional Ge-detectors behind the FPDB were installed for γ-ray measurements in coincidence with α- or SF decays.

In total 640 spectrometric channels (320 for the α-particle branch and 320 for the SF branch) are required to readout the FPDB. The dedicated analogue and digital electronics in CAMAC and VME standard were designed and implemented. To minimize the total number of ADC channels, 8-channel dual-range amplifiers with integrated multiplexers were built. The multiplexed analog output signals are digitized in three 32-channel peak sensing ADCs V785 (CAEN), while 3-bit address codes of the fired strips are processed in four 32-channel I/O VME registers SIS 3820-3600 (Struck GmbH). This proposed scheme allows to significantly decrease the number of required ADS channels, and therefore the costs of the electronics. The total readout dead time of ~ 30 μs was measured for the FPDB (without Ge-detectors). The software package Go4 was adapted for the visualization as well as for the on-line and off-line analysis [138].

The new detector setup and new DAQ system have been used during a successful experiment on the synthesis of element 114 performed at TASCA in 2009. In total, 15 decay chains from two isotopes of element 114, ^{288}114 and ^{289}114, have been observed during a 29-day beam time. Cross sections, decay modes, α-particle energies, and half-lives agree with those reported from the DGFRS collaboration [27]. The decay properties and the data on the production cross sections were improved, and a previously unobserved α-decay branch in ^{281}Ds has been observed for the first time, leading to the discovery of the isotope ^{277}Hs [151]. The high cross sections and observation of two of the ^{288}114 decay chains in the SIM demonstrate that TASCA is ideal for use as a physical preseparator in future studies of the chemistry of element 114.

The significant improvement in the TASCA detection system and DAQ electronics opens up new opportunities for SHE studies by allowing the safe detection of very rare events with high efficiency, good energy and position resolution and with rather low dead time. Further developments of the TASCA detection system are possible. The E114 experiment has showed, that the energy resolution of the SSSSD detectors, which have a large strip surface and, therefore, a large capacity, can be improved, as it is required for spectroscopy experiments. This can be done by using Si wafers with a higher resistivity and by a better cleaning of the Si wafer surfaces at all production stages. The MWPC detector needs to be improved to reach a better signal to noise ratio. The working gas in the MWPC was isobutene at the pressure of 4 mbar. Heavier gases (or vapors) like pentane or heptanes give stronger amplification of signals in the low pressure range and should be tested as a MWPC working gas. A new grid and chamber design can be developed for more stable conditions against discharge due to high voltage, as well as for better gas circulation in the chamber. The use of a MWPC as a TOF detector is limited for asymmetric reactions due to the short stopping ranges of the EVRs in the Mylar foil serving as windows. Due this fact, the TOF detector scheme, where the MWPC is used as a start detector and the implantation detector is used as a stop detector, can be modified. The whole volume of the detector chamber, where the MWPC and the FPDB are installed, can be separated from the He atmosphere in TASCA by one thin Mylar window, which can withstand a minimal pressure difference of ~ 1 mbar. In this case, additional grids can be mounted in the detector chamber volume in front of the implantation detector providing a stop signal. The use of two MWPC as start and stop TOF detectors allow ΔE measurements for all ions and,

therefore, a better distinction between products of complete fusion- and multinucleon transfer reactions.

References

1. V. M. Strutinsky. Shell effects in nuclear masses and deformation energies. *Nucl. Phys. A*, **95**(952),420 (1967)
2. A. Sobiczewski, F.A. Gareev, B.N. Kalinkin. Closed shells for $Z > 82$ and $N > 126$ in a diffuse potential well *Phys. Lett.,* **22**, 500, 1966.
3. H. Meldner, *Ark. Fys*., **36**, 593 (1967)
4. U. Mosel , W. Greiner,: Z. Phys. A **222**, 261 (1969)
5. R. Smolanczuk et al., Phys. Rev. C **52**, 1871 (1995)
6. K. Rutz, M. Bender, T. Bürvenich, T. Schilling, P.-G. Reinhard, J. A. Maruhn, and W. Greiner. Superheavy nuclei in self-consistent nuclear calculations. *Physical Review C*, **56**,238–243, July 1997
7. W.D. Myers, W.J. Swiatecki, Nucl. Phys. **81**, (1966)
8. S.G. Nilsson, et al., Nucl. Phys. A **115**, 545 (1968)
9. S. G. Nilsson et al., Phys. Lett. B **28**, 458 (1969)
10. E. O. Fiset, J. R. Nix, Nucl. Phys. A **193**, 647 (1972)
11. J. Randrup et al., Phys. Rev. C **13**, 229 (1976)
12. K. S. Krane, Introductory Nuclear Physics. New York, John Wiley & Sons, Inc. (1988)
13. C. F. Weizäcker, "Zur Theorie der Kernmassen." Zeitschrift für Physik 96: 431-458 (1935)
14. Glenn T. Seaborg and Walter D. Loveland, The Elements Beyond Uranium. Wiley, New York, 1990.
15. M. G. Mayer, Phys. Rev. **75**, 1969 (1949)
16. O. Haxel, J. H. D. Jensen, H. E. Suess, Phys. Rev. 113, 1766 (1949)
17. R. D. Woods and D. S. Saxon, Phys. Rev. 95, 577-578 (1954)
18. M. G. Mayer. Nuclear configurations in the spin-orbit coupling model. Part I Empirical evidence. Phys. Rev., **78,** 16 (1950)
19. M. G. Mayer. Nuclear configurations in the spin-orbit coupling model. Part II Theoretical considerations. Phys. Rev., **78,** 22 (1950)
20. B.R. Mottelson and S.G. Nilsson, Phys. Rev. 99, (1955) 1615
21. S. G. Nilsson. Binding states of individual nucleons in strongly deformed nuclei. Kgl. Danske Videnskab. Selskab*, Mat.-fys. Medd*., **29**(16), (1955)
22. P. Möller, J. R. Nix, and K.-L. Kratz. Nuclear Properties for Astrophysicaland Radioactive-Ion Beam Applications. *Atomic Data and Nuclear Data Tables*, **66**,131, (1997)
23. V. M. Strutinsky. ”Shells” in deformed nuclei. *Nuclear Physics A*, **122**(1), 1–33, December 1968
24. P. Möller, J. R. Nix, W. D. Myers and W. J. Świątecki (1995). "Nuclear Ground-State Masses and Deformations." Atomic Data and Nuclear Data Tables **59**(2): 185-381.
25. Z. Patyk, A. Sobiczewski, P. Armbruster, K.-H. Schmidt, Shell effects in the properties of the heaviest nuclei. *Nuclear Phys. A* **491,** 267, 1989.
26. R. Smolanczuk, Phys. Rev. C 56, 812 (1997)
27. Y. Oganessian. Heaviest nuclei from ^{48}Ca-induced reactions. Journal of Physics G. Nuclear and Particle Physics, 34(4), R165–R242, 2007.
28. W. D. Myers and W. J. Swiatecki. Nuclear properties according to the Thomas-Fermi model. *Nuclear Physics A*, **601**,141–167, February 1996

29. A. Sobiczewski, Structure of Heaviest Nuclei, *Acta Physica Polonica B*, **29**, 2191, September 1998
30. S. Cwiok, J. Dobaczewski, P. H. Heenen, P. Magierski, and W. Nazarewicz. Shell Structure of the Superheavy Elements. *Nucl. Phys., A,***611**,211–246, 1996
31. Z. Patyk, J. Skalski, A. Sobiczewski, and S. Cwiok. Potential energy and spontaneous-fission half-lives for heavy and superheavy nuclei. *Nuclear Phys. A*, **502**,591–600, October 1989.
32. Z. Patyk and A. Sobiczewski. Ground-state properties of the heaviest nuclei analyzed in a multidimensional deformation space. *Nuclear Physics A*, **533**,132–152, October 1991.
33. M. Bender, P.-H. Heenen, and P.-G. Reinhard. Self-consistent mean-field models for nuclear structure. *Rev. Mod. Phys*., **75**,121–180, 2003
34. P. Armbruster, Ann. Rev. Nucl. Sci. **50**, 411 (2000)
35. R. Smolanczuk, A. Sobiczewski, in: Yu.Ts. Oganessian, W. von Oertzen, R. Kalpakchieva (Eds.), Proc. XV Nucl. Phys. Conf.: Low Energy Nuclear Dynamics, St. Petersburg, Russia, 1995, World Scientific, Singapore, 1995, p. 313
36. U. Mosel, W. Greiner, On the Stability of Superheavy Nuclei against Fission *Z. Phys*., **222**, 261, 1969
37. A. Sobiczewski, *Acta Physica Polonica B 29* (1987)
38. R. Smolanczuk and A. Sobiczewski. Low energy nuclear dynamics. In Yu. Oganessian, R. Kalpakchieva, and W. von Oertzen, editors, Proceedings of XV Nuclear Physics Divisional Conference "Low Energy Nuclear Dynamics", Singapore, 1995. St. Petersburg, Russia, World Scientific. p. 313
39. Y. A. Lazarev et al., Discovery of enhanced nuclear stability near the deformed shells N=162 and Z=108. *Physical Review Letters,* **73**, 624–627, August 1994
40. B. Kadkhodayan et al., On-line gaschromatographic studies of chlorides of rutherfordium and homologs Zr and Hf. *Radiochimica Acta*, **72**, 169, 1996
41. A. Ghiorso, M. Nurmia, K. Eskola, and P. Eskola. 261Rf; new isotope of element 104. *Physics Letters B*, **32**, 95–98, June 1970
42. M. R. Lane, K. E. Gregorich, D. M. Lee, M. F. Mohar, M. Hsu, C. D. Kacher, B. Kadkhodayan, M. P. Neu, N. J. Stoyer, E. R. Sylwester, J. C. Yang, and D. C. Hoffman. Spontaneous fission properties of $^{262}_{104}$Rf. *Physical Review C* **53**, 2893–2899, June 1996
43. S. Hofmann et al., New results on elements 111 and 112. *European Physical Journal A*, **14**, 147–157, 2002
44. K. Morita, K. Morimoto, D. Kaji, T. Akiyama, S. Goto, H. Haba, E. Ideguchi, H. Koura, H. Kudo, T. Ohnishi, A. Ozawa, T. Suda, K. Sueki, H. Xu, T. Yamaguchi, A. Yoneda, A. Yoshida, and Y.-L. Zhao. Experiments on synthesis of isotope ^{277}112 by ^{208}Pb + ^{70}Zn reaction. RIKEN Accel. Prog. Rep., 38:69, 2005.
45. A. Türler, R. Dressler, B. Eichler, H. W. Gäggeler, D. T. Jost, M. Schädel, W. Brüchle, K. E. Gregorich, N. Trautmann, and S. Taut. Decay properties of ^{265}Sg (Z=106) and ^{266}Sg (Z=106). *Phys. Rev. C*, **57**, 1648–1655, April 1998.
46. C. E. Düllmann, W. Brüchle, R. Dressler, K. Eberhardt, B. Eichler, R. Eichler, H. W. Gäggeler, T. N. Ginter, F. Glaus, K. E. Gregorich, D. C. Hoffman, E. Jäger, D. T. Jost, U. W. Kirbach, D. M. Lee, H. Nitsche, J. B. Patin, V. Pershina, D. Piguet, Z. Qin, M. Schädel, B. Schausten, E. Schimpf, H.-J. Schött, S. Soverna, R. Sudowe, P. Thörle, S. N. Timokhin, N. Trautmann, A.

Türler, A. Vahle, G. Wirth, A. B. Yakushev, P. M. Zielinski. Chemical investigation of hassium (element 108). *Nature*, **418,** 859 (2002)
47. J. Dvorak et al., Phys. Rev. Lett. 97, 242501 (2006)
48. J. Dvorak et al., Phys. Rev. Lett. 100, 132503 (2008)
49. R. Graeger, submitted to *Phys. Rev. C*
50. A. Yakushev, Habilitation thesis (2009)
51. I. Muntian, S. Hofmann, Z. Patyk, and A. Sobiczewski. Properties of Heaviest Nuclei. *Acta Physica Polonica B*, **34**, 2073, April 2003.
52. A. Sobiczewski. private communication.
53. R. B. Firestone and V. S. Shirley. Table of Isotopes, 2 Volume Set. Table of Isotopes, 2 Volume Set, by Richard B. Firestone, Virginia S. Shirley (Editor), pp. 3168. ISBN 0-471-33056-6. Wiley-VCH , December 1998.
54. S. Hofmann, F. P. Heßberger, D. Ackermann, S. Antalic, P. Cagarda, S. Cwiok, B. Kindler, J. Kojouharova, B. Lommel, R. Mann, G. Münzenberg, A. G. Popeko, S. Saro, H. J. Schött, and A. V. Yeremin. The new isotope ^{270}110 and its decay products ^{266}Hs and ^{262}Sg. *European Physical Journal A*, **10**, 5–10, 2001.
55. F.P. Hessberger, S. Hofmann, V. Ninov, P. Armbruster, H. Folger, G. Münzenberg, H.J. Sch¨ott, A.G. Popeko, A.V. Yeremin, A.N. Andreyev, and S. Saro. Spontaneous fission and alpha-decay properties of neutron deficient isotopes $^{257-253}$104 and ^{258}106. *Zeitschrift fuer Physik A Hadrons and Nuclei,* **359**(4), **415**, 12 (1997)
56. Oganessian, to be published
57. C. E. Düllmann and A. Türler, Phys. Rev. C 77, 064320 (2008)
58. Yu. Ts. Oganessian et al., Phys. Rev. Lett. 104, 142502 (2010)
59. R. Eichler et al., *Nature*, **447**(7140), 72–75, May 2007
60. S. Hofmann et al., *Eur. Phys. J. A* 32 3, 251, 2007
61. Glendenning, N. K. (2004). Direct Nuclear Reactions. River Edge, NJ, World Scientific Publishing Co.
62. V. I. Zagrebaev, M. G. Itkis and Y. T. Oganessian (2003). "Fusion Fission Dynamics and Perspectives of Future Experiments." Physics of Atomic Nuclei **66**(6): 1033
63. M. G. Itkis, Y. T. Oganessian, and V. I. Zagrebaev. Fission barriers of superheavy nuclei. Phys. Rev. C, 65(4): 044602, March 2002
64. M. Itkis et al., Fusion-fission of superheavy nuclei. Journal of Nuclear and Radiochemical Sciences, 3(1):5761, 2002
65. M. Schädel., The chemistry of the Superheavy Elements. Kluwer Academic Publishers Dordrecht/Boston/London, 2003
66. Keller O.L. *et al.*, J. Phys. Chem. 74, (1970) 1127
67. W. Loveland et al., "Search for the production of element 112 in the ^{48}Ca+^{238}U reaction." Physical Review C 66(4): 044617(2002)
68. K. E. Gregorich et al.,. "Cross-section limits for the 208 Pb(86Kr, n)293118 reaction." The European Physical Journal A - Hadrons and Nuclei 18(4): 633-638 (2003)
69. K. E. Gregorich et al.. "Attempt to confirm superheavy element production in the Ca-48+U-238 reaction." Physical Review C 72(1): 014605 (2005)
70. K. E. Gregorichet al., "New isotope 264Sg and decay properties of $^{262-264}$Sg." Physical Review C 74(4): 044611 (2006)
71. K. Morita, et al., Nucl. Instr. and Meth. in Phys. Res. B 70 (1992) 220-22

72. A. Semchenkov et al., Nucl. Instr. and Meth. in Phys. Res. B 266, 4153–4161 (2008)
73. S. Hofmann. On beyond uranium. Science Spectra, Taylor and Francis, London, 2002
74. C. B. Fulmer and B. L. Cohen. Equilibrium charges of fission fragments in gases. Phys. Rev., 109(1):94–99, January 1958
75. N. O. Lassen. Total charges of fission fragments in gaseous and solid media. Phys. Rev., 79(6):1016–1017, September 1950
76. N. Bohr. Velocity-Range Relation for Fission Fragments. Physical Review, 59:270–275, February 1941
77. A. Ghiorso et al., Nucl. Instr. and Meth. in Phys. Res. A 269 (1988) 192
78. K. E. Gregorich, et al. Attempt to confirm superheavy element production in the $^{48}Ca + ^{238}U$ reaction. Phys. Rev. C, 72:014605, (2005)
79. A. B. Wittkower and H. D. Betz. Equilibrium charge-state distributions of 2-15 MeV tantalum and uranium ions stripped in gases and solids. Physical Review A, 7:159–167, January 1973
80. A. Ghiorso, B. G. Harvey, G. R. Choppin, S. G. Thompson, and G. T. Seaborg. New element mendelevium, atomic number 101. Phys. Rev., 98(5):1518–1519, June 1955
81. M. Schädel. Chemistry of superheavy elements. Angewandte Chemie International Edition, 45(3):368–401, January 2006
82. Ch.E. Düllmann, Eur. Phys. J. D (2007) DOI: 10.1140/epjd/e2007-00033-9
83. Ch.E. Düllmann et al., Nucl. Instr. and Meth. in Phys. Res. A 551 (2005) 528-539
84. U. Kirbach et al., Nucl. Instr. and Meth. in Phys. Res. A 484 (2002) 587-594
85. A. Semchenkov. Modelling the differential pumping of the TASCA gas-vacuum system. GSI Scientific Report, 1:264, 2005
86. K. Brown, F. Rothacker, D. Carey, and C. Iselin. Transport: a computer program for designing charged particle beam transport systems. Technical Report 91 SLAC, 91:129, May 1977
87. U. Rohrer, "Computational programs for designing, investigating and commissioning charged particle beam lines". PSI Scientific and Technical Report 2000, VI (Large Research Facilities):24, 2001
88. A. Semchenkov, Envisaged TASCA configuration. GSI Scientific Report 2004, 1:332, 2005
89. K. E. Gregorich, Tasca Monte-Carlo simulation program and program for studying ion-optical parameters of dipole and quadrupole magnets from field maps. GSI Scientific Report 2006, 1:144, 2007
90. K. E. Gregorich, T. N. Ginter, W. Loveland, D. Peterson, J. B. Patin, C. M. Folden, D. C. Hoffman, D. M. Lee, H. Nitsche, J. P. Omtvedt, L. A. Omtvedt, L. Stavsetra, R. Sudowe, P. A. Wilk, P. M. Zielinski, and K. Aleklett. Crosssection limits for the $_{208}Pb(_{86}Kr,n)_{293}118$ reaction. European Physical Journal A Supplement, 18:633–638, (2003)
91. A. Semchenkov. private communication
92. A. Semchenkov. First TASCA commissioning experiments in the small image size mode. GSI Scientific Report, 1:145, 2006
93. C. Düllmann et al., TASCA as a preseparator: Recoil transfer chamber commissioning. GSI Scientific Report, 1:146, 2006
94. F.P. Heßberger et al., Nucl. Instr. Meth. in Phys. Res. B 204 597 (2003)
95. F.P.Heßberger et al., Eur. Phys. J. A 12 57 (2001)

96. Knoll, G. F. (2000). Radiation Detection and Measurement. New York, John Wiley & Sons.
97. J. L. Alberi and V. Radeka, Position Sensing by Charge Division, IEEE Trans. Nucl. Sci., NS-23, 251 (1976)
98. Š. Šaro et al., Nucl. Instr. and Meth. in Phys. Res. A 381 520-526, (1996)
99. A.V. Yeremin et al., Nucl. Instr. and Meth. A350 (1994) p. 608 -617
100. A.N. Andreyev et al., Nucl. Instr. and Meth. A 364 (1995) 342
101. M. Leino et al., Nucl. Instr. and Meth. B 99 (1995) 653
102. R.S. Simon et al., Z. Phys. A 325 (1986) 197
103. E.S. Paul et al., Phys. Rev. C 51 (1995) 78
104. I.H. Lazarus et al., IEEE Trans. Nucl. Sci. 48 (2001) 567
105. S.L. Thomas, T. Davinson, A.C. Shotter, Nucl. Instr. And Meth. A 288 (1990) 212
106. R.G. Allatt et al., Phys. Lett. B 437 (1998) 29
107. M. Schädel et al., GSI Sci. Rep. 2007, GSI Report 2008-1, 2008, p. 152
108. J. Khuyagbaatar, to be published
109. K.E. Gregorich *et al.*, GSI Sci. Rep. 2006, GSI Report 2007-1, 2007, p. 144
110. J. Even *et al.,* GSI Sci. Rep. 2008, GSI Report 2008-1, 2009, p. 143
111. L.-L. Andersson *et al.,* to be submitted in NIM
112. L. P. Somerville et al.,, Phys. Rev. C 31, 1801 (1985)
113. E. K. Hulet *et al.*, Phys. Rev. C **40**, 770 (1989)
114. J. M. Gates et al. Phys. Rev. C **77**, 034603 (2008)
115. B. Kadkhodayan *et al.*, Radiochim. Acta **72**, 169 (1996)
116. E. R. Sylwester *et al.*, Radiochim. Acta **88**, 837 (2000)
117. Y. Nagame Journal of Nuclear and Radiochemical Sciences, Vol. 6, No.2, pp. A21-A28, 2005
118. Yu. Ts. Oganessian *et al.*, Phys. Rev. C 64 (2001) 054606
119. M. Asai, Oral presentation at the 3rd International Conference on the Chemistry and Physics of the Transactinide Elements, TAN 07, September 23-28, 2007, Davos, Switzerland, (2007)
120. M. Asai, priv. comm
121. Y. A. Lazarev et al., Phys. Rev. C 62, 064307 (2000)
122. J. V. Kratz, A. Nähler, U. Rieth, A. Kronenberg, B. Kuczewski, E. Strub, W. Brüchle, M. Schädel, B. Schausten, A. Türler, H. W. Gäggeler, D. T. Jost, K. E. Gregorich, H. Nitsche, C. Laue, R. Sudowe, and P. A. Wilk. An EC-branch in the decay of 27-s ^{263}Db: Evidence for the isotope ^{263}Rf. *Radiochim. Acta*, **91**, 59–62, 2003.
123. M. Schädel, Eur. Phys. J. D 45, 67 (2007)
124. K. Eberhardt et al., Nucl. Instrum. Methods A 590, 134 (2008)
125. J. F. Ziegler, Nucl. Instrum. Methods B 219-220, 1027 (2004)
126. G. Audi, A. H. Wapstra, and C. Thibault, Nucl. Phys. A729, 337 (2003)
127. W. Reisdorf and M. Schädel. How well do we understand the synthesis of heavy elements by heavy-ion induced fusion? *Z. Phys. A*, **343**(1), 47, 03 1992.
128. Ch.E. Düllmann. Eur. Phys. J. D 45, 75–80 (2007)
129. K. Sümmerer, M. Brügger, W. Brüchle, H. Gäggeler, E. Jäger, M. Schädel, D. Schardt, E. Schimpf. ROMA - A Rotating Wheel Multidetector Apparatus used in Experiments with 254Es as a Target. GSI Annual Report 1983, 84-1, Darmstadt 246, 1984

130. K.-H. Schmidt, C.-C. Sahm, K. Pielenz, and H.-G. Clerc. Some remarks on the error analysis in the case of poor statistics. *Zeitschrift für Physik A* **316**(1), 19, 1984
131. Nuclear Data Sheets 99, 197 (2003)
132. Nuclear Data Sheets 84, 901 (1998)
133. K. E. Gregorich, priv. comm
134. H. G. Essel, J. Hoffmann, N. Kurz, R. S. Mayer, W. Ott, and D. Schall, The New Data Acquisition System at GSI, IEEE Trans. Nucl. Sci. NS-43, 132 (1996)
135. H. G. Essel and N. Kurz, The General Purpose Data Acquisition System MBS, IEEE Trans. Nucl. Sci. NS-47, 337 (2000)
136. J.Adamczewski, H.G.Essel, H.Göringer, M.Hemberger, N.Kurz, M.Richter, "Status of ROOT based analysis system Go4", GSI Annual Report 1999, 232 (2000)
137. J.Adamczewski et al., Go4 online monitoring, IEEE Trans. Nucl. Sci. Vol.51, No.3, 565 (2004)
138. H. J. Essel et al., GSI Sci. Rep. 2009
139. J. F. Ziegler, Nucl. Instrum. Methods B 219-220, 1027 (2004)
140. W. D. Myers and W. J. Świątecki, Nucl. Phys. A 601, 141 (1996)
141. F. P. Heßbergeret al., Eur. Phys. J. A 22, 417 (2004)
142. Yu. Ts. Oganessian et al., Phys. Rev. Lett. 83, 3154 (1999)
143. V. Ninov, P. Armbruster, F.P. Heßberger, S. Hofmann, G. Münzenberg, Y. Fujita, M. Leino and A. Lüttgen., Nucl. Instr. and Meth. in Phys. Res. A 357 (1995) 486
144. K. Subotic, et al., Nucl. Instr. and Meth. in Phys. Res. A 481 (2002) 71-80
145. K. Morita et al., J. Phys. Soc. Jap. 73 (2004) 2593-2596
146. K.E. Gregorich et al., submitted to Phys. Rev. Lett. (2007)
147. R.-D. Herzberg et al., Nature 442 (2006) 896-899
148. M. Leino, Nucl. Instr. and Meth. in Phys. Res. B 126 (1997) 320-328.
149. M. Schädel et al., GSI Sci. Rep. 2005, GSI Report 2006-1, 2006, p. 262, and http://www.gsi.de/TASCA
150. Ch.E. Düllmann et al., Nucl. Instr. and Meth. in Phys. Res. B 266 (2008) 4123M
151. Ch. E. Düllmann et al., Phys. Rev. Lett. in print (2010)

Appendix I

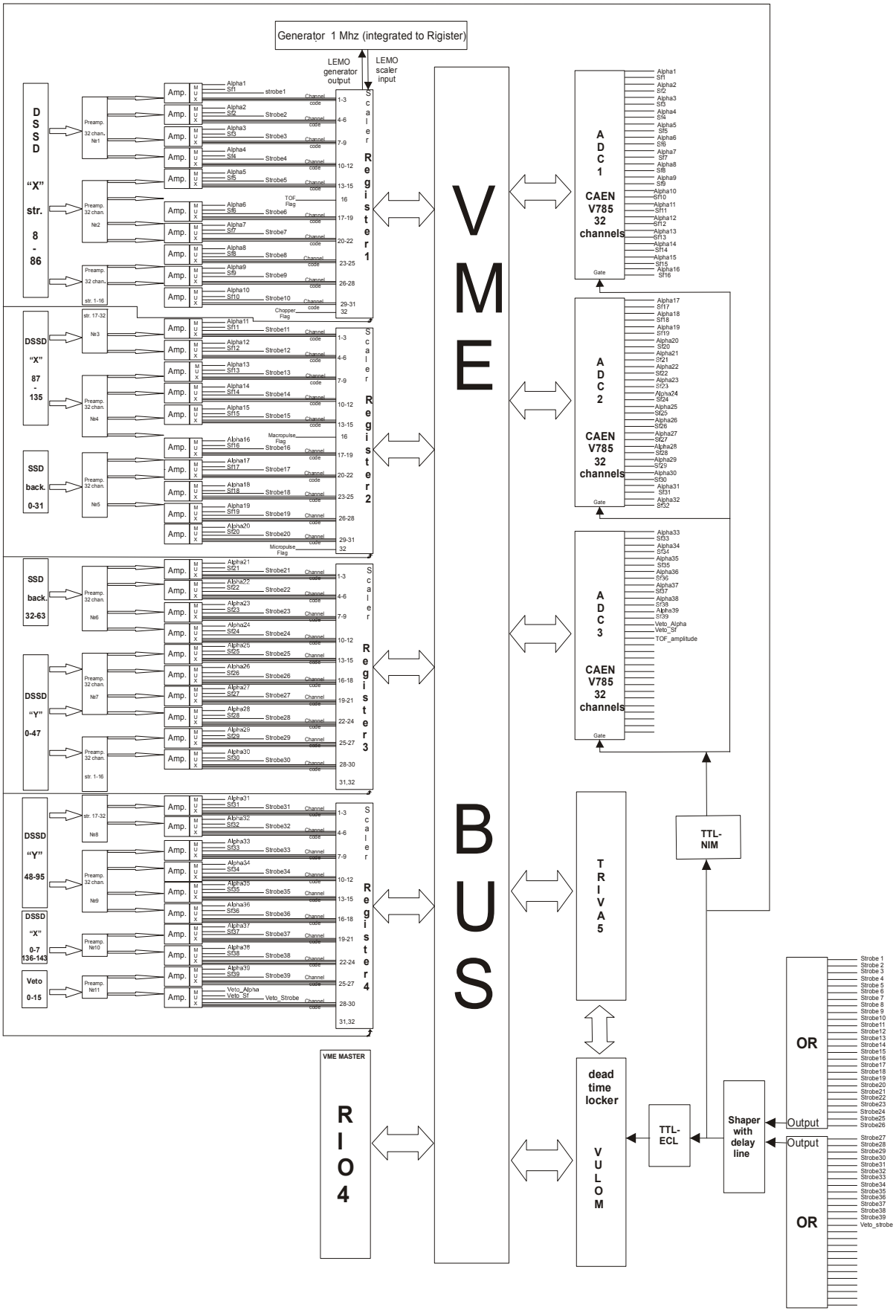
Generator 1 Mhz (integrated to Rigister)
LEMO generator output
LEMO scaler input
VME BUS
DSSD "X" str. 8 - 86
DSSD "X" 87 - 135
SSD back. 0-31
SSD back. 32-63
DSSD "Y" 0-47
DSSD "Y" 48-95
DSSD "X" 0-7 136-143
Veto 0-15
Scaler Register 1
Scaler Register 2
Scaler Register 3
Scaler Register 4
ADC 1 CAEN V785 32 channels
ADC 2 CAEN V785 32 channels
ADC 3 CAEN V785 32 channels
TRIVA 5
VME MASTER
RIO 4
dead time locker
VULOM
TTL-NIM
TTL-ECL
Shaper with delay line
OR
OR
Output
Output